5-2019

Development and Implementation of a Computational Surgical Planning Model for Pre-Operative Planning and Post-Operative Assessment and Analysis of Total Hip Arthroplasty

Manh Duc Ta
University of Tennessee, dta@vols.utk.edu

To the Graduate Council:

I am submitting herewith a dissertation written by Manh Duc Ta entitled "Development and Implementation of a Computational Surgical Planning Model for Pre-Operative Planning and Post-Operative Assessment and Analysis of Total Hip Arthroplasty." I have examined the final electronic copy of this dissertation for form and content and recommend that it be accepted in partial fulfillment of the requirements for the degree of Doctor of Philosophy, with a major in Biomedical Engineering.

Richard Komistek, Major Professor

We have read this dissertation and recommend its acceptance:

Mohamed Mahfouz, Jeffrey Reinbolt, Mingzhou Jin

Accepted for the Council:

Dixie L. Thompson

Vice Provost and Dean of the Graduate School

(Original signatures are on file with official student records.)

Development and Implementation of a Computational Surgical Planning Model for Pre-Operative Planning and Post-Operative Assessment and Analysis of Total Hip Arthroplasty

A Dissertation Presented for the
Doctor of Philosophy
Degree
The University of Tennessee, Knoxville

Manh Duc Ta

May 2019

DEDICATION

To my parents

To my wife, Duyen Lai

To my son, Steven Ta

ACKNOWLEDGEMENTS

First and foremost, I would like to thank Dr. Richard Komistek for his guidance, wisdom, and the source of knowledge throughout my time at the Center for Musculoskeletal Research (CMR). His constant support, guidance, and encouragement inspired me to become a better researcher, to always keep myself moving forward. I especially appreciate the opportunities he gave me to not only pursue the advanced education in orthopedics, but also helped me to see a clear vision of the connection between academia and the industry.

I would also like to thank Dr. Adrija Sharma for sharing with me incredible technical skills. Throughout the time working with him I have learned a lot. Now, I am confident to say to him that my coding skills are much better than they used to be.

Thank you, Dr. Mohamed Mahfouz, for sharing with me your extensive knowledge on 3D reconstruction using ultrasound technology, bone morphology, and constructive questions that really inspired me to seek better solutions.

Thank you, Dr. Jeffrey Reinbolt, for being the source of knowledge in OpenSim and teaching me to have a better understanding of human movement.

Thank you, Dr. Mingzhou Jin, for being a mentor and a friend, and for the invaluable insights and helpful feedbacks during the course of this dissertation.

I would also like thank Dr. John J. Callaghan MD for sharing with me incredible lessons on the selection of hip implant sizing from clinical perspectives. I would like to extend my gratitude to Mr. Randy Kilburn, CEO of JointVue, for sharing the valuable lessons on total hip arthroplasty from industrial and clinical visions.

I would also like to thank my colleagues at CMR and JointVue, including Dr. Michael LaCour, Dr. Ian Zeller, Dr. Trevor Grieco, Dr. Brad Meccia, Dr. Michael Johnson, Dr. Emam Fatah, and Mr. Mark Hawley, for your invaluable support during my time at CMR and JointVue. I would also like to thank to my current graduate colleagues at CMR, including Milad Khasian, Jarrod Nachtrab, Garett Dessinger, Seth Coomer, Lauren Smith, and undergraduate research assistants including Hunter Potter, Noah Dover, Jackson Lovelace, Ben Rouse, Leyton Adams, Daniel Nalepa, and Jan Bruckbauer for being supportive. I really appreciate your assistance during my time at CMR and enjoyed the time we ran projects together. I would also like especially thank Alex Defilippis, Chance Cuthbert, Jay Patel, and Seth Coomer, who helped me out to revise and give invaluable feedback for this dissertation. I would also like thank Rebecca Robertson, the person I really admire and my source of encouragement, for being very supportive not only to my research needs but also to my personal spirit.

I would also like to show my appreciation to the Ngo for the friendship, the source of encouragement, and being my second family.

Lastly, I would never have embarked on this journey without constant, emotional, beloved, and lifelong support of my family and my parents-in-law. Their belief in me has constantly motivated me to overcome many challenges to obtain this degree. Specially, from the bottom of my heart I would like to thank my wife for her unconditional love, sacrifices for the family, and for being my home. I would also thank my little son for coming at the right time and being the heart of our family.

ABSTRACT

Total hip arthroplasty (THA) is most often used to treat osteoarthritis of the hip joint. Due to lack of a better alternative, newer designs are evaluated experimentally using mechanical simulators and cadavers. These evaluation techniques, though necessary, are costly and time-consuming, limiting testing on a broader population. Due to the advancement in technology, the current focus has been to develop patient-specific solutions. The hip joint can be approximated as encompassing a bone socket geometry, and therefore the shapes of the implant are well constrained. The variability of performance after the surgery is mostly driven by surgical procedures. It is believed that placing the acetabular component within the "safe zone" will commonly lead to successful surgical outcomes [1]. Unfortunately, recent research has revealed problems with the safe zone concept, and there is a need for a better tool which can aid surgeons in planning for surgery.

With the advancement of computational power, more recent focus has been applied to the development of simulation tools that can predict implant performances. In this endeavor, a virtual hip simulator is being developed at the University of Tennessee Knoxville to provide designers and surgeons alike instant feedback about the performance of the hip implants. The mathematical framework behind this tool has been developed.

In this dissertation, the primary focus is to further expand the capabilities of the existing hip model and develop the front-end that can replicate a total hip arthroplasty surgery procedure pre-operatively, intra-operatively, and post-operatively. This new computer-assisted orthopaedic surgical tool will allow surgeons to simulate surgery, then

predict, compare, and optimize post-operative THA outcomes based on component placement, sizing choices, reaming and cutting locations, and surgical methods. This more advanced mathematical model can also reveal more information pre-operatively, allowing a surgeon to gain ample information before surgery, especially with difficult and revision cases. Moreover, this tool could also help during the implant development design process as designers can instantly simulate the performance of their new designs, under various surgical, simulated in vivo conditions.

TABLE OF CONTENTS

LIST OF TABLES

LIST OF FIGURES

CHAPTER 1: INTRODUCTION

The hip joint is a ball and socket synovial joint: the ball is the head of the femur, and the socket is the acetabulum of the pelvis. There is only one articulating surface between the femoral head and the acetabulum. The hip joint serves as the connection between the lower extremity and upper body, allowing relative motion between these two parts of the body. The hip joint allows for movement in three orthogonal axes and is driven by muscles across the joint. The movement in the coronal plane is referred to as the adduction/abduction of the hip. The movement in the sagittal plane is known as the flexion/extension of the hip. The movement in the transverse plane allows for the internal/external rotation of the hip.

The hip joint is strengthened by four capsular ligaments. The extracapsular ligaments consist of the pubofemoral, ischiofemoral, and iliofemoral ligaments. These capsular ligaments tighten and prevent an excessive range of motion of the hip joint to occur. The intracapsular ligament, sometimes referred as to the femoral head ligament, is attached to the acetabulum notch and a depression on the femoral head. This ligament is only stretched when resisting hip is dislocation, preventing further displacement.

Movements of the hip are driven by the activation of multiple muscles crossing the hip joint. Most muscles are responsible for more than one type of movement. Modern anatomists define 17 muscles crossing the hip joint. According to their functionalities and cause of movements, these muscles are divided into three groups: the flexion/extension group, the adduction/abduction group, and the internal/external group. For example, the muscles that cause the pelvis flexion/extension include the quadriceps muscle group, iliacus, the iliopsoas muscle group, and the gluteus maximus muscle group. Since the movements of the hip joint are so complicated, and there are many muscles that become activated at once, leading to the assumption of how muscles contribute to human body movements. The first assumption is that the muscles with larger physiological cross-sectional areas can generate larger forces. Similarly, the muscles with a longer moment arm are capable of generating larger torques.

Osteoarthritis is the most common chronic condition of the hip joint which causes the cartilage or cushion between joints to degenerate, essentially breaking down and leading to pain, stiffness, and swelling. According to Mayo Clinic, the Arthritis Foundation, and recent reports, there are more than 3 million people in the US who suffer from osteoarthritis each year [2-4]. In the past, people who suffered serious osteoarthritis were often forced to live with very limited motion in that joint for the rest of their lives. More recently, artificial joints that permit greater movement have been developed [5-7]. Ideally an artificial joint should move similarly to the normal healthy joint, while providing exceptional patient satisfaction and meeting all patient expectations. Therefore, it allows the patient to return to the quality of daily living she/he was used to prior to the diseased state.

Total hip arthroplasty (THA) (Figure 1-1b) is a surgical process that removes the damaged areas of the hip joint articulating surfaces and replaces them with artificial components that will allow for increased activity for the patient. According to a report in 2010 [8], the number of total hip arthroplasty cases in the United States was 2.5 million individuals. The age distribution is 45 and over. Specifically, the number of THA for younger age groups increased while it decreased for older age groups.

Regardless of a highly successful rate of total hip arthroplasty, there still exist many factors that contribute to the complications of THA. The complications are commonly due to osteoarthritis (Figure 1-1a), rheumatoid arthritis (inflammation of the synovial membrane), and osteonecrosis (injury to hip resulting in loss of blood supply to femoral head). Post-surgery complications are not as high as for other orthopedic surgeries, but there remain concerns. These complications include but are not limited to: infection around the surgery site, blood clots in the leg, unequal leg length, rough or grinding wear to the polymer lining of the cup, hip separation due to misalignment, and even full dislocation of the hip joint.

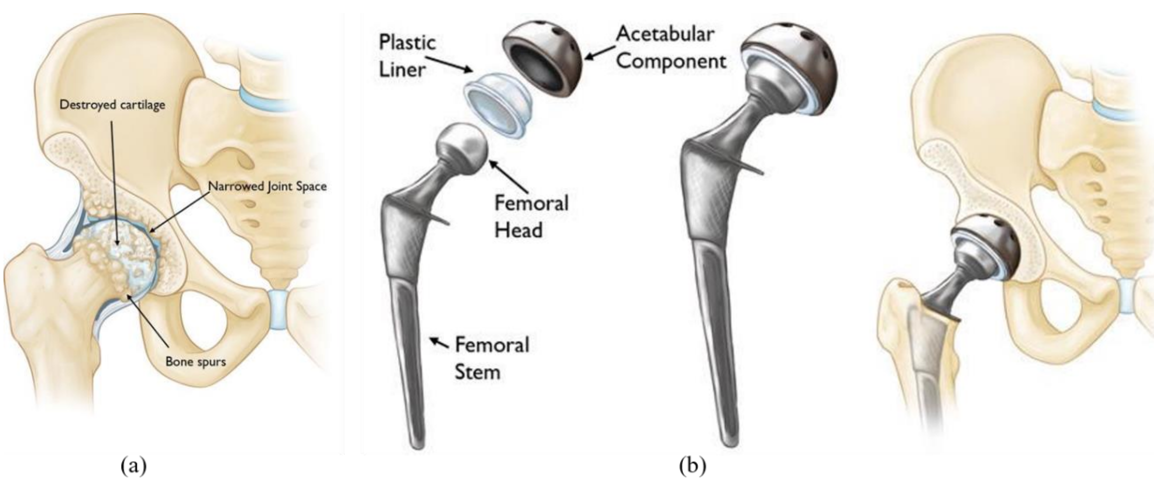

Figure 1-1: An osteoarthritic hip (a) and total hip arthroplasty (b). Image from (orthoinfo.aaos.org)

CHAPTER 2: LITERATURE REVIEW

Total hip arthroplasty has been an ideal solution for reducing pain and improving joint function in patients with hip arthritis. Long-term follow-up studies of THAs have shown a success rate exceeding 97.8% in five years and 95.8% in ten years [9, 10]. Perhaps, the most popular problems are in the form of hip dislocation or instability and wear of the contact surface between the acetabular cup and the femoral head [11-13]. Among these complications, cup positioning has been documented to be the leading cause of dislocation [13-15]. An ideal positioning of the cup in a THA can improve hip function and reduce impingement, wear, and dislocation. However, determining the optimal cup position is still a controversial problem. It is not a straightforward problem, as it involves several factors.

Wear of a material is a significant concern when two surfaces moving are in contact with each other. Fortunately, the advancement of material science has led to the development of high wear-resistant materials that are often utilized in contact-related research, especially in designing of artificial joints. In regard to contact pressures, stresses, and wear generated in the contact surfaces, a better understanding of in vivo loading at the hip joint is required.

It has been suggested that surgical planning or preoperative planning is the key to successful THA [16]. Effective preoperative planning allows the surgeon to understand the joint condition better before proceeding to the surgery. This step helps the surgeon to determine the impact of different interventions in order to restore the patient's natural anatomy [16]. For total hip arthroplasty, preoperative planning provides surgeons adequate information to appropriately choose implant component sizes, equalize the limbs, and reduce the duration of the operation [17]. Particularly, the goal of pre-operative planning is to find the optimal femoral stem fit, the level of femoral neck cut, the femoral component neck length, the femoral component offset, the size of the acetabular component, and the positions of the femoral component and acetabular cup [18].

Traditionally, conventional radiographs of the hip were used to assist surgeons during the preoperative planning process. Size and location of implants were measured by overlaying schematics of the implanted components onto the preoperative radiographs. Most of the currently available planning tools are in two-dimensions (2D), using X-ray images and 2D templates of the implants [19-21]. Determination of the ideal component size requires at least two radiographic views of the involved femur: one in the anterior-posterior (AP) and one in the lateral direction. When templating, the magnification of the femur and pelvis will vary according to the distance from the patient and the x-ray source to the film. Visible makers on X-ray images will be placed to identify the actual magnification of the radiograph [19, 22]. The surgeon will use this information in order to anticipate the component size accurately. Even though this approach has been used for quite some time now and has led to very good results, this manual process potentially carries multiple shortcomings.

The biggest issue is that the AP X-ray image is the fact that it is 2D in nature while the measurement's objective is to obtain three-dimensional (3D) parameters [19, 20, 23]. For example, measurement of the femoral neck shaft angle from the AP X-ray images has been documented to be different from its measurement in 3D [24, 25]. Mahfouz et al. has shown that the mean difference between 2D and 3D approaches for measuring the femoral neck shaft angle is about 12 degrees in females and 13 degrees in males [24, 25]. Another example is that the fit and fill of the femoral component in the proximal femoral canal is vastly different in 2D when compared with 3D. As shown in Figure 2-1 the femoral stem fits the canal well in the frontal view, similar to what is seen in an AP x-ray of the hip, but badly in the sagittal and axial views.

Recently, 3D planning tools have been introduced to assist the surgeon in the pre-operative planning process. These software packages often integrate the built-in CT scans of the patient and the 3D CAD models of the implants [15, 26-28]. The software package allows the surgeon to place the implant components into the proper position of the 3D space of the CT data. The surgeon can manually adjust the size of the component between those available, while controlling the level of fit and fill achieved, using a contact map analysis generated by the program [27].

For example, Brainlab Inc has developed a surgical planning program that assists the surgeon, allowing for the determination of the best fitting hip implant [29]. This program takes the silhouettes of 3D CAD models of the hip implants and overlays them onto the AP X-ray image if the hip. This approach is superior to the traditional approach as the silhouettes of 3D CAD models can be rotated and translated to fit the X-ray image. In addition, the acetabular cup's version and inclination can be achieved from this program. However, using an X-ray image to determine the best fitting implants still lacks accuracy due to the nature of the X-ray image itself. On the other hand, other commercial surgical planning programs use CT scans, and segmented femoral and pelvis bone models

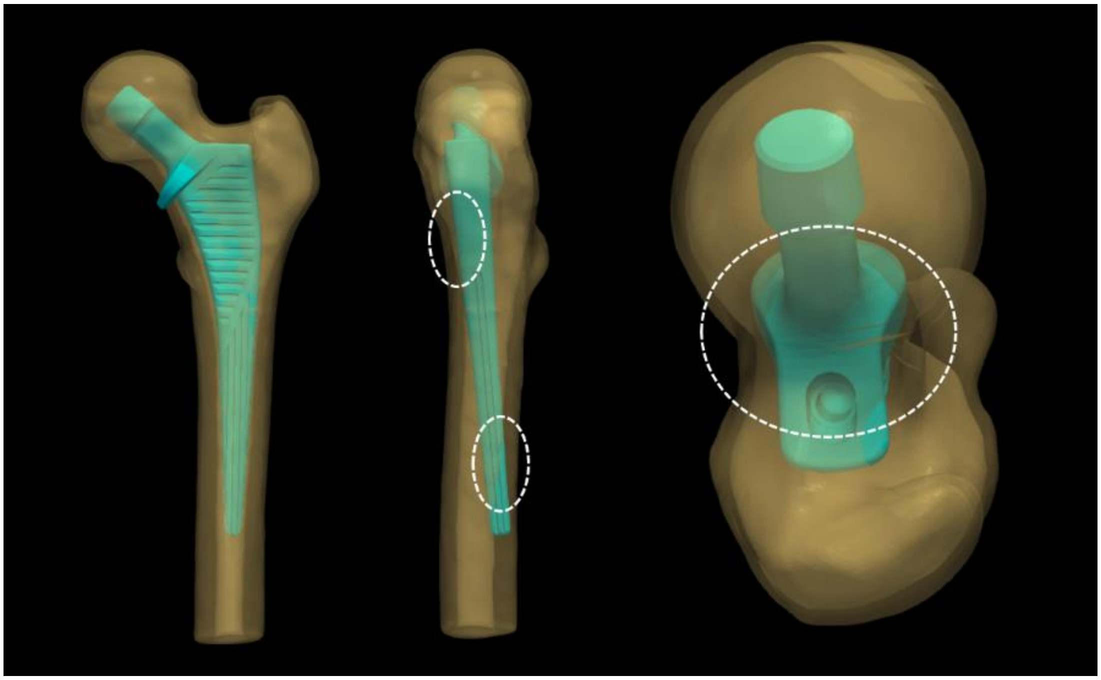

Figure 2-1: The femoral stem fits the canal well in the frontal view (left image), but fits badly in the sagittal (middle image) and axial (right image) view.

from CT scans to estimate the size of implants [26, 28, 30]. This approach is fully conducted in 3D and provides sufficient accuracy to determine the size of the hip implants by templating and trying different sizes one by one. However, these software packages are completely manual and therefore lack efficiency.

Measurement of the proximal femoral morphology plays a crucial role in the estimation of the size of existing hip arthroplasty implants and the design of new implants. However, it has not been prioritized during the surgical planning process as most of the surgical planning techniques rely on a templating procedure. Traditionally, the morphology of the proximal femur was measured based on radiographs in the frontal and sagittal views [31, 32]. The parameters of interest that are often measured are shown in Figure 2-2.

The canal flare index (CFI), defined as the ratio of the intracortical width of the femur at a point 20 mm proximal to the lesser trochanter to that at the medullary isthmus, was calculated [31]. Based on the calculated CIF, the femoral shapes are then classified into three groups, providing a basis for the design and selection of femoral implants.

CT scans have been utilized to measure the morphology of the proximal femur for more than two decades [32-36]. It has been concluded that using CT scans provide a precise technique in experimental conditions. It is superior to the traditional technique of using radiographic images in several ways. One advantage is the ability to evaluate specific angles of the 3D configuration that cannot be done by a manual or 3D based radiographic measurement. Another advantage is that the axis of any portion, such as the femoral neck axis or the femoral shaft axis, can be set up from within the structure; this cannot be

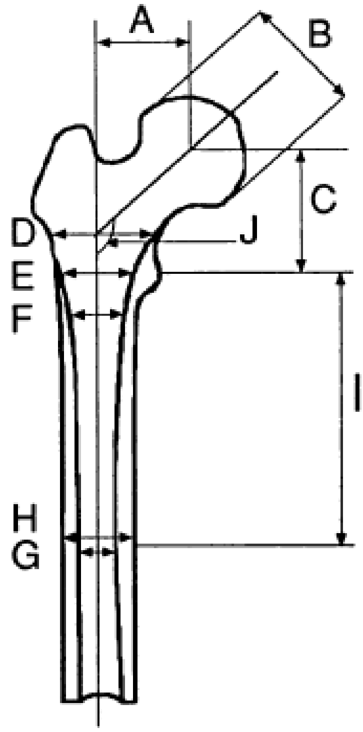

Figure 2-2: The parameters of interest in the measurement of the proximal femur: the femoral offset (A), femoral head diameter (B), femoral head position (C), Canal width at 20 mm above the lesser trochanter (D), canal width at the level of the lesser trochanter (E), canal width at 20 mm below the lesser trochanter (F), endosteal width at the isthmus (G), periosteal width at the isthmus (H), isthmus position (I), and femoral neck shaft angle (J). Image from [32].

performed by any other method [37]. However, most of them have relied on a manual process that is inefficient and potentially subject to human error.

Qualitatively, the CFI provides the surgeons with meaningful information to approximate the femoral stem size and determine whether he or she needs a smaller or larger size for their patient. The CFI does not provide the surgeon with a specific size that will fit their patient, due to a lack of the corresponding information of the femoral stems. Therefore, there is a need for research to investigate which information of the femoral stem is corresponding to the measured morphology of the proximal femur.

Anatomical landmarks have been used as reference points for measurement of the proximal femoral morphology [25, 33, 36, 38]. Obtaining accurate anatomical landmarks is needed to have a better morphologic measurement but challenging due to the variation of bony geometries. If a manual approach is used, surgeons or engineers have to get CT or MRI scans and pick landmarks based on the 3D representation of the scanned data. This manual process can be done with a limited number of subjects, but is time-consuming, labor expensive, and inefficient when there are a large number of subjects. It is also challenging due to population variations and deformity of the bone model resulting from arthritis or movement disorder. Therefore, extensive research exists on how to automatically obtain anatomical landmarks on a new bone model given a set of known landmarks on a known bone model.

Anatomical landmarking can be achieved using either a statistical shape model or template matching [39-43]. Statistical modeling approaches require a large number of training data in order to capture population variation [24, 39, 40]. These techniques, though powerful, robust, and able to capture geometric differences due to population variation, are labor expensive and require a large training dataset that is not always available.

Prediction of anatomical landmarks through the template matching techniques has also been extensively investigated. Rigid and non-rigid registrations are the most often used techniques in order to predict landmarks on a new bone model [44-49]. Given a known template bone model and a new bone model, non-rigid algorithms, like statistical shape modeling techniques, deform the template bone model to best match the new bone model [49, 50]. The anatomical landmarks are then predicted in the new bone model through a non-rigid transformation. These non-rigid algorithms differ from the statistical shape modeling techniques in a way, such that, the non-rigid algorithms do not require a large number of training datasets. Instead, these techniques are based on the minimization or maximization of an objective function or cost function. As is the nature of non-rigid algorithms, these techniques can be trapped in the local maxima if the template and new bone models have noise or outliners.

On the other hand, rigid registration techniques map the anatomical landmarks from the template to the new bone models though a rigid transformation. These techniques are able to maintain the relative positions of the landmarks due to the nature of rigid transformation [48, 51]. However, they fail to address the geometric differences due to population variation. Therefore, a combination of rigid and non-rigid registration techniques is a needed for research, in order to obtain accurate anatomical landmarks and improve the landmark prediction process.

Prediction of anatomical landmarks, though well investigated, has not been prioritized in computational biomechanics or mathematical modeling. In the mathematical modeling techniques, there are a large number of anatomical landmarks that need to be defined. These landmarks can be muscle and ligament attachment and insertion sites, bone references, or even user-defined points. For a single subject simulation, the user can define all of these landmarks manually. However, if multiple subjects are needed to simulate, prediction of anatomical landmarks would be a powerful tool that helps the user save time and work efficiently.

Regardless of the effort to improve THA performance, it is extremely important to evaluate how the THA functions after the surgery. THA assessment has been done using mechanical simulators, cadaveric rig, telemetry, and long-term follow up using fluoroscopy [6, 52-59]. These methods produce a direct and accurate measurement of motion and interaction forces and moments across at the joint. These methods, however, are either time-consuming, expensive or lack the physiological representation of the human hip joint under in vivo conditions. Mathematical modeling is a promisingly, alternative theoretical technique that relies on mathematical predictions to quantify new artificial joints [60-65]. The development of mathematical modeling can lead to tremendous important advantages.

As a theoretical approach, the most important benefit of mathematical modeling is to allow thousands of computer-aided experiments to explore how new THA designs perform. THA implants need to be examined carefully before implanting into the human body. A mathematical model aims to create a computer-based visualization in which the

THA implants mimic the actual human joints during any activity [5]. However, this is a very difficult task since the human joints involve a complex musculoskeletal system composed of a huge number of tendons, ligaments, soft tissue, and muscles [66]. For example, the hip joint consists of more than 17 muscles [61, 63, 67]. With the aid of computers, the human hip joint has been successfully modeled by utilizing either optimization techniques or reduction methods. The optimization principle allows for the solving of a complicated system, which retains most of the joint components [63, 65, 68-70], while reduction methods remove unnecessary muscles from the simulation and group the remaining muscles together. With the assumption that the force of the grouped muscles characterizes the best fit estimation of the force acting within each particular muscle, researchers can customize input values to investigate how new implants perform in a computer-aided environment [5, 60, 61, 71-73].

Reduction-based mathematical modeling has been successfully developed in order to simulate and predict interaction forces as well as motions not only of the human knee but also of the hip [5, 60, 72]. Recently, a fully forward solution model of the hip has been developed at the Center for Musculoskeletal Research, the University of Tennessee [61]. This model has successfully predicted hip separation, edge loading, impingement of total hip arthroplasty. The model also has the capabilities to compare various implant designs and surgical conditions. This model has played a foundational role in this dissertation.

CHAPTER 3: RESEARCH AIMS

Total hip arthroplasty is most often used to treat osteoarthritis of the hip joint. Due to lack of a better alternative, newer designs are evaluated experimentally using mechanical simulators and cadavers. These evaluation techniques, though necessary, are costly and time-consuming, limiting testing on a broader population. Due to the advancement in technology, the current focus has been to develop patient-specific solutions. The hip joint can be approximated as encompassing a bone socket geometry, and therefore the shapes of the implant are well constrained. The variability of performance after the surgery is mostly driven by surgical procedures. It is believed that placing the acetabular component within the "safe zone" will commonly lead to successful surgical outcomes [1]. Unfortunately, recent research has revealed problems with the safe zone concept, and there is a need for a better tool which can aid surgeons in planning for surgery.

With the advancement of computational power, more recent focus has been applied to the development of simulation tools that can predict implant performances. In this endeavor, a virtual hip simulator is being developed at the University of Tennessee Knoxville to provide designers and surgeons alike instant feedback about the performance of the hip implants. The mathematical framework behind this tool has been developed.

In this dissertation, the primary focus is to further expand the capabilities of the existing hip model and develop the front-end that can replicate a total hip arthroplasty surgery procedure pre-operatively, intra-operatively, and post-operatively. This new computer-assisted orthopaedic surgical tool will allow surgeons to simulate surgery, then predict, compare, and optimize post-operative THA outcomes based on component placement, sizing choices, reaming and cutting locations, and surgical methods. This more advanced mathematical model can also reveal more information pre-operatively, allowing a surgeon to gain ample information before surgery, especially with difficult and revision cases. Moreover, this tool could also help during the implant development design process as designers can instantly simulate the performance of their new designs, under various surgical, simulated in vivo conditions.

CHAPTER 4: MATERIALS AND METHODS

4.1 ANATOMICAL LANDMARKING

4.1.1 Algorithm Framework

The algorithm framework for the anatomical landmarking module is represented in Figure 4-1. This algorithm aims to predict anatomical landmarks on a new bone model with respect to a template bone model having known, identifiable landmarks. Initially, the 3D meshes for a template bone and the new bone of question are imported into the program. Landmarks on the template bone are also loaded with the import data. Then, the template and new bones are located at arbitrary positions within the global coordinate system. If they are determined to be placed at different positions with significant differences in orientation, the user will need to re-align the bone to ensure that they are close enough for the process to commence.

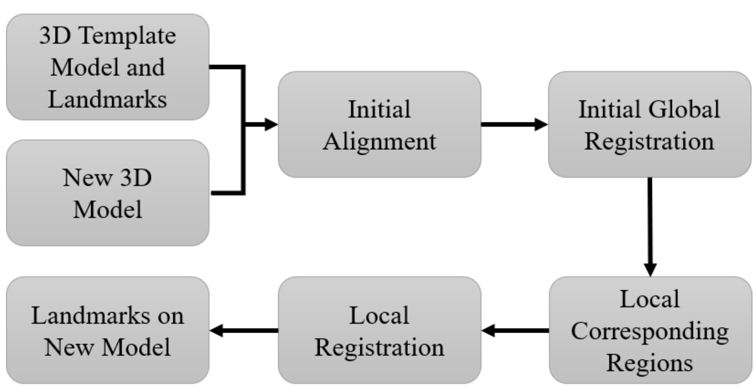

Figure 4-1: Anatomical landmark algorithm framework.

After initially aligning the bones, the new bone model appears closer to the template bone model. The template bone model is then registered to the new model using Iterative Closest Point (ICP) with scaling [74], a variant of the ICP algorithm [51], to find the initial region of correspondences. For each anatomical landmark on the template, initial corresponding landmarks on the new bone model are defined as being its closest point. For some applications, the initial landmarks on the new bone model are good enough and can be used for further analysis. However, in biomechanical applications, landmarks on the new model need to be precise as surgeons and engineers will use those landmarks for surgical planning, implant size identification, and possibly for robot-assisted surgery (RAS). To refine landmarks on the new bone model, the next step is to determine local corresponding regions between the template and new bone models. This task can be done by using the landmarks on the template and initial landmarks on the new bone model. For each landmark on the template and new bone models, a subsample surface of the mesh model is then obtained based on a distance measurement to the landmark. This empirical distance is consistently used in both the template and new bone models and for all landmarks. Local corresponding regions on the template and new bone models are then registered again using the ICP with scaling (ICPs) algorithm to refine the locations of landmarks on the new model.

4.1.2 Initial Alignment

If the two input models have a significant difference in orientation, they need to be pre-aligned by the user. In Figure 4-2 two input models are initially positioned in an opposite orientation and then reoriented into the required positions. There are several approaches that can be used for the initial alignment of the two bone models. The most popular approach is to identify three corresponding landmarks on the template and new bone model. This approach is primarily used in the clinical setting as surgeons prefer using definable landmarks. However, for general users or engineers, this approach may be challenging due to a lack of anatomical background understanding. In this section, a more efficient approach is introduced that can be used for both surgeons and engineers. This new approach utilizes Visualization Toolkit (VTK) [75], an open source software developed by Kitware for 3D computer graphics, modeling, image processing, and scientific visualization. The template and new model are loaded into VTK for visualization. The VTK software allows for handling and interacting with 3D bone models. Therefore, users can transform (rotate and translate) the new bone model using a computer mouse to realign the two bone models into proper position (Figure 4-3). This process is straight forward, takes less effort, and can be finished in a timely manner as users can visualize and align two bone models without extensive knowledge of human anatomy. As shown in Figure 4-3, the new bone model is covered by a bounding box that allows users to rotate and translate the bones. The bounding box will be rotated and translated along with the bone model as it moves. In some case, users can scale the model if necessary. However, in this application the shape of the new model bone should remain unscaled as landmarks from the template bone model will be mapped onto the new bone model. When two models are lined up as shown in Figure 4-4, the new model is saved in this orientation to be then used for the global registration process.

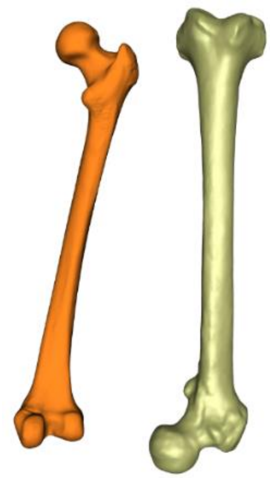

Figure 4-2: Misalignment of input models that needs to be pre-aligned.

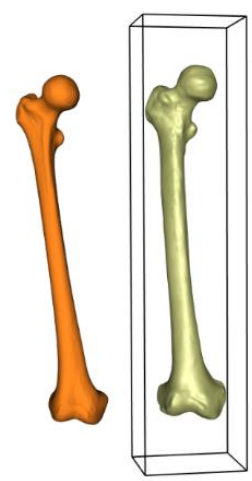

Figure 4-3: Interactive initial alignment of the template and new model.

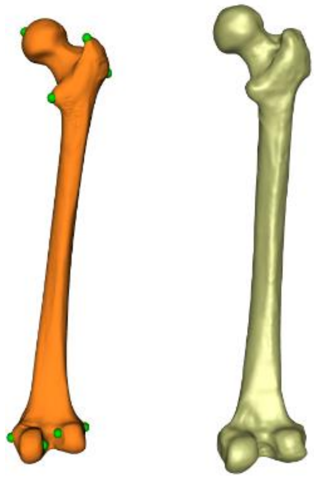

Figure 4-4: The new model is lined up with the template model. The template model is on the left. The new model is on the right.

4.1.3 Initial Global Registration

Since the template and new bone models are properly aligned, the process can continue towards initial global registration. The mesh models for the bones are input to an initial global registration sequence using the ICPs algorithm [74]. This step aims defines the initial alignment between the template and the new bone models and can be completed by translating, rotating, and scaling the template to best fit with the new model throughout the ICPs algorithm (Figure 4-5).

The ICP algorithm is the best known as a method to minimize the difference between two clouds of points. The algorithm is performed on two sets of points: (1) reference or target set, and (2) the source set. The target set is kept fixed, while the source set is transformed for the best target match. The algorithm iteratively revises the transformation (translation and rotation) to minimize a cost function or an error metric. The algorithm proposed in this dissertation [51] uses a mean square error as the cost function.

The ICP algorithm always converges to the nearest local minimum of a mean square error. Therefore, given a certain initial rotation and translation of the source, there always exists a combination of the rotation and translation so that the source best matches the target. For this reason, the initial registration step mentioned in the previous section is crucial to obtain the best alignment between the two models.

The ICP, with scaling, (ICPs) [74] enhances the ICP algorithm by using a scaling factor. As the ICP algorithm iteratively alters the rotation and translation, the ICPs algorithm adds a scaling factor to its iterations. Routinely, in biomechanical problems two bone models can have different shapes and sizes even when they represent the same part

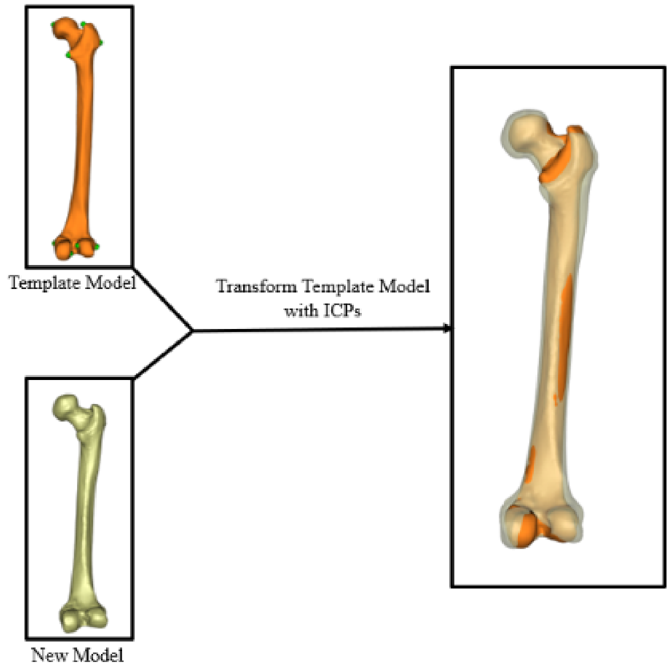

Figure 4-5: Initial global registration. The template model will be transformed (rotated, translated, and scaled) to line up with the new model using the ICPs algorithm.

of the human body. For instance, the femur of a male subject should be different in shape and size from the femur of a female subject even though they are both femurs. Apparently, they look similar in anatomy but different in geometry. The ICPs algorithm accounts for the sizing difference between the two models. In Figure 4-6 it can be seen a comparison of the scaled and non-scaled template model using ICPs and ICP algorithm, respectively.

Figure 4-7 and Figure 4-8 represent a comparison of the scaled and non-scaled model with the new model.

In this application, the objective is to map the landmarks from the template to the new bone model. For that reason, the template bone model with landmarks will play a role as the source bone model (the moving model) while the new bone model will be the target bone model (the fixed model) (Figure 4-5). Once the two bone models are aligned, the initial corresponding landmarks on the new bone model are determined as the closest points to the landmarks on the template bone model. The process can be seen in Figure 4-9, demonstrating the initial landmarks on the new bone model.

As can occur, the initial landmarks on the new bone can be far from the true landmarks so the initial global registration uses the entire bone model during the registration process. Initial global registration realigns two separate bones into the best position but ignores local regions alignment. As shown in Figure 4-10, initial lesser trochanter of the new bone (purple) is the closest point to the lesser trochanter on the template bone (green), but not the true lesser trochanter of the new bone. Similar to the greater trochanter (Figure 4-11), there still exists deviation to predict landmarks on the new bone after initial global registration.

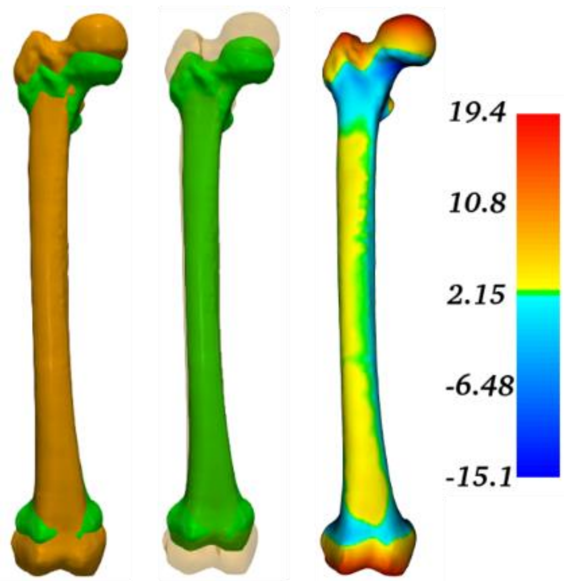

Figure 4-6: Comparison of the scaled and non-scaled template model using ICPs and ICPs algorithm, respectively. The orange model represents the scaled model using the ICPs algorithm while the green model is the non-scaled model using ICP.

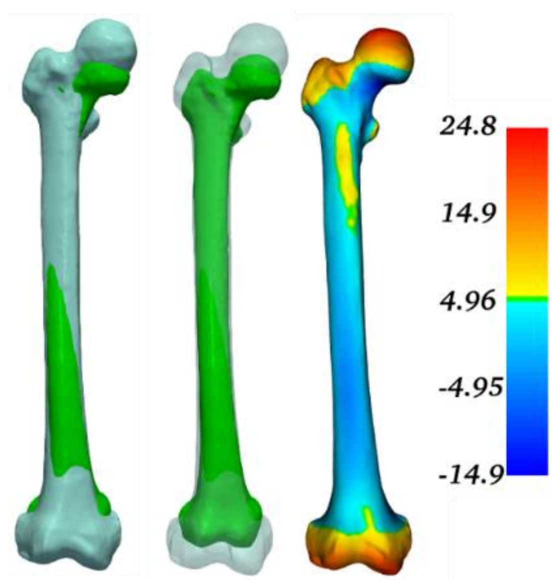

Figure 4-7: Comparison of the non-scaled model (green) using the ICP algorithm to the new model (cyan).

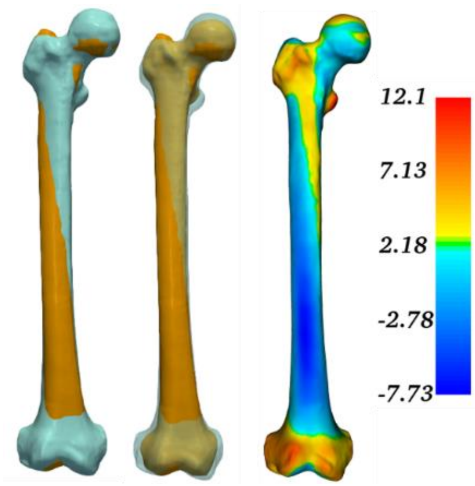

Figure 4-8: Comparison of the scaled model (orange) using the ICPs algorithm and the new model (cyan).

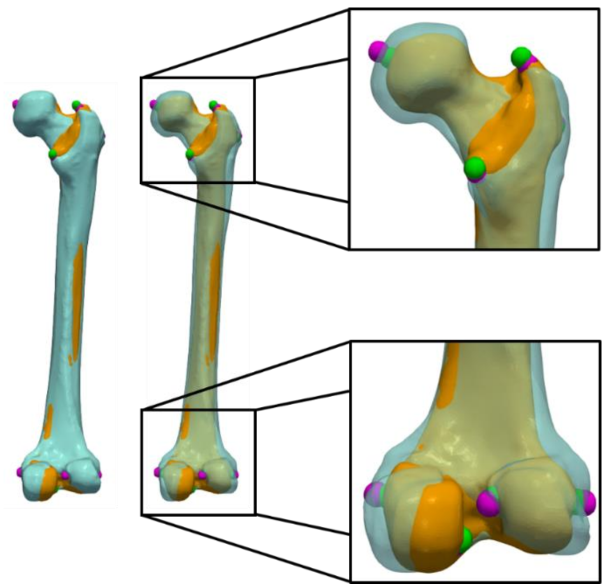

Figure 4-9: The initial landmarks on the new model (purple) are determined to be the closest points to the landmarks on the template (green). The template model is in orange while the new model is in cyan.

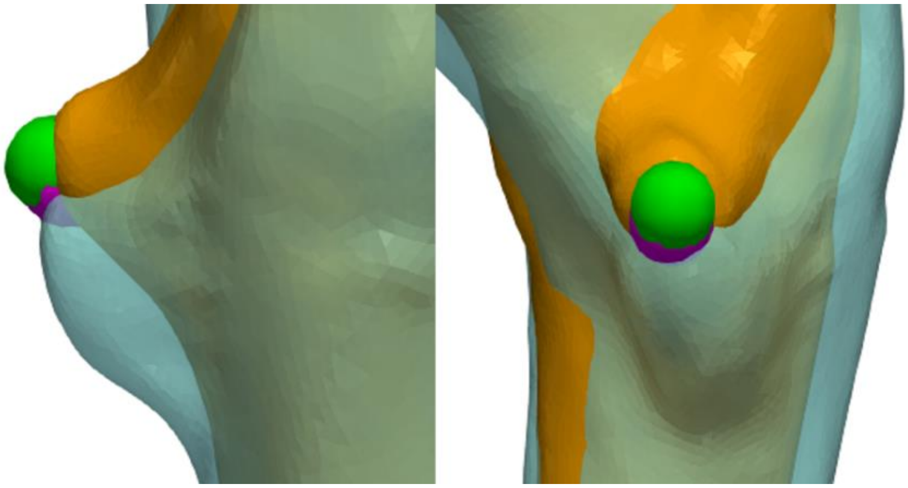

Figure 4-10: Initial lesser trochanter on the new bone after initial global registration. Landmark on the template model (orange) is in green. Landmark on the new bone (cyan) is in purple.

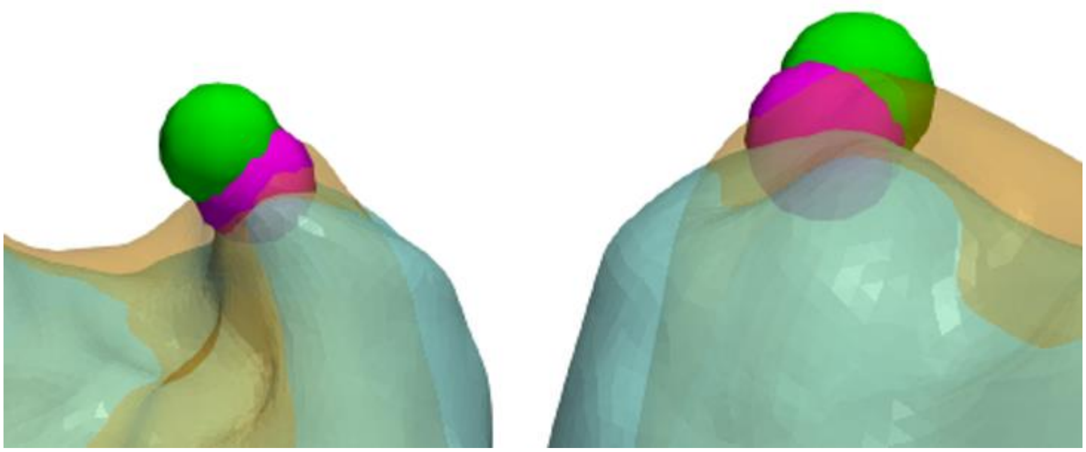

Figure 4-11: Initial greater trochanter on the new bone after initial global registration. Landmark on the template model (orange) is in green. Landmark on the new bone (cyan) is in purple.

4.1.4 Determination of Corresponding Regions

Initial global registration does not define an accurate prediction of landmarks on the new bone but does determine the correspondences between two bone models. For each matching-pair landmark on the template and new bone models, a local neighborhood of vertices on the template and new bone are identified as those vertices within a defined sphere having the center as the landmark location and radius being an empirical value. The radius of the sphere is kept consistent for all landmarks and set to 5 mm. This empirical radius should neither be significantly small nor significantly large. It can vary depending on which bone models are analyzed. Ideally, the empirical radius should be sufficient enough to capture a meaningful structure of the surrounding area. An example of a meaningful structure should consist of high curvatures and extreme points. In Figure 4-12, it can be seen that the local area of vertices is located around the initial landmark on the femoral head of the new bone. The local neighborhoods of vertices around the femoral head ligament landmark on the template model can be seen in Figure 4-13. As shown in Figure 4-14 and Figure 4-15 the corresponding local regions between the template and new model are defined around the femoral head ligament landmark, lesser trochanter, medial and lateral femoral epicondyle, respectively.

4.1.5 Local Registration

The local registration process is carried out between two local corresponding regions on the template and new model. This step enhances the accuracy of predicting landmarks on the new model. Initially, the global registration is conducted using the ICPs algorithm [74]. Figure 4-16 represents the framework of local registration.

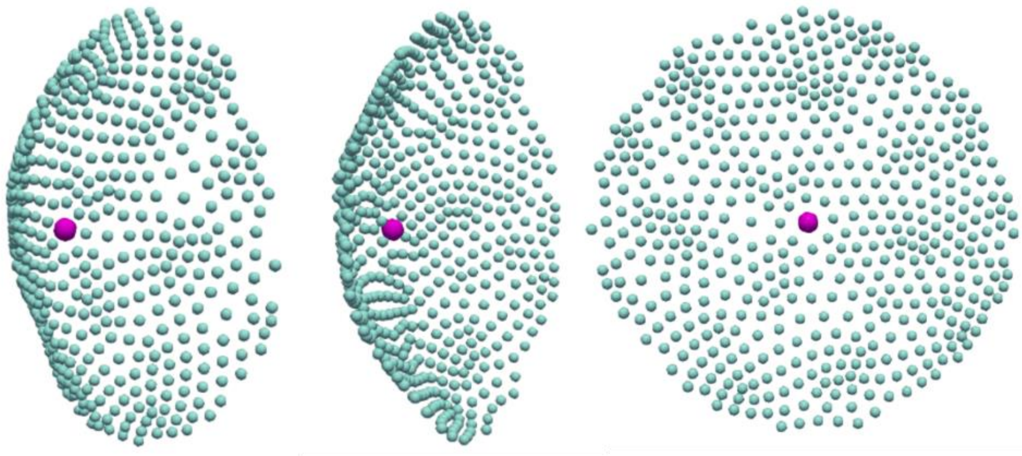

Figure 4-12: The local neighborhoods of vertices around the initial landmark on the femoral head of the new bone.

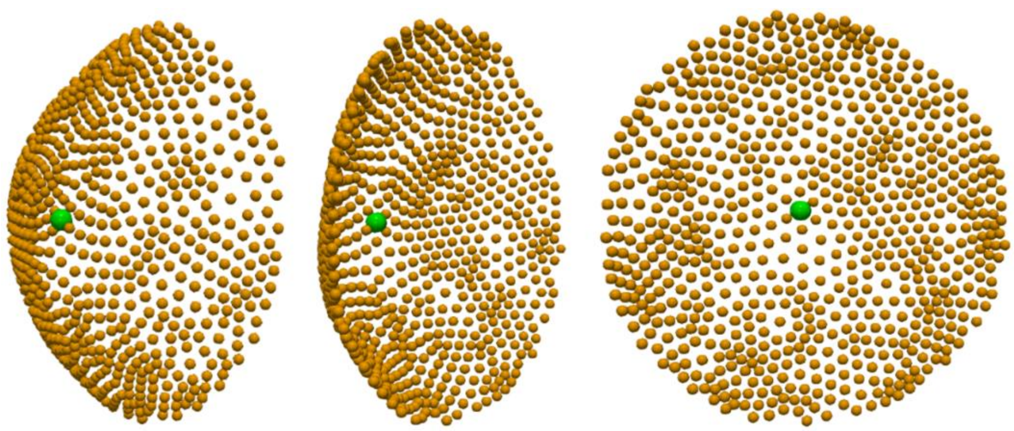

Figure 4-13: The local neighborhoods of vertices around the landmark on the femoral head of the template model.

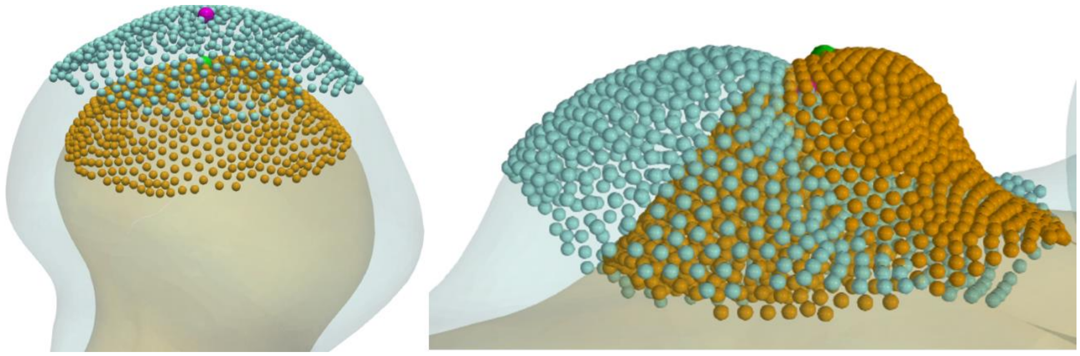

Figure 4-14: Local Corresponding regions of neighbors around the landmark on the femoral head (left) and lesser trochanter (right).

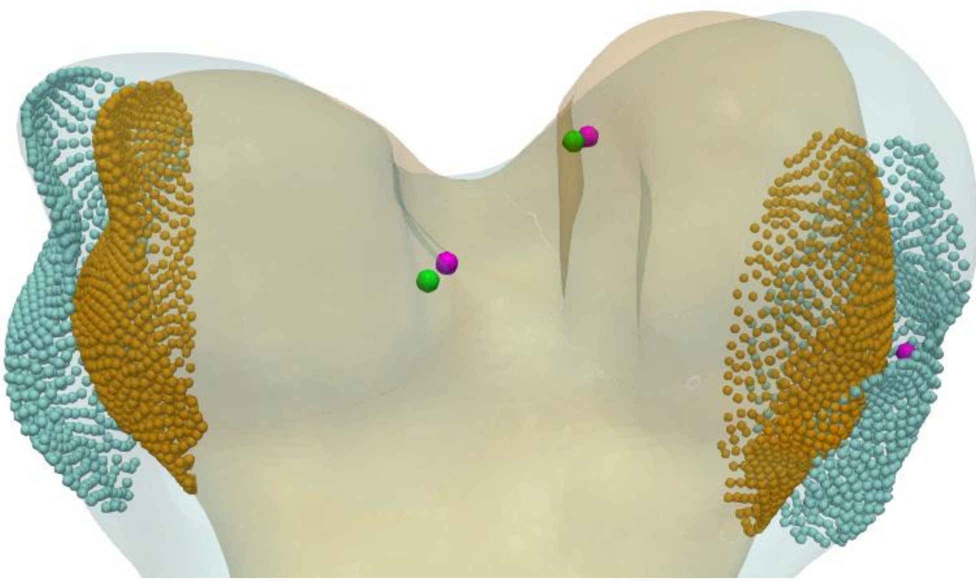

Figure 4-15: Local corresponding regions of neighbors of the medial and lateral femoral epicondyles.

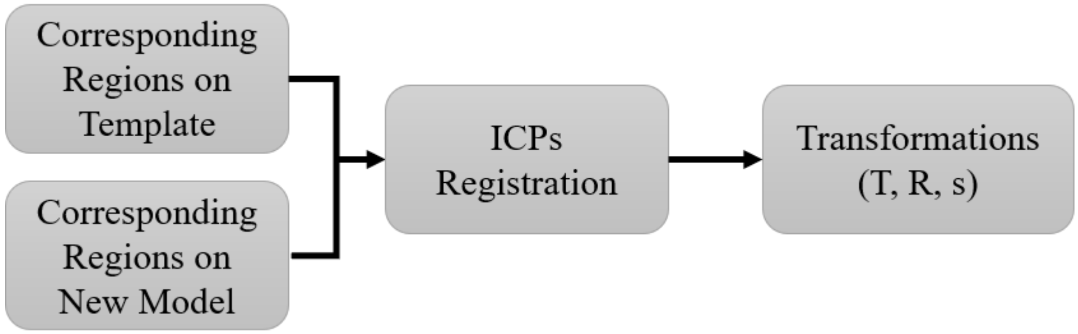

Figure 4-16: Local registration framework.

As each landmark has one local area of vertices, the number of corresponding regions is the same to the number of landmarks. The transformations that best match the corresponding regions on the template to those on the new model will be used to map the landmarks on the template bone to the new bone model. Figure 4-17 - Figure 4-22 define the corresponding regions on the template and new bone before and after local registration.

4.1.6 Mapping Landmarks to the New Bone Model

Once the local regions on the template bone model are registered to their corresponding regions on the new bone model, the transformations are used to transfer landmarks from the initial global registered-template to the local registered-regions of the template. Quite simply, each time the registration algorithm is performed, the landmarks on the template bone are transformed along with the registration to realign them closer to the true landmarks on the new bone model. The refined landmarks on the new bone model are determined to be the closest points to the last transformed landmarks of the template bone after the local registration. Figure 4-23 - Figure 4-28 show the process used to define the landmarks on the template model after local registration and the refined landmarks on the new bone.

The femoral head ligament landmark on the new bone is also defined after initial global registration and local registration processes are completed (Figure 29). White landmark represents the initial position after initial global registration while the purple point is the refined landmark after local registration. Using this process, the femoral head ligament landmark before and after local registration are identical.

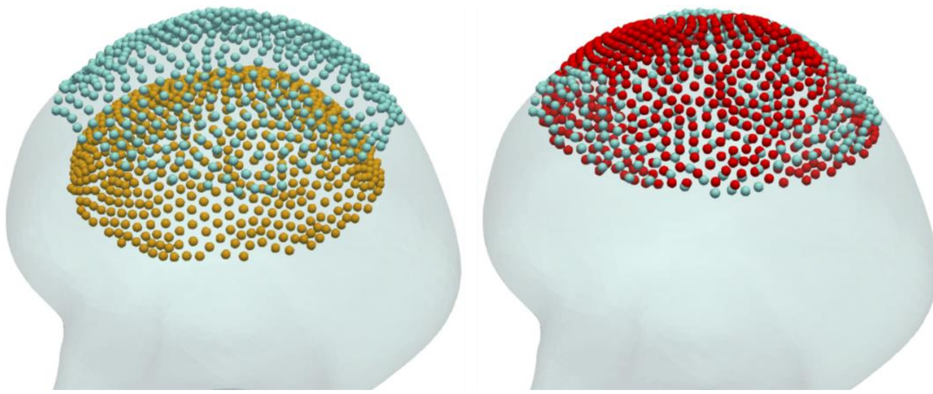

Figure 4-17: The corresponding regions on the femoral head before (left) and after (right) local registration. The cyan point cloud is vertices on the new bone. The orange point cloud is the corresponding vertices of the cyan point cloud on the template. The red point cloud is vertices of cyan point cloud after local registration.

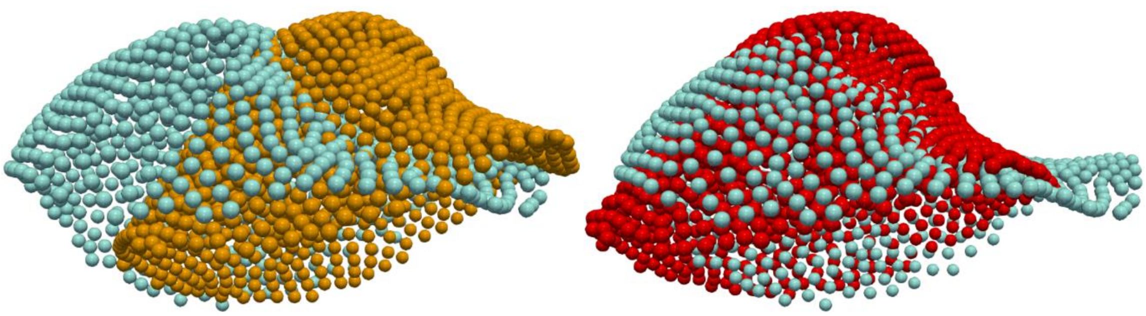

Figure 4-18: The corresponding regions around lesser trochanter before (left) and after (right) local registration. The cyan point cloud is vertices on the new model. The orange point cloud is the corresponding vertices of the cyan point cloud on the template. The red point cloud is vertices of cyan point cloud after local registration.

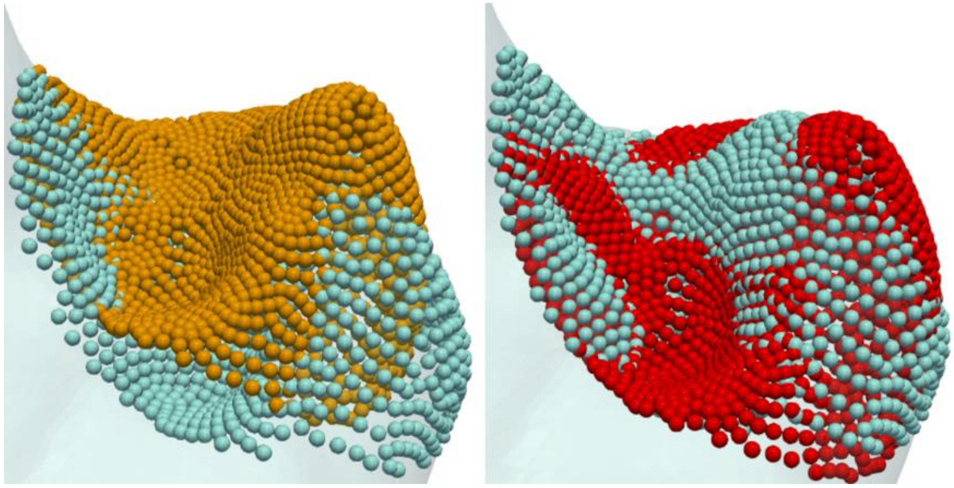

Figure 4-19: The corresponding regions around greater trochanter before (left) and after (right) local registration. The cyan point cloud is vertices on the new model. The orange point cloud is the corresponding vertices of the cyan point cloud on the template. The red point cloud is vertices of the cyan point cloud after local registration.

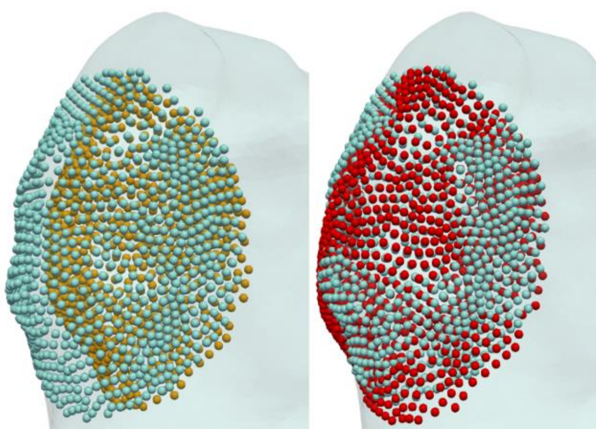

Figure 4-20: The corresponding regions around greater trochanter before (left) and after (right) local registration. The cyan point cloud is vertices on the new model. The orange point cloud is the corresponding vertices of the cyan point cloud on the template. The red point cloud is vertices of the cyan point cloud after local registration.

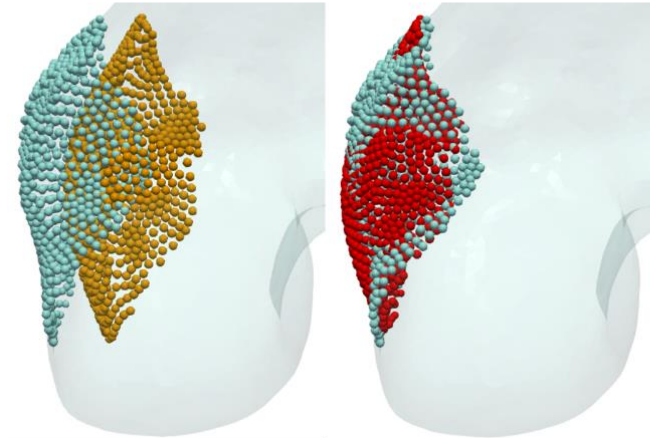

Figure 4-21: The corresponding regions around medial epicondyle before (left) and after (right) local registration. The cyan point cloud is vertices on the new model. The orange point cloud is the corresponding vertices of the cyan point cloud on the template. The red point cloud is vertices of the cyan point cloud after local registration.

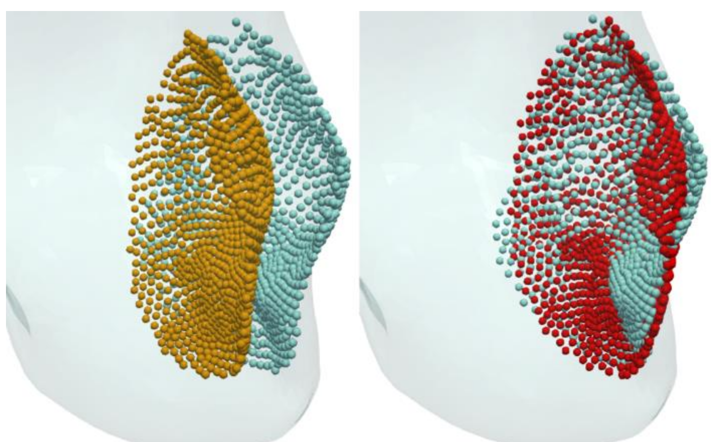

Figure 4-22: The corresponding regions around the lateral epicondyle before (left) and after (right) local registration. The cyan point cloud is vertices on the new model. The orange point cloud is the corresponding vertices of the cyan point cloud on the template. The red point cloud is vertices of the cyan point cloud after local registration.

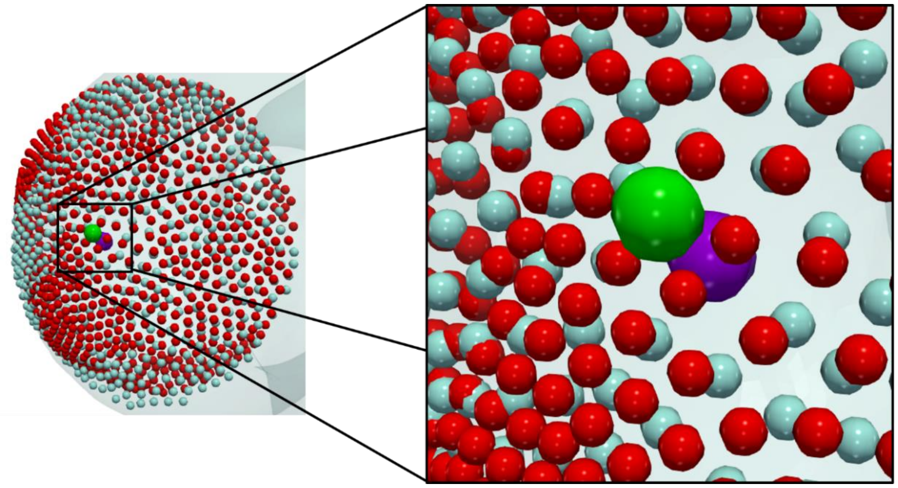

Figure 4-23: Refined femoral head ligament landmark of the new bone (purple) and the landmark on the template after local registration (green). Cyan point cloud represents the local region on the new model while the red one represents the local corresponding region on the template.

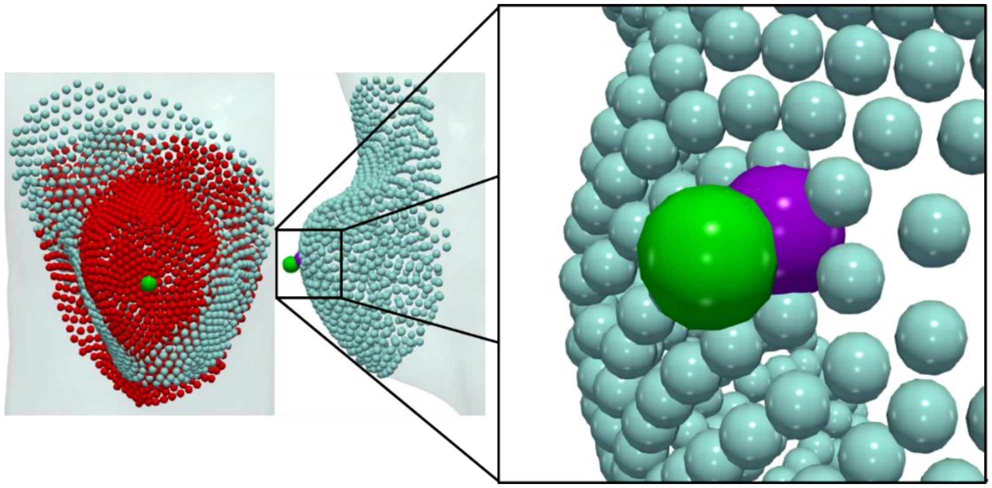

Figure 4-24: Refined lesser trochanter landmark of the new bone (purple) and the landmark on the template after local registration (green). Cyan point cloud represents the local region on the new model while the red one represents the local corresponding region on the template.

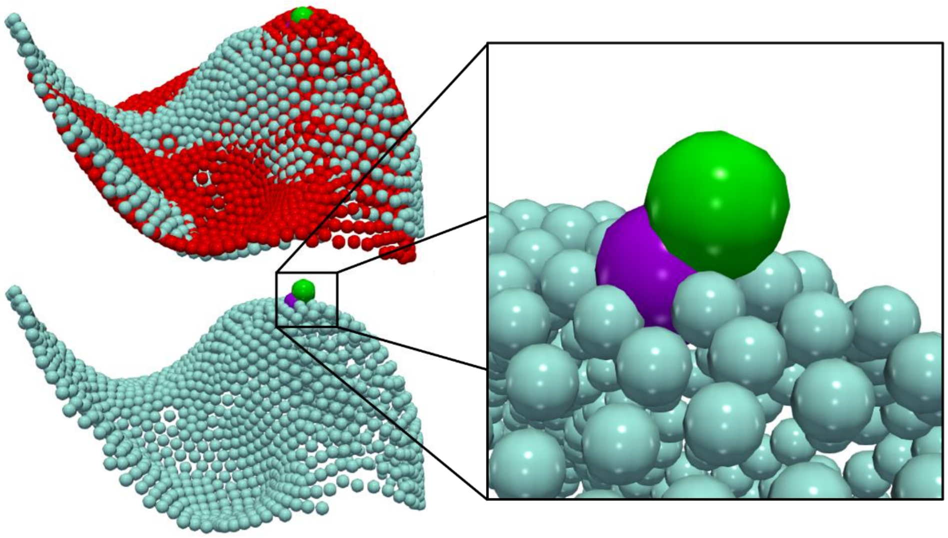

Figure 4-25: Refined greater trochanter landmark of the new bone (purple) and the landmark on the template after local registration (green). Cyan point cloud represents the local region on the new model while the red one represents the local corresponding region on the template.

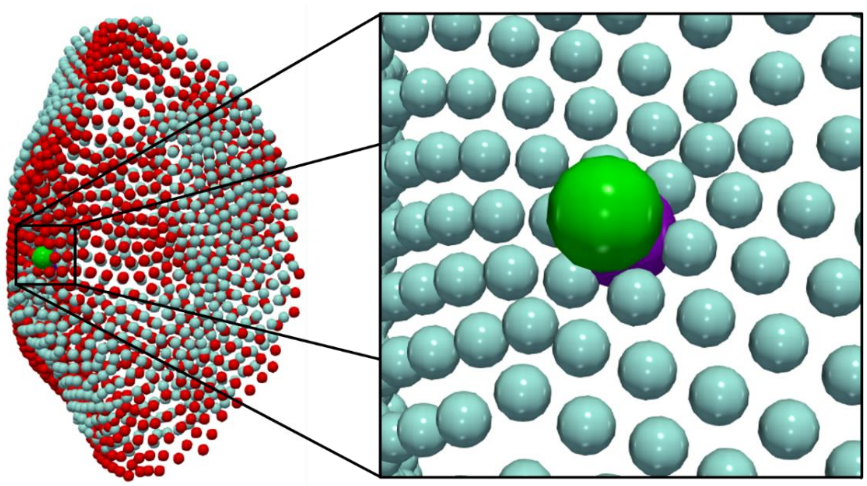

Figure 4-26: Refined greater trochanter landmark of the new bone (purple) and the landmark on the template after local registration (green). Cyan point cloud represents the local region on the new model while the red one represents the local corresponding region on the template.

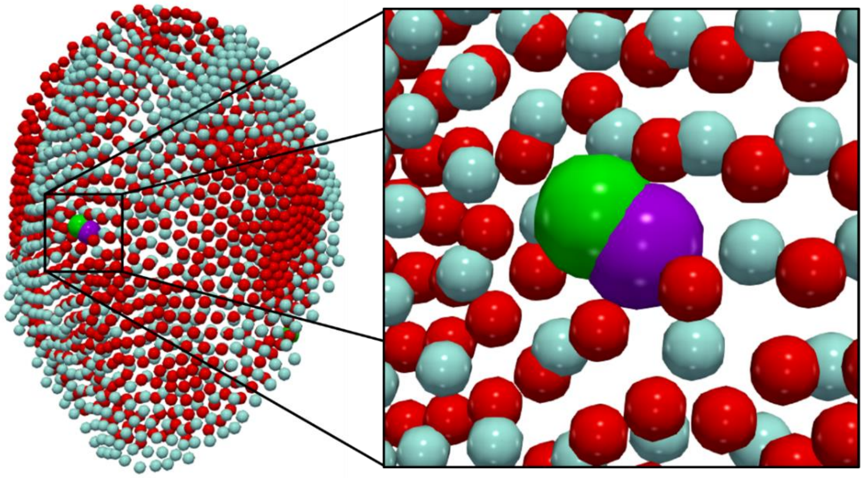

Figure 4-27: Refined medial epicondyle of the new bone (purple) and the landmark on the template after local registration (green). Cyan point cloud represents the local region on the new model while the red one represents the local corresponding region on the template.

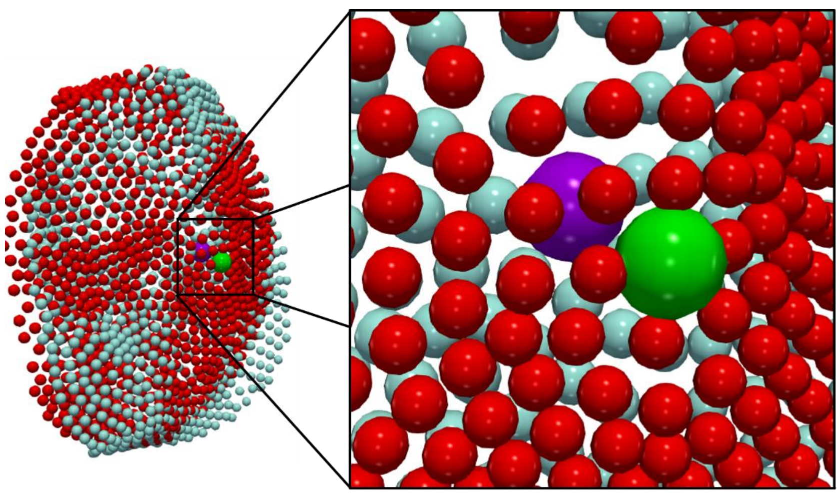

Figure 4-28: Refined lateral epicondyle of the new bone (purple) and the landmark on the template after local registration (green). Cyan point cloud represents the local region on the new model while the red one represents the local corresponding region on the template.

Figure 4-29: Comparison of refined (purple) and initial (white) femoral head ligament landmark on the new model. The blue point is the femoral head ligament landmark on the template model after local registration.

The lesser trochanter landmarks before and after local registration are also defined (Figure 30). The white landmark, slightly a further distance away, represents the location before local registration is completed, but the point is still close enough to the true landmark location. The local registration process is able to capture surrounding vertices, which can then be used to bring the white landmark closer to the purple landmark, which is closer to the landmark on the template bone (green).

Similar to femoral head ligament landmark, the medial epicondyle landmarks before and after local registration are very close. It can be seen that a small deviation between two landmarks is represented in Figure 4-31. As shown in Figure 4-32, lateral epicondyle landmarks before and after local registration is slightly off, but they are still very close to each other. At some regions, the final landmarks on the new bone are refined to match the landmarks on the template better. Those regions share a similar structure that is they contain more geometry details including curves, extreme points.

Regardless of differences in size, geometry, and initial position, the algorithm has proven to be successful in transferring landmarks from the template bone to the new bone model. It can be seen in Figure 4-33 that the predicted landmarks on the new model bone (purple) are properly defined with respect to the landmarks on the template bone (green).

4.1.7 Anatomical Landmarking for the Pelvis

Not only does this anatomical landmarking algorithm work for the femoral bone, but it can also be used for any bone geometry. Figure 4-34 shows the comparison of the template and new pelvis bones after initial global registration. Even though they are similar in structure, in some certain regions they are very different in geometry and size.

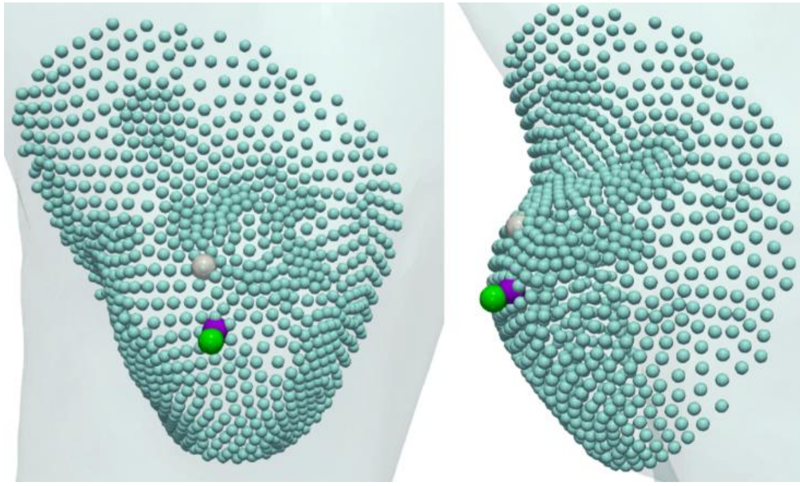

Figure 4-30: Lesser trochanter before (white) and after (purple) local registration. The green point represents the lesser trochanter of the template after local registration.

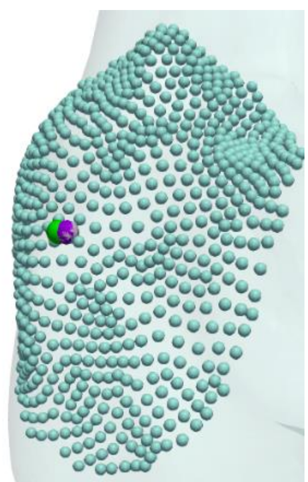

Figure 4-31: Medial epicondyle before (white) and after (purple) local registration. The green point is medial epicondyle of the template after local registration.

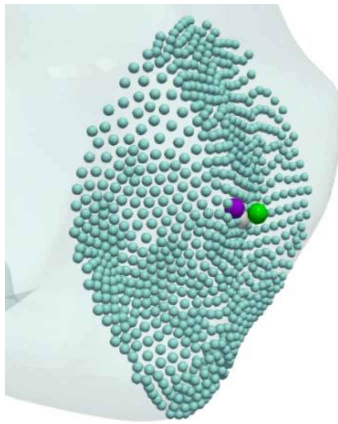

Figure 4-32: Lateral epicondyle before (white) and after (purple) local registration. The green point represents the lateral epicondyle landmark on the template after local registration.

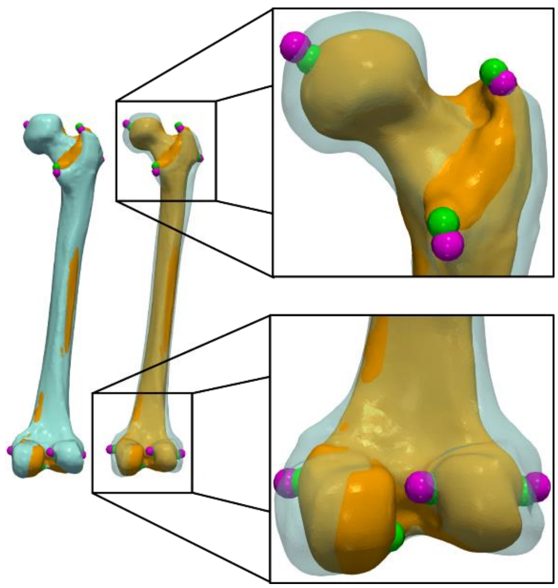

Figure 4-33: Landmarks on the template are successfully mapped to the new femur model using the proposed anatomical landmarking algorithm. The cyan model represents the new femur, while the orange model represents the template femur. Green points are landmarks on the template while purple points are landmarks on the new femur.

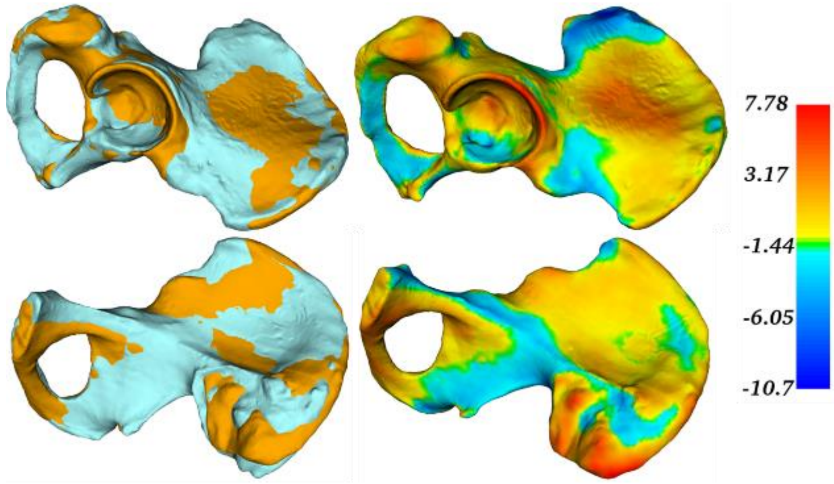

Figure 4-34: Comparison of the template (orange) and new pelvis (cyan) after initial global registration.

Figure 4-35 demonstrates the landmarks on the template pelvis bone are mapped to the new pelvis bone. Therefore, it can be seen that with the same algorithm, landmarks on the new model can be predicted and properly defined. This new algorithm accelerates the process of analyzing new subjects and avoids human error while determining new landmarks on the bone of new subjects used in the forward solution model.

4.2 MORPHOLOGY OF THE PROXIMAL FEMUR

After defining landmarks on the new femoral bone model, the landmark positions will then be used to analyze the femoral bone and canal to obtain the morphologic parameters (Figure 4-36). This crucial step aims to determine the following parameters of the proximal femur and canal.

1. Femoral head diameter (B)
2. Femoral head center
3. Femoral neck shaft axis
4. Femoral canal morphology
5. Proximal femoral shaft axis
6. Femoral offset (A)
7. Femoral neck shaft angle (C)

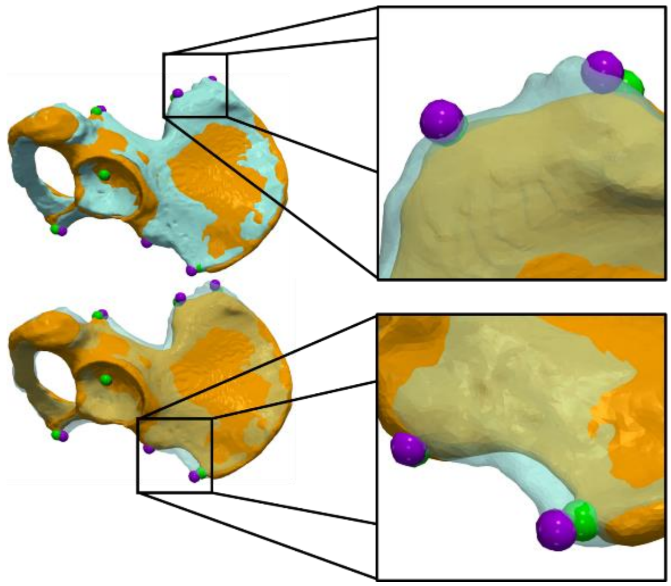

Figure 4-35: Landmarks on the new pelvis (purple) are successfully mapped from landmarks on the template femur (green).

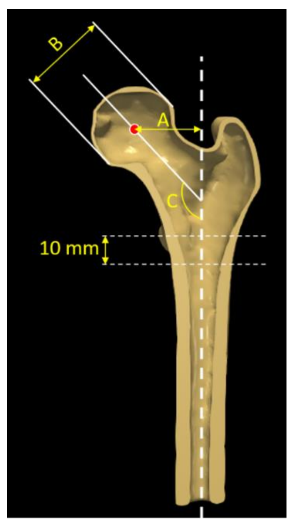

Figure 4-36: Proximal femoral morphology.

4.2.1 Algorithm Framework

The anatomical landmarking algorithm framework is revised in a specific manner so that it provides more information that can be used to determine the femoral morphologic parameters. The revised algorithm is shown in Figure 4-37.

Using this revised framework, additional information can then be added to the template femoral bone model. The mesh of the template femoral bone is segmented to smaller regions that contain important information pertaining to the femur. As described in Figure 4-38, the femoral bone is intuitively divided into six small regions: the femoral head, femoral neck, trochanter region, proximal femoral shaft, distal femoral shaft, and distal femur.

Also, the lesser trochanter landmark is defined and represented as the green sphere in Figure 4-38. The initial alignment and the initial global registration are performed in exactly the same manner as seen in the anatomical landmarking algorithm. After the initial global registration is completed, only three regions are necessarily used to determine the correspondences in the template femur bone and the new femoral bone model. The three regions previously referred to are the femoral head, femoral neck, and the region around the lesser trochanter. In Figure 4-39 and Figure 4-40 represention is shown for the correspondence of the femoral head and femoral neck after the initial global registration, respectively.

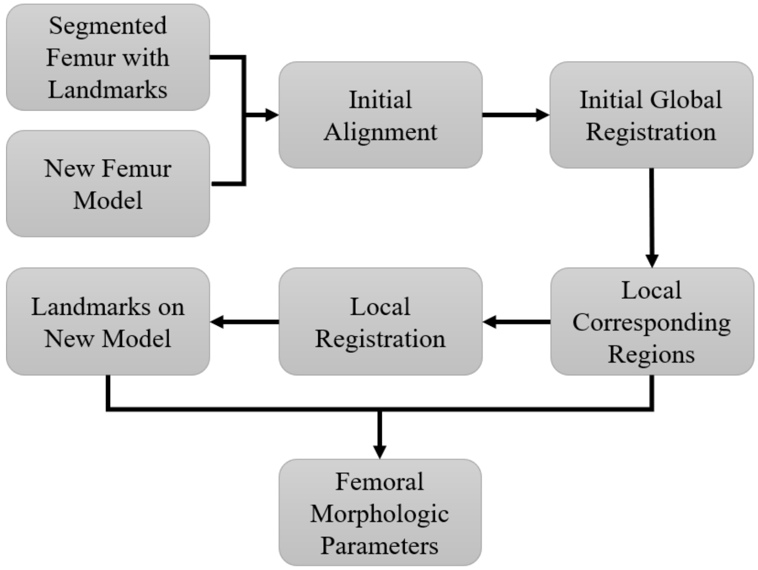

Figure 4-37: Measurement of the proximal femoral morphology framework.

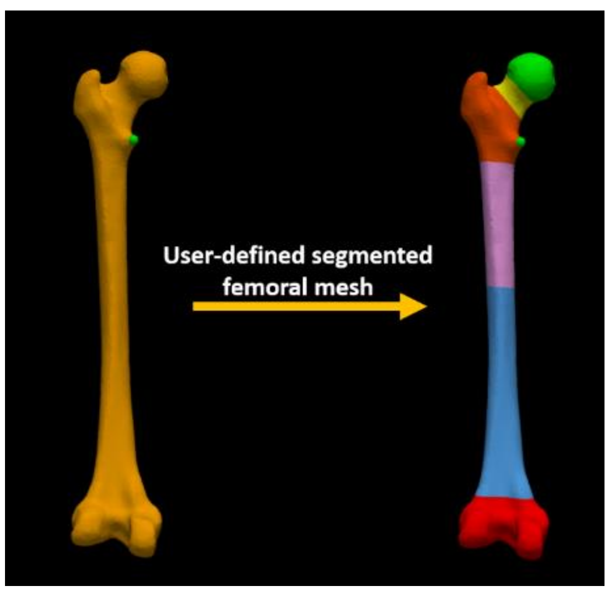

Figure 4-38: User-defined segmented mesh of the femur.

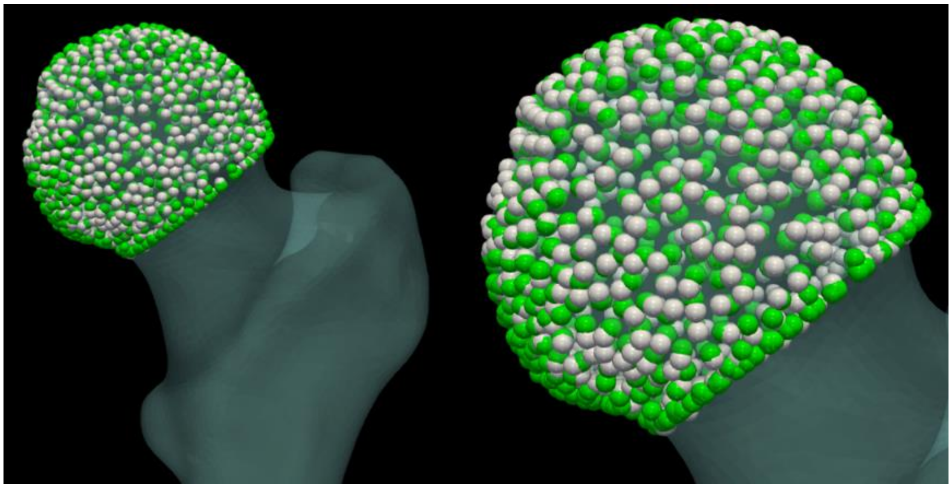

Figure 4-39: The corresponding regions of the femoral head on the template (green) and the new model (white).

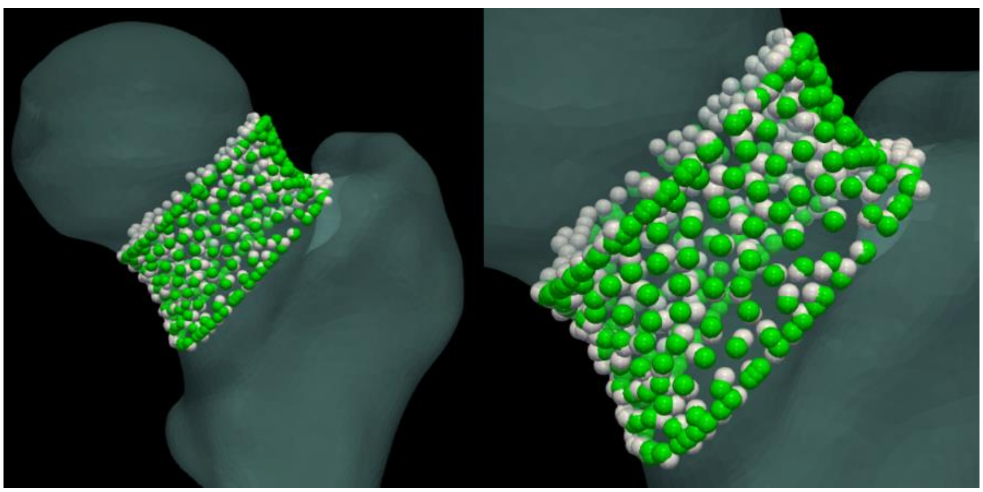

Figure 4-40: The corresponding regions of the femoral neck on the template (green) and the new model (white).

4.2.2 Determination of The Femoral Head Center and Diameter

Once the femoral head of the new femur bone is obtained, a spherical fitting function is used to fit the point cloud for the femoral head. The diameter of the femoral head is then determined to be the diameter of the fitting sphere. The fitting sphere of the femoral head, given its point cloud is shown in Figure 4-41.

Since the femoral head is not a perfect sphere, the spherical fitting function is run multiple times to account for artifact error. Each run generates a fitting sphere pertaining to the femoral head point cloud. The final sphere, representing the femoral head, is determined to be an average sphere with respect to all the spheres derived from each run of the process. The sphere for each run, pertaining to the femoral head, its center and the diameter of this sphere are recorded for each run. The final femoral head center and diameter are calculated as the mean of the fitting centers and diameters. The mean fitting sphere with respect to the femoral head, with point cloud and without point cloud, respectively are shown in Figure 4-42 and Figure 4-43.

4.2.3 Determination of The Femoral Neck Shaft Axis

Similar to the determination of the femoral head information, a cylindrical fitting function is used, instead of a spherical fitting function, to fit a cylinder to the point cloud of the femoral neck. Again, the point cloud of the femoral neck is not representing by a perfect cylinder, so the algorithm runs multiple times to estimate the mean cylinder. The procedure is carried out using a variant of the Random Sample Consensus (RANSAC) called M-estimator RANSAC [76]. RANSAC is an iterative method to estimate parameters of a mathematical model from a set of observed data that contains outliers or noise. In this

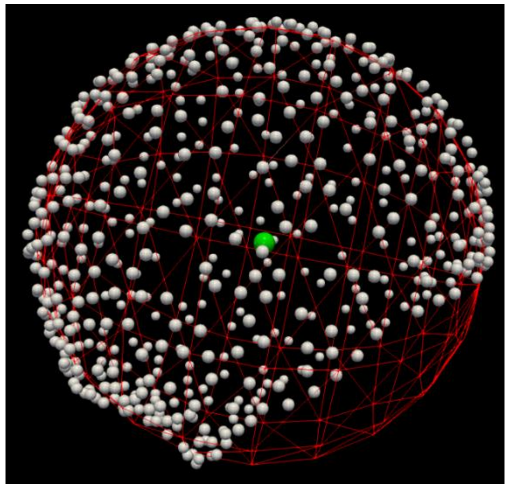

Figure 4-41: A fitting sphere is used to fit the point cloud of the femoral head.

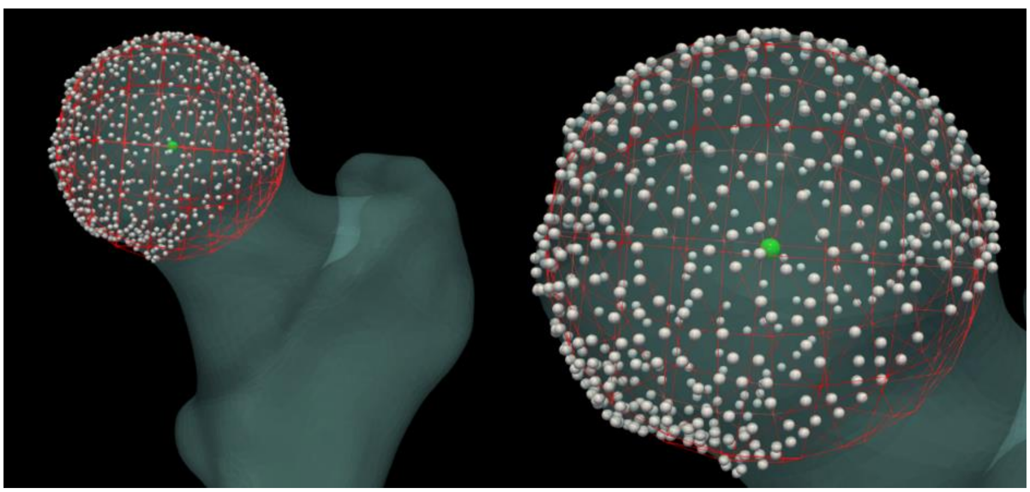

Figure 4-42: The mean fitting sphere of the point cloud of the femoral head.

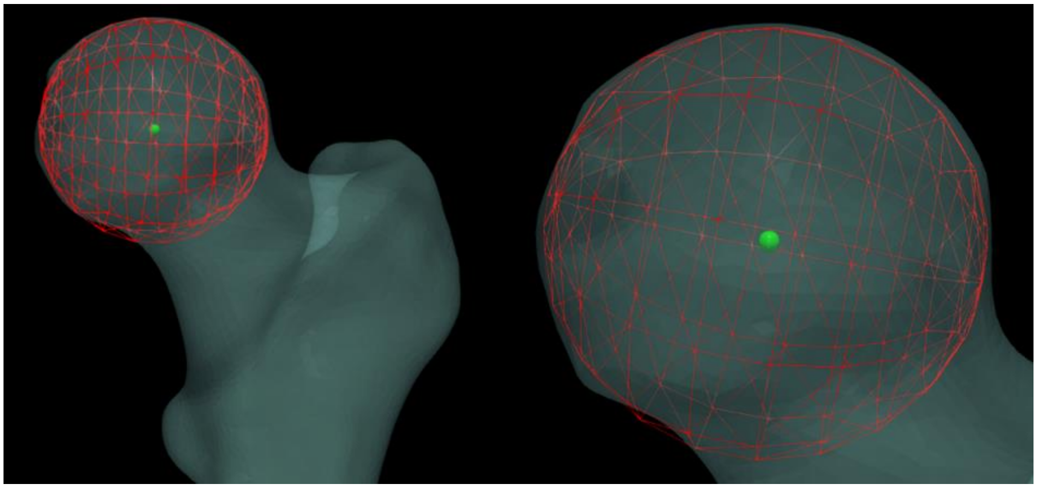

Figure 4-43: The mean fitting sphere of the point cloud of the femoral head.

application, the mathematical model is a cylindrical fitting function. The point cloud of the femoral neck plays an important role, as the derived data is used to fit a cylinder (mathematical model). M-estimator of RANSAC suggested by Torr et al. [77] provides a modification of the RANSAC algorithm to reduce the effect of noise and outliners. This is a random process, so after each run, the M-estimator RANSAC yields a different result of the mathematical model. With respect to the cylindrical fitting function, after each run, the algorithm generates a different set of cylindrical parameters. A set of parameters that are needed to define a cylinder includes centers of both sides of the cylinder, the radius, and the height. After multiple runs, a set of cylindrical parameters are recorded. The final fitting cylinder is estimated to be the mean of all fitting cylinders after all runs.

The femoral neck shaft axis is then determined to be the axis that goes through two centers of two sides of the mean cylinder. As the center of the femoral head and the axis of the femoral shaft are estimated separately, it is likely that the estimated femoral head center will not lie on the femoral neck shaft axis. In order to correct that problem, additional steps are carried out. Before discussing how this problem is fixed, let us review how a line is formed. On the Cartesian plane, a line is represented as two points or a unit vector and a point. The unit vector represents the direction while the point can be any certain point that bisects the line. Two lines are determined to be parallel when they share the same unit vector, although the points can be different from each other. With respect to the representation of the femoral neck shaft axis, it is represented as two center points on two sides of the cylinder or can be represented as a unit vector and a point. Therefore, the refined femoral neck shaft axis is determined by keeping the unit vector of the mean femoral shaft axis the same as the mean femoral neck shaft axis, which is shifted to include the femoral head center. The femoral neck shaft axis before and after the correction is completed are shown in Figure 4-44.

4.2.4 Measurement of Femoral Canal Morphology

Measurement of femoral canal morphology is performed through four steps, which are described as follows:

Step 1: Multi-plane intersection

Starting from 10 mm below the lesser trochanter landmark location, multiple slices in the same plane, that are parallel to each other (equally spaced at 1 mm thickness), and parallel to the transverse plane, are used to intersect with the canal to obtain a set of canal boundary contours. A canal boundary contour is a set of 3D point clouds, but in each slice, the contour is represented as a 2D point cloud. The canal boundary contours in 3D view and 2D view (Top View) are shown in Figure 4-45.

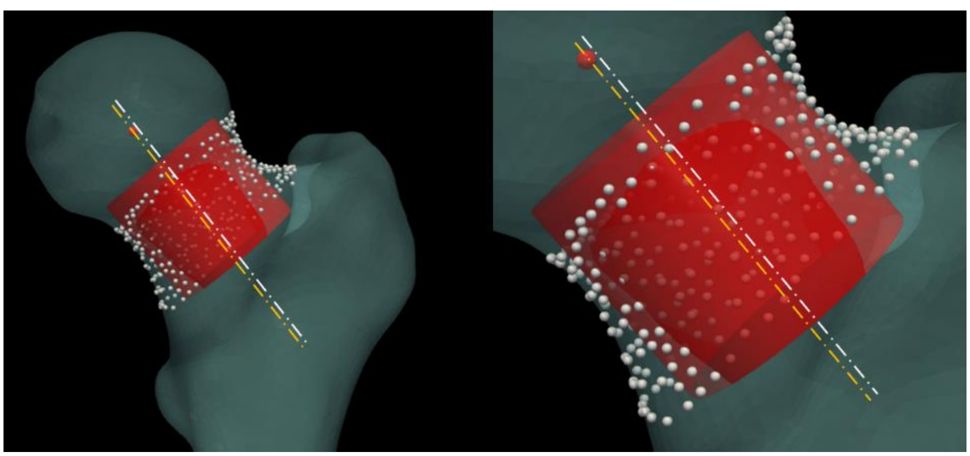

Figure 4-44: Femoral neck shaft axis before (white) and after (orange) correction.

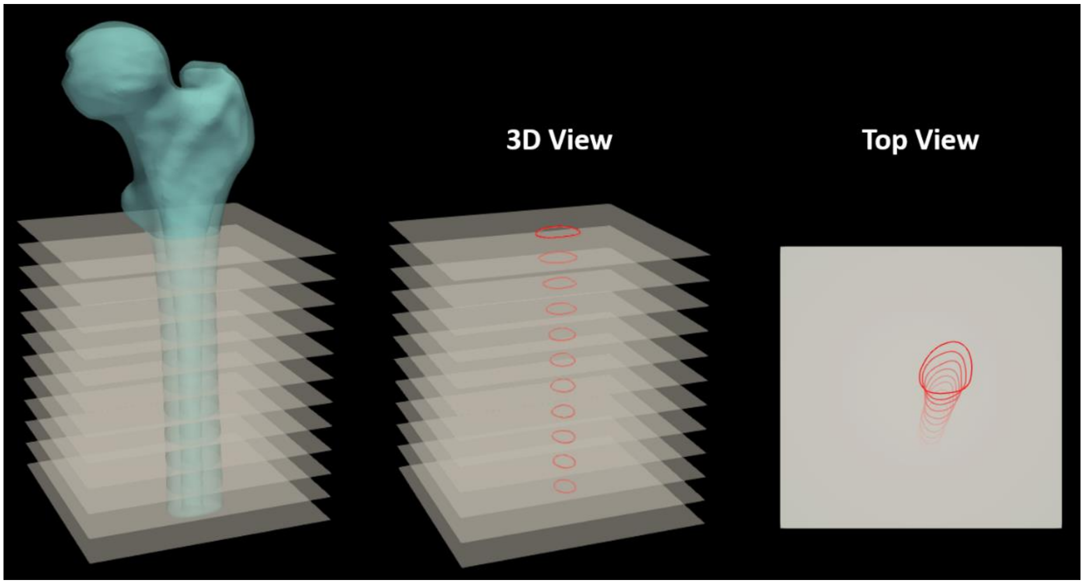

Figure 4-45: Multiple planes are used to slice the femoral canal to obtain a set of canal boundary contours.

Step 2: Determination of incircles of the canal boundary contours

The position of each slice in the plane is recorded with respect to the global coordinate system. In each slice, the canal boundary contour is represented as a set of 2D points. For each canal boundary contour in a certain slice, an incircle is determined to be the largest circle that fits inside the canal boundary contour. This incircle represents a virtual space where a femoral stem can rotate around its shaft axis. Therefore, assuming that a femoral stem fits inside the canal, the femoral stem can then be rotated to find the best fitting position for each slice in the chosen plane. Then, the boundary of the femoral component will draw a circle trajectory inside the canal. Therefore, the incircle of the canal will work as a constraint that only allows smaller circle trajectories to fit inside. The canal boundary contour and its incircle at an arbitrary plane are shown in Figure 4-46.

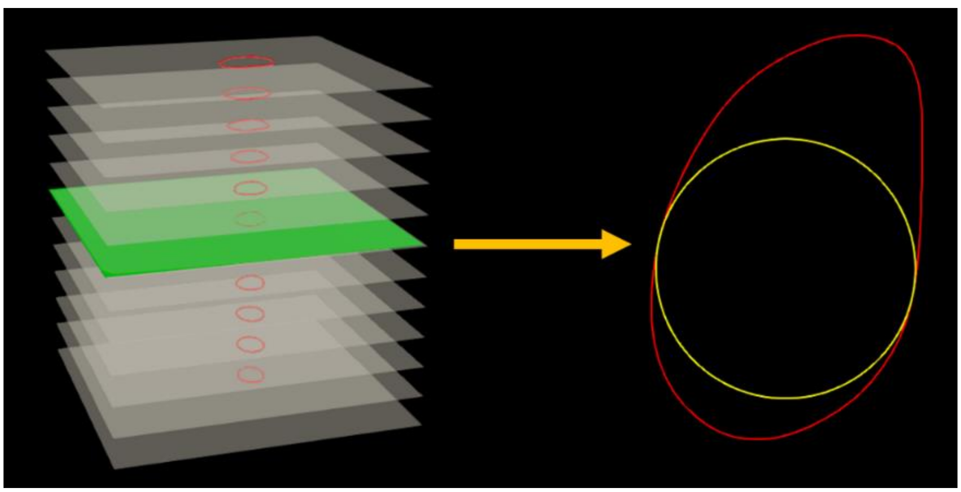

Figure 4-46: At an arbitrary plane, an incircle (yellow) of a canal boundary contour (red) is defined as the biggest circle that can fit inside the canal boundary contour.

This process is repeated for all slices in the chosen plane through to the proximal femur. A set of canal boundary contours and their incircles are recorded for further analysis. The canal boundary contours and their incircles are obtained for the entire proximal femur are shown in Figure 4-47.

Step 3: Determination of incircles' centers and radii

All centers and radii representing the incircles are stored in a module library. The module library is define in a manner, such that the center location of the incircle closest to the femoral head center will be recorded first, and the furthest incircle defined last. By doing this in such a way creates virtual storage that is likely similar to the canal shape. The centers of incircles and their radii are shown in Figure 4-48.

Step 4: Measurement of the distances from the femoral head center to each center of incircles

As the coordinates of the femoral head center and centers of incirles are determined in the global coordinate, the relative distance from each incircle center to the anatomical femoral head center is obtained by subtracting the distances from the two coordinates. The relative position of the centers of incircles to the anatomical femoral head center are represented in Figure 4-48.

4.2.5 Determination of The Proximal Femoral Shaft Axis

Once the centers of all the incircles are determined, the proximal femoral shaft axis is determined by fitting a line to all the center locations. In the previous section, the RANSAC algorithm [77] was used to determine a fitting cylinder to the femoral neck. In

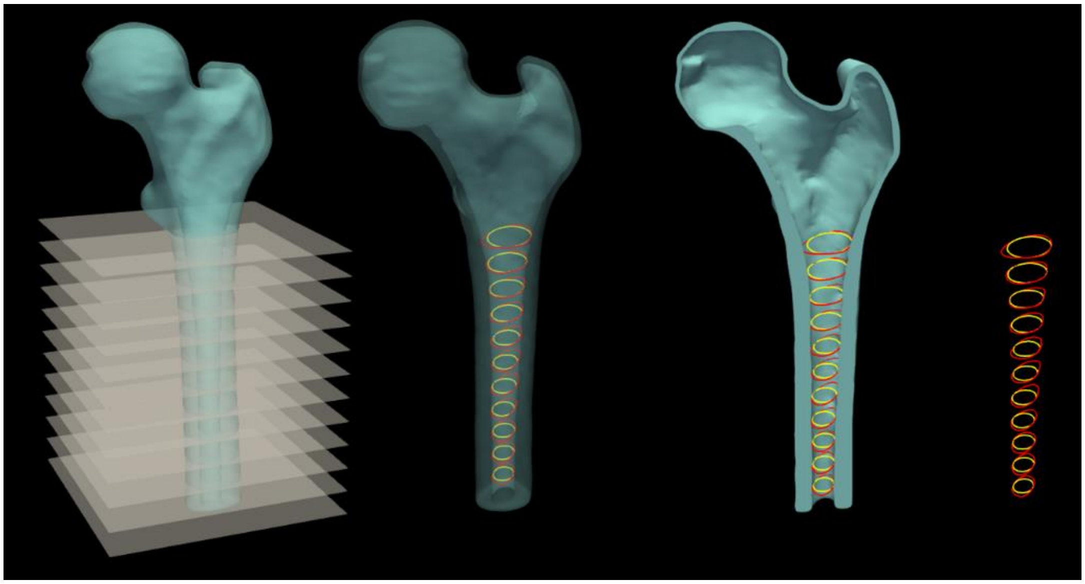

Figure 4-47: Incircles of all canal boundary contours are obtained.

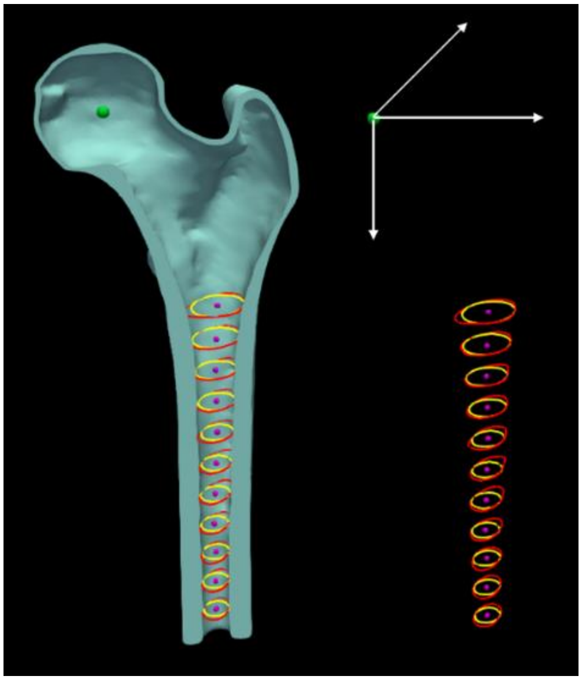

Figure 4-48: The center and radius of each incircle are recorded.

this section, the RANSAC algorithm is also used but for fitting a line. The superiority of the RANSAC algorithm over other regression models is that the RANSAC algorithm is very efficient to determine a fitting line with noisy input data. Similar to the representation of the femoral neck shaft axis, the femoral shaft axis is also represented using a unit vector and a point. The estimated femoral shaft axis is defined in Figure 4-49 using the RANSAC algorithm.

4.2.6 Measurement of The Femoral Offset

The femoral offset plays an important role for determining whether a standard or high offset femoral stem is needed for a specific patient requiring a total hip arthroplasty. The femoral offset is defined as the distance from the femoral head center to the proximal femoral shaft axis. As the femoral head center and femoral shaft axis are determined in the previous sections, the calculation of the femoral offset is straightforward. The femoral offset is shown in Figure 4-50.

4.2.7 Measurement of Femoral Neck Shaft Angle

As the femoral neck shaft axis and femoral shaft axis are calculated in the previous sections, the femoral neck shaft angle is determined as the angle between those axes. The femoral neck and shaft angle are shown in Figure 4-51.

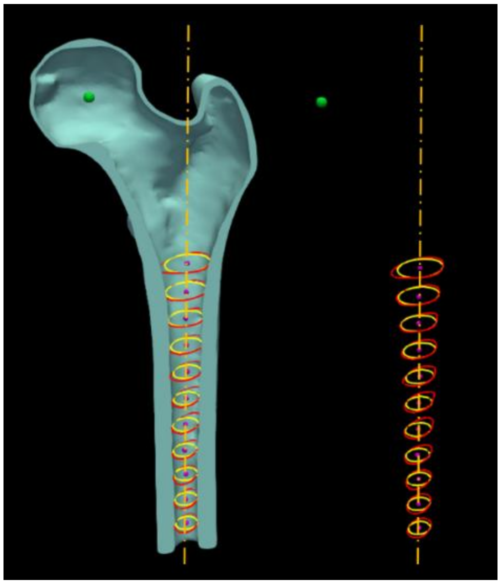

Figure 4-49: The proximal femoral shaft axis is defined to be the fitting line that bisects all incircle centers.

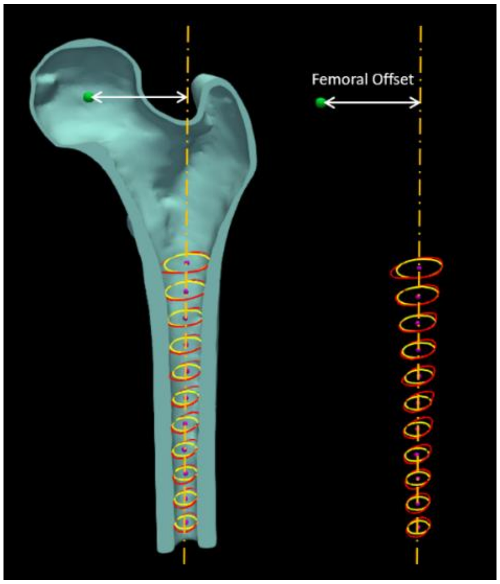

Figure 4-50: Femoral offset is measured as the distance from the femoral head center to the proximal femoral shaft axis.

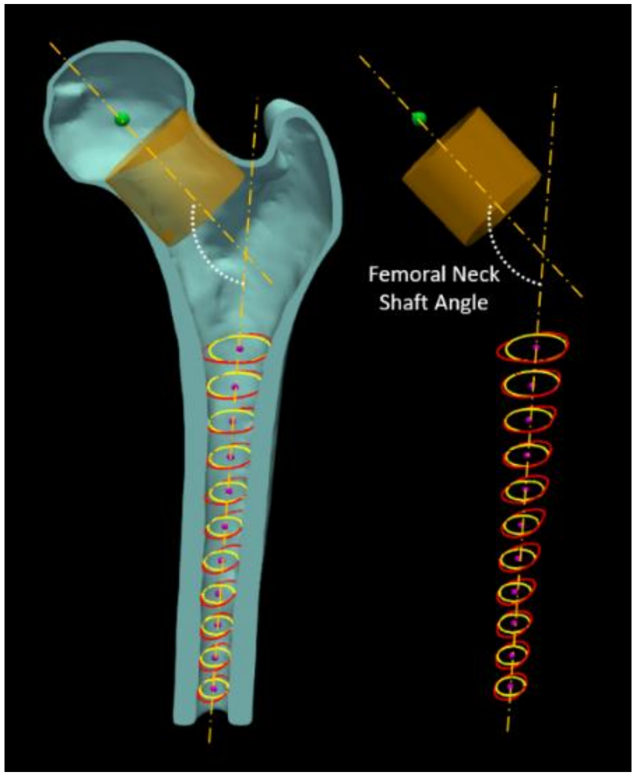

Figure 4-51: Femoral neck shaft angle is measured as the angle between the femoral neck shaft axis and the proximal femoral shaft axis.

4.3 AUTOMATED TOTAL HIP ARTHROPLASTY SIZING PREDICTION

4.3.1 Measurement of Femoral Component Morphology

Measurement of the femoral component morphology needs to be differentiated from the femoral component specification. The femoral component configurations contain five parameters, which are stem length, neck offset, neck length, neck shaft angle, and component width. A standard Corail total hip arthroplasty stem will be used in this section (Figure 4-52).

The objective pertaining to the morphology of a femoral component is to provide meaningful information that can be used to determine how the femoral stem fits the canal. Similar to the femoral canal morphology measurement, there are five steps to measure the morphologic parameters of a femoral component. Using a similar approach, only that contents that differ from the canal analysis are discussed in this section.

Step 1: Preparation of the training implant database

Similar to anatomical landmarking that automatically predicts landmarks on a new bone model given a known set of landmarks on a template model, the objective of this step pertains to obtaining two defined landmarks on each femoral component. These landmarks are the femoral head center and the distal aspect of the collar, commonly referred to as the collar landmark. For collarless femoral stem components, the landmark becomes the lowest point of the boundary that separates the component's neck and shaft. Since it can be difficult to determine these features on a femoral component using an automated process,

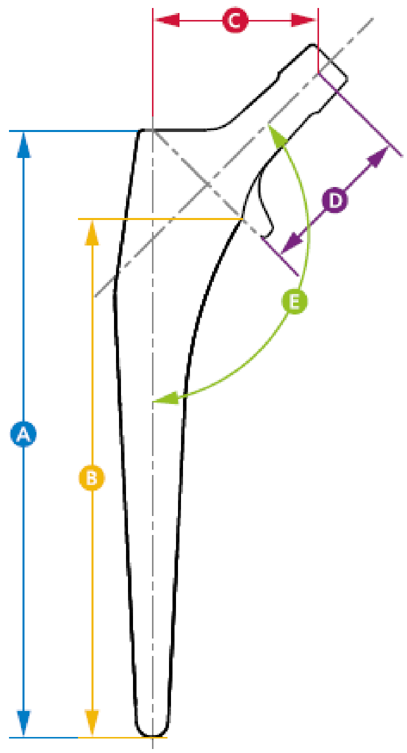

Figure 4-52: Corail stem specification that contains stem length (A & B), offset (C), neck length (D), and neck shaft angle (E). Image from (www.depuysynthes.com)

it is recommended that two landmarks be manually selected and saved in a text file. The femoral head center and the most distal aspect of the femoral collar, in a standard collared femoral component are shown in Figure 4-53. Two landmarks are selected and stored in separate text files for all of the femoral components that are stored in the database.

Step 2: Multi-plane intersection

Similar to the femoral bone in the anatomical landmark module, starting at 1 mm below the collar landmark, multiple parallel planes are defined in the chosen plane and also with respect to the transverse plane. These planes spaced at 1 mm thickness with respect to each other are used to intersect with the femoral component to obtain a set of the femoral component boundary contours. Similar to the canal morphology measurement section, the boundary contours are 3D curves, but in each plane, they are represented as 2D curves. The position of each plane is also obtained to locate its position with respect to the global coordinate. In Figure 4-54, the multi-plane intersection with the femoral component can be seen.

In Figure 4-55 the multiple defined planes, separated by1 mm thickness intersection with the femoral component can be seen. The process is able to capture the boundary of the femoral component even with limited details.

Step 3: Determination of circumcircles for all intersected femoral component contours

Unlike the femoral canal analysis section where an incircle is determined for each canal contour, a mating circumcircle is determined for each femoral component contour. A circumcircle is defined to be the smallest circle that contains all the femoral component

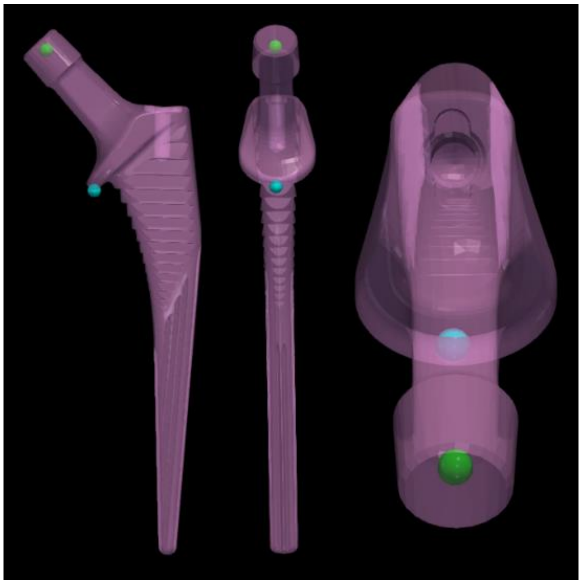

Figure 4-53: The femoral stem head and collar landmark are manually defined.

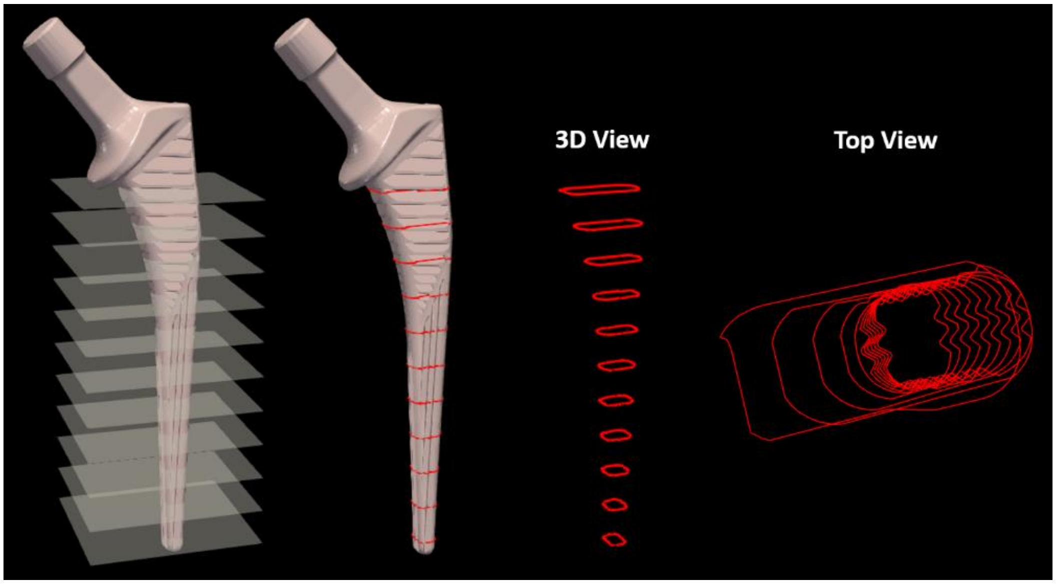

Figure 4-54: Multiple planes are used to slice the femoral component to obtain a set of the boundary contours.

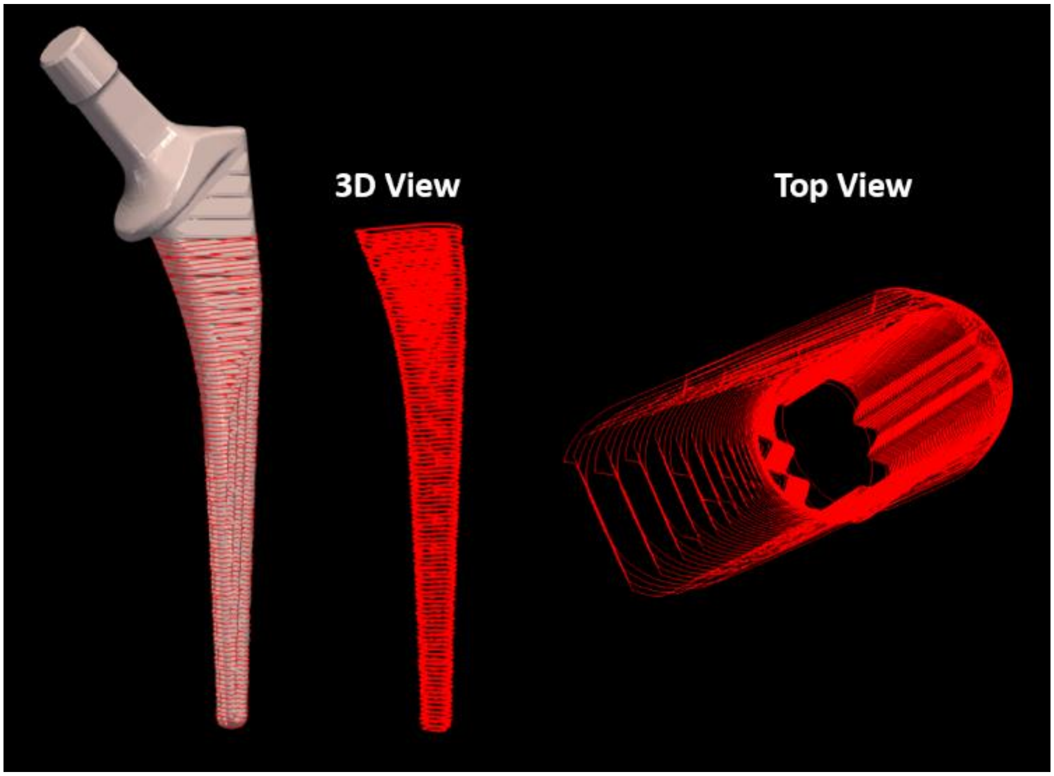

Figure 4-55: Multiple planes with 1 mm thickness are used to intersect the femoral component to obtain detailed component boundary contours.

contour points. An example of the circumcircle for a defined slice of the femoral component contour at a certain plane is shown in Figure 4-56.

A circumcircle is used instead of incircle for this process because if the femoral component rotates about its shaft axis within the femoral canal, whereas the defined boundary, represented by a slice, represents a circle. This circle is a known to be a circumcircle of the femoral component boundary at each specific slice in the plane. A circumcircle provides meaningful information with respect to the femoral component contour at each slice defined by the points representing its circumference. Therefore, this information is used to determine how far each stem can fit within the femoral canal. A specific set of circumcircles is then identified for each femoral component by using the contours at each slice. Those circumcircles form the morphology of a given femoral component. The circumcircles obtained at each slice are shown in Figure 4-57.

Step 4: Determination of the centers and radii of circumcircles

Similar to the femoral canal analysis section, all centers and radii representing the set of circumcircles for each stem are recorded and stored in the module library. The circumcircle closest to the femoral neck head center (where the center of the femoral head will locate on the femoral neck) will be stored first and subsequently all other circumcircles with one representing the furthest distance from the femoral neck head center, stored last. The centers and radii of all circumcircles is shown in Figure 4-58.

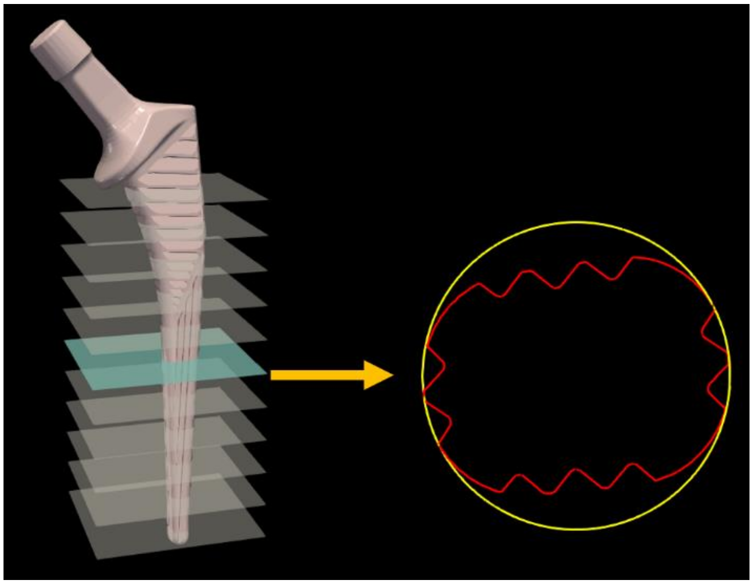

Figure 4-56: Circumcircle of a contour at a certain plane is defined as the smallest circle that contains all contour points.

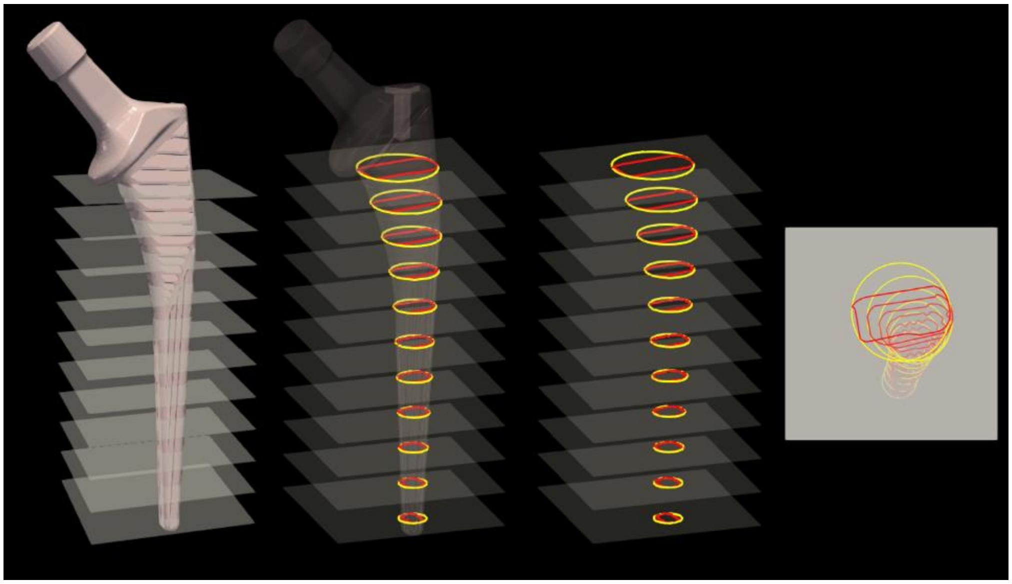

Figure 4-57: Circumcircles are identified for all contours at all planes.

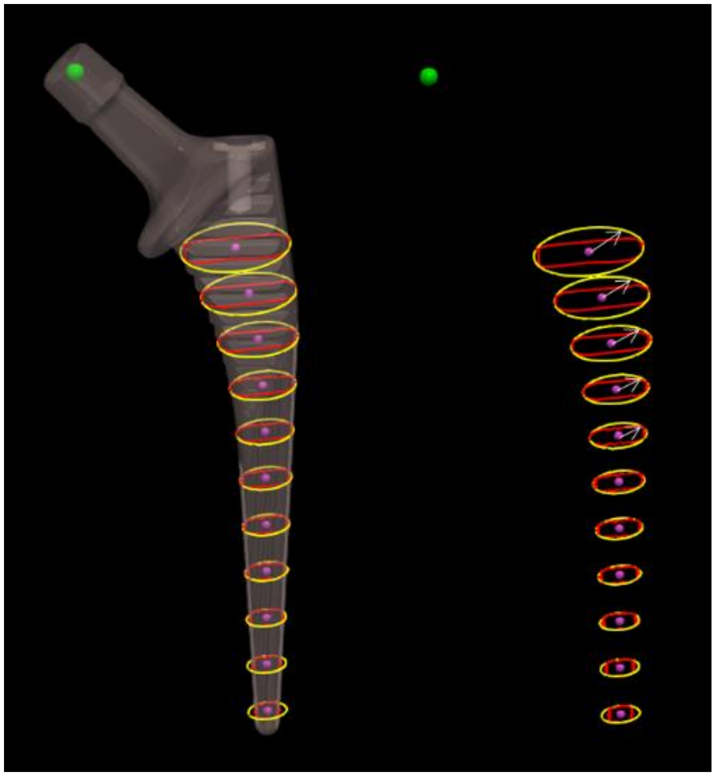

Figure 4-58: Centers and radii of all circumcircles are obtained.

Step 5: Measurement of distances from each circumcircle to the femoral component head center

As the coordinates of the femoral component head center and centers of circumcircles are determined in the global coordinate, the relative distance from each circumcircle to the component head center is obtained by subtracting the distances from the two coordinates. Those parameters are defined and stored in the above stack to add to the morphologic parameters of the femoral component.

Step 6: Determination of the stem shaft axis

Unlike the femoral canal, where the shape of each canal slice is not homogenously smaller from the most proximal to the most distal slice, the radii of the circumcircles of the femoral component do gradually reduce proximally to distally. Therefore, a meaningful methodology can be determined to define the axis of the femoral stem body. As shown in Figure 4-58, the shape of the femoral component does change proximally to distally where the shape allows for bone ingrowth and fixation. Beyond this point, the shape is reduced in a more constant manner. Although we define numerous slices and centers, in order to determine the femoral component shaft axis, only a small portion of the distal component is required. A line is the defined bisecting the distal centers of the circles and this line represents the stem axis. Therefore, the femoral stem axis is determined to be the best fitting line that bisects those centers (Figure 4-59)

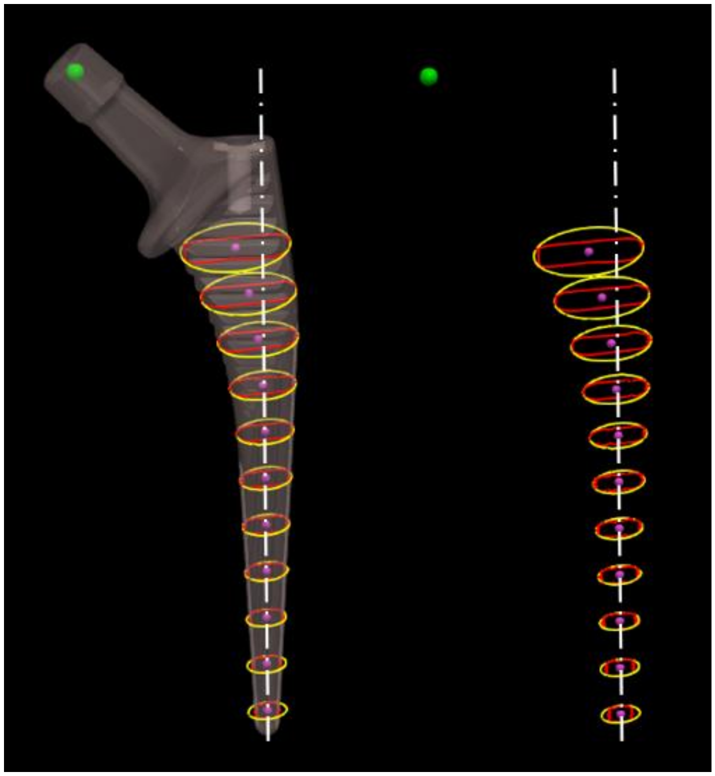

Figure 4-59: Femoral component shaft axis is defined as the fitting line that goes through all centers of circumcircles.

4.3.2 Femoral Component Sizing Algorithm Framework

The algorithm that is used to determine which femoral component will fit a specific femoral canal best, using a 3D mesh model of the femur, is shown in Figure 4-60.

The femoral component and canal morphology of a given femoral CAD model are compared to the training femoral component database. For each femoral component morphology, the algorithm determines how far distally the femoral component can fit within canal before collision is detected between the stem and the cortical bone. Once the defined position of where the femoral component can fit properly within the canal is confirmed, the relative distance from the anatomical femoral head center to the femoral component head center is calculated. This process is repeated for all femoral component morphology in the database. The best fitting femoral component is determined when the distance from its head center to the femoral head center is at a minimum.

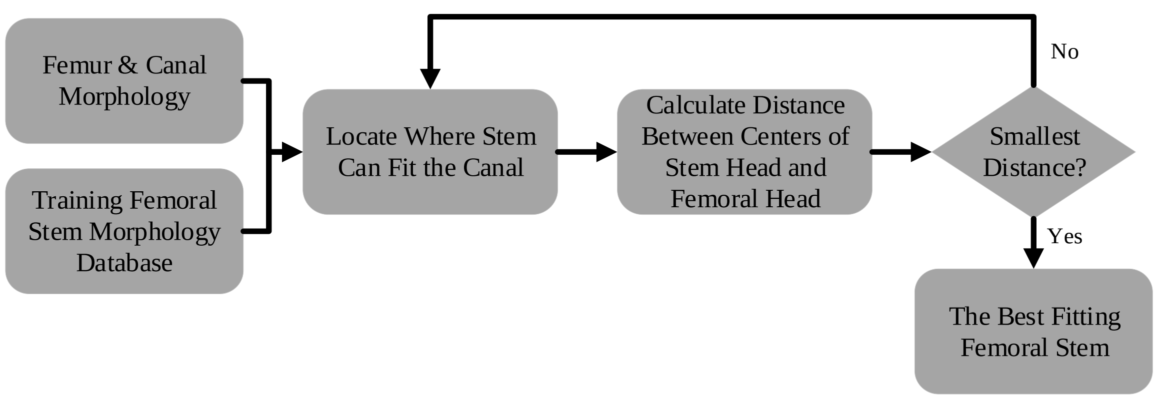

Figure 4-60: The femoral component sizing algorithm framework.

4.3.3 Determination of the Fitting Location Between the Femoral Component and Canal

The following important question must now be asked: For each femoral component that is stored in the database, how well can they fit within the canal? Previously we defined the incircles of the canal and circumcircles of the femoral component and now they are used for the femoral component fit process (Figure 4-61). The incircles and circumcircles represent the femoral canal and femoral component's morphology, respectively and are further used to determine which femoral stem fits best in the canal.

There are two solutions that can be used to address the stem fit. The first solution, as well as the most common thought of majority of readers, is inserting the femoral component within the canal and allow for the gravitational force to take effect, fitting the femoral component. The chosen stem would then be the one where the position of the femoral component can fit most stable within the canal. From a mathematical perspective, this solution can be written as comparing each circumcircle of the femoral component to the biggest incircle of the canal. The matching of circumcircle and incircle will reveal the position where the femoral component can fit best within the canal. On the other hand, the second solution that has been developed in this section compares the largest incircle to the circumcircles of the femoral component (Figure 4-62). These two solutions do share a common methodology, but the second solution can detemine which stem fits best using only a few comparisons. A demonstration of this the idea of solution two where the biggest incircle is compared to the circumcircles of the femoral component.

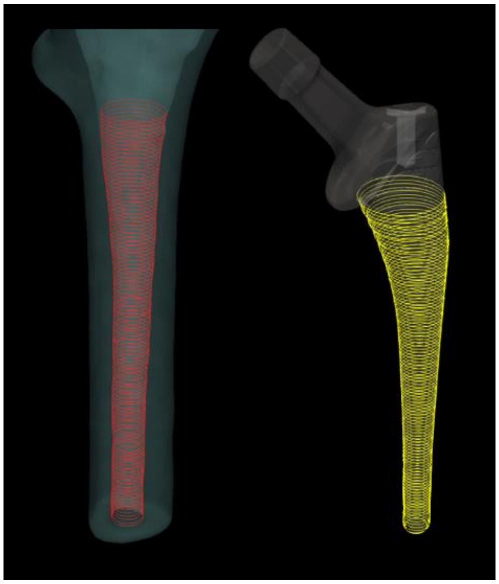

Figure 4-61: Incircles of the canal and circumcircles of the femoral component.

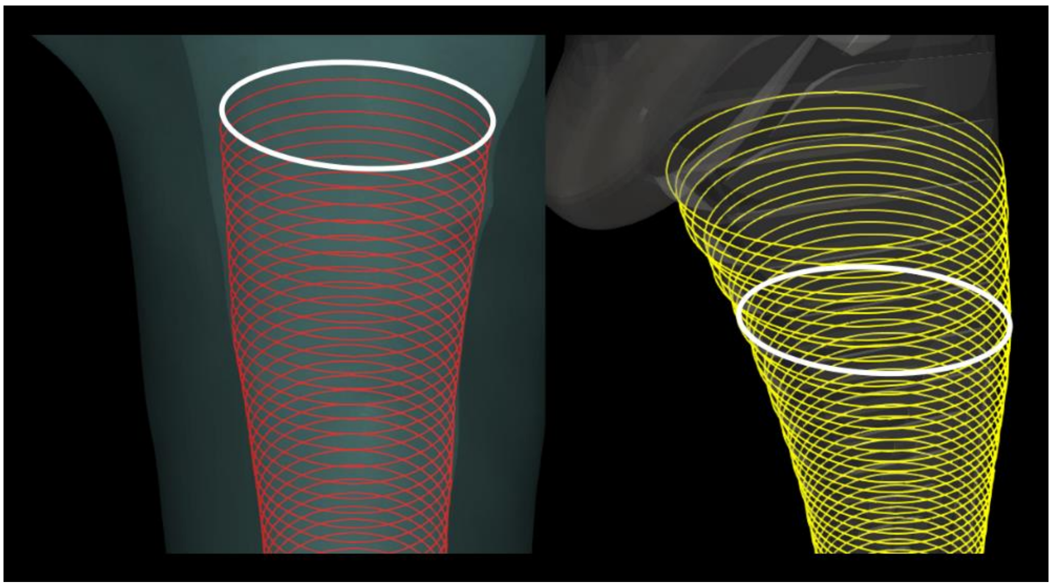

Figure 4-62: The biggest incircle of the canal is compared to the circumcircles to locate the fitting location of the femoral component and the canal.

4.3.4 Determination of the Smallest Distance

Once the position for each femoral component with the database fits with the canal is determined, the distance from its implanted head center to the anatomical femoral head center is then measured. Therefore, for all femoral components in the database, the set of distances from each femoral component head center to the anatomical femoral head center is determined and stored in the database. This process is conducted to find the best fitting femoral component within the canal by determining which femoral component has the smallest distance from its head center to the anatomical femoral head center. Since the distances for each implant size are recorded, the computer algorithm can then choose the best fitting stem. This is done by using minimization function that can be used to locate which femoral component fits best in the canal within having stem-bone collision and stem-bone gaps. Figure 4-63 shows the comparison of femoral components with different sizes sitting on the canal. The femoral component is outlined by a rectangular is the one with the smallest distance between its head center to the anatomical femoral head center.

4.3.5 The Choice of a Standard or High Offset Stem

Even though the best fitting femoral component was determined in the previous section, it is still necessary to consider whether that femoral component should be a standard or high offset stem. Orthopaedic manufacturers routine design two femoral component options with the same body characteristics, which are defined to be the standard offset and high offset stem. The only difference between two component designs is that with the same size of stem body, the high offset stem has a longer neck than the standard stem. The high offset stems account for the majority of patients, having a femoral offset

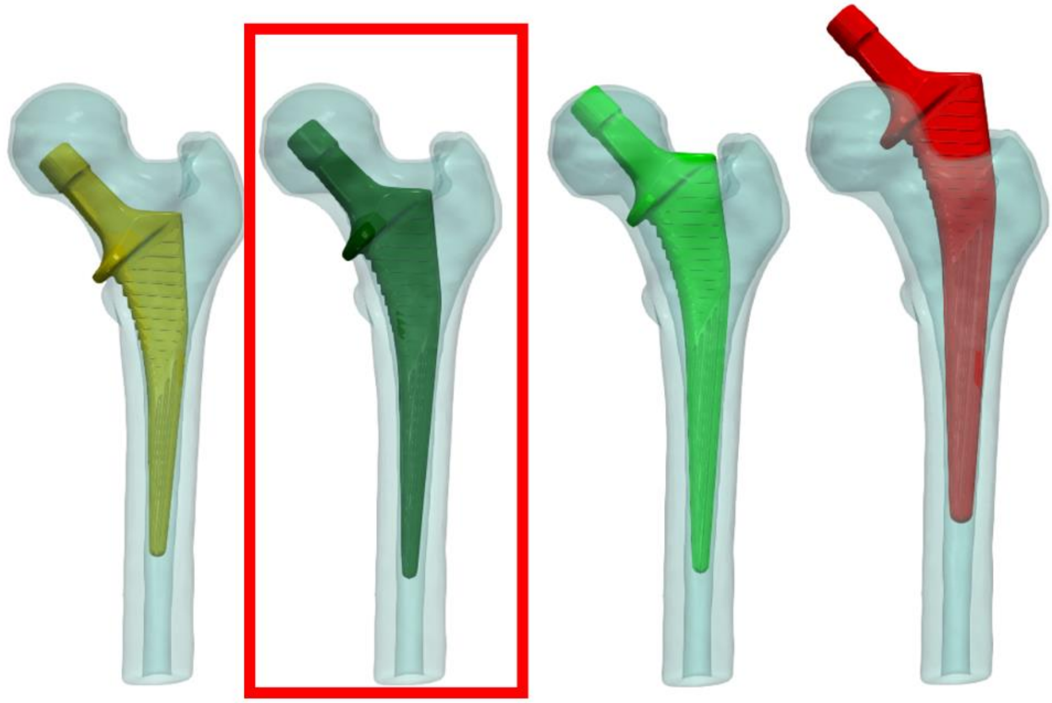

Figure 4-63: The best fitting femoral component is defined as the one that has the smallest distance from its head center to the femoral head center.

over 43 mm [78-80], while the standard stems are used for the majority of patients with the femoral offset less than 43 mm [78-80]. Fortunately, in the previous section, the femoral offset is measured. Therefore, in order to restore the femoral anatomy, a high offset may be a good choice if the patient has the femoral offset over 43 mm. Otherwise, a standard stem would be the best solution. In Figure 4-64 a standard and high offset stem can be seen.

4.3.6 The Choice of Femoral Component Neck Shaft Angle

Surgeons or Users of the stem fitting algorithm can determine whether a particular patient needs a different stem neck shaft angle other than a standard stem based on the patient's anatomy. Similar to femoral offset, hip prosthetic manufactures provide surgeons multiple options to choose the correct femoral component for a specific patient. Typical options include standard, high offset, collared, collarless, cemented, cementless, Coxa Vara, and Reef stems, etc. In Figure 4-65 multiple stem options for the Corail (DePuy-Synthes, A Johnson & Johnson Company, Warsaw, Indiana) stems can be seen.

Among those options, a Coxa Vara stem typically has a smaller neck shaft angle compared to a standard stem. In the previous section, the measurement of femoral neck shaft angle has been determined so the User can utilize the information stored in the database to determine whether a patient needs a Coxa Vara stem.

4.3.7 The Sizing Estimation of the Shell, Liner, and Femoral Head

A rule of thumb in clinical practice about determining the size of the shell stated as [81]:

$$\text{Size of the Shell} = \text{Femoral Head Diameter} + 8 \pm 2 \text{ (mm)}$$

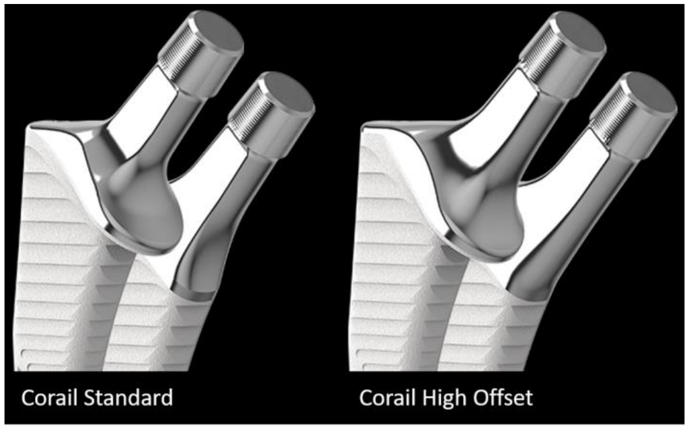

Figure 4-64: Standard and high offset Corail stem. Image from (www.depuysynthes.com).

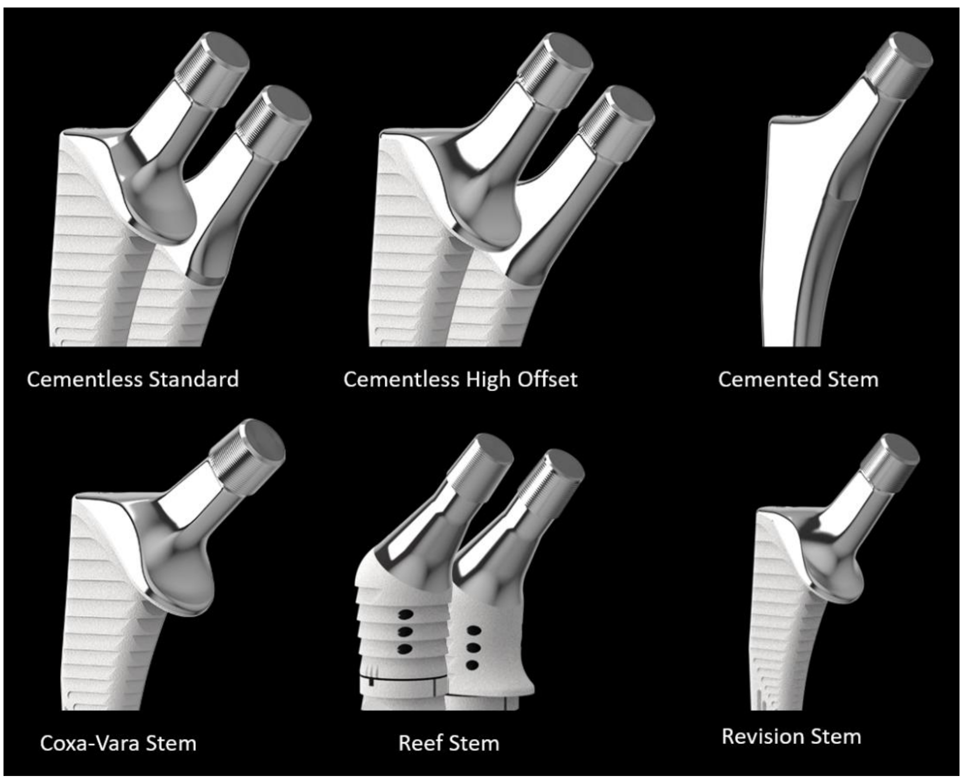

Figure 4-65: Diversity of the Corail stem system. Image from (www.depuysynthes.com).

This formula is applied to estimate the size of the shell. As the femoral head diameter is already measured in the previous section, it should be straightforward to estimate the size of the shell. The size of the liner is a dependence of the size of the shell, and the size of the femoral head component is a dependence of the size of the liner. Once the size of the shell is estimated, the sizes of the liner and femoral head are estimated as well. In clinical practice, the outer size of the liner is equal to the size of the shell, while the size of the femoral head component is equal to the size of inner aspect of the liner.

4.3.8 Femoral Component Fit Analysis

Once the femoral component is determined, it is necessary to see how well the femoral component fits the canal using our fitting analyses. In order to provide fruitful results, three intensive analyses have been developed. They are defined as (1) cross-sectional analysis, (2) slice analysis, and (3) contact map analysis.

Cross-sectional analysis functions similar to CT scans where the User can see the anatomy at each scan, but it is more powerful than CT scans in several ways. Cross-sectional analysis is a user graphic interaction program where users can freely view the anatomy at any orientation. To elaborate that point, while CT viewer program only allow users to view anatomy at three orthogonal views such as coronal, transverse, and sagittal view, the cross-sectional analysis allows Users of our process to handle, interact, and screen the anatomy at any arbitrary view. Cross-sectional anatomy of the femur and femoral component at different views using the cross-sectional analysis can be seen in Figure 4-66.

When using the cross-sectional analysis, it is quite simple to understand how the chosen femoral component fits the femoral canal. The User can screen the fitting by dragging the intersectional plane to the desired region to view the stem fit within the canal. If the plane is placed parallel to the coronal plane, the view turns into a traditional X-ray image (Figure 4-66). The cross-sectional analysis program not only functions similar to CT scans, but also it works in a similar manner to an X-ray image.

While the cross-sectional analysis provides a dynamic view of the anatomy, sometimes it is hard to remember which area is fit, and subsequently which is not. To overcome that shortcoming, a slice analysis enhances the visualization ability of the User by providing a static view of the fit between the chosen femoral component and the femoral canal. The slice analysis slices the femur bone and the chosen femoral component into small sections. They are then assembled to visualize the intersection at each slice. This approach allows a 3D view of the intersection of slices which can be seen in Figure 4-67.

Users now do not need to remember where the stem fits to the canal, instead users can see the fit in the 3D viewer. The advantage of this analysis is that Users can define a custom view, then the analysis will slice the femur and femoral component at that view.

The last point to be discussed pertaining to the slice analysis tool is that Users can define the thickness of the planes as it matches their needs. Therefore, the slice resolution will be enhanced, and Users will be able to visualize anatomy better. The power of VTK allows Users to zoom in and out and to have a better view without any restriction even when using a computer without the support of a graphics card.

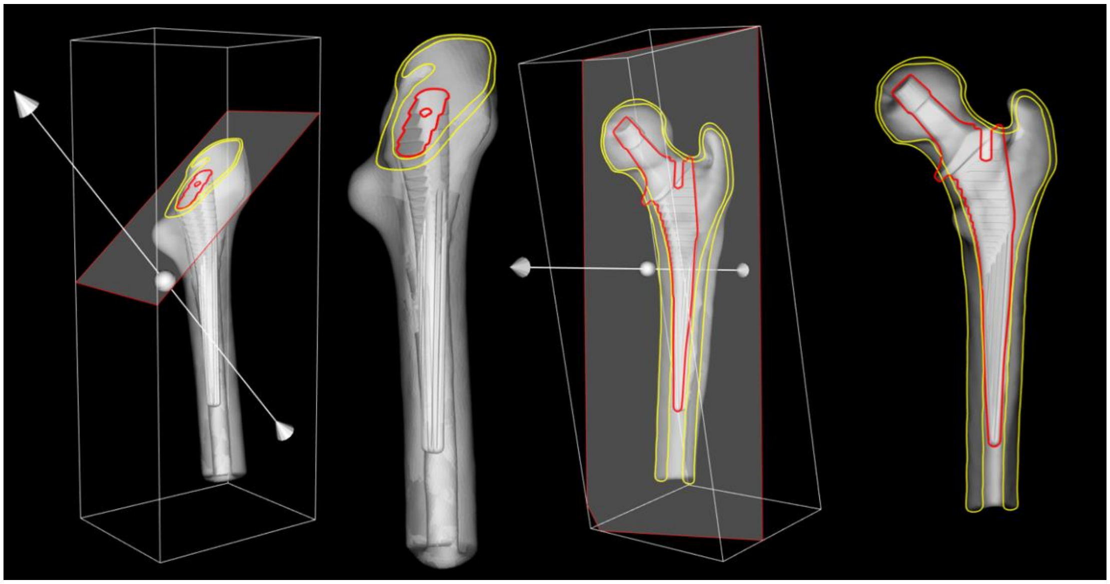

Figure 4-66: The cross-sectional analysis is used to screen the anatomy at arbitrary views.

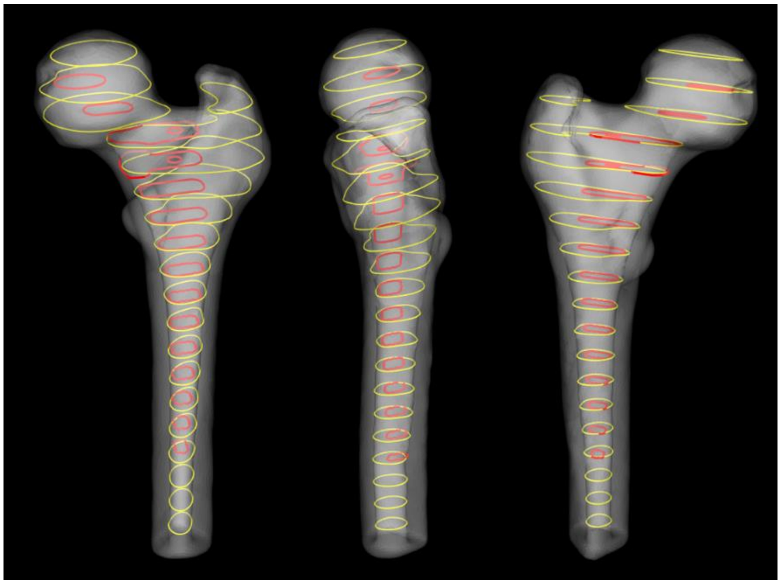

Figure 4-67: Slice analysis enhances visualization by proving a static view of the system.

The cross-sectional analysis and slice analysis modules are powerful qualitative tools that can be used to examine how the chosen femoral component fits the canal. They, however, do not provide information about the distance of the femoral component with respect to the bone. Hence, we developed the contact map analysis which overcomes the shortcomings of these other processes. The contact map analysis allows for measurements to be made to determine the distance from the outer aspect of the femoral component to the femoral canal. This distance is then determined at each slide and correlated to a visualization distance map where the closest distance to the canal is red and furthest distance as blue. The color map on the stem and color bar in Figure 4-68 show the distance from the stem to the canal or how much the stem would penetrate into the bone if that stem was chosen. The findings from this analysis allows the Users make a decision as to whether they would like to downsize or upsize the stem.

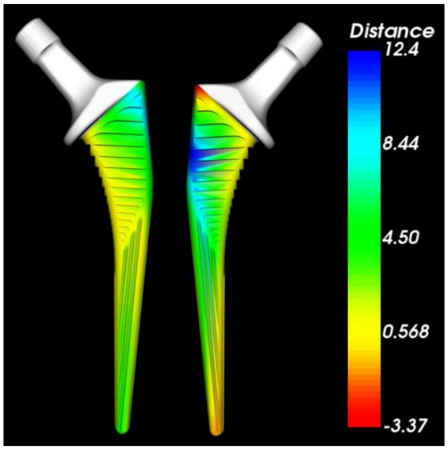

Figure 4-68: Contact map analysis allows users to see how close the femoral component to the canal.

4.4 VIRTUAL SURGERY

4.4.1 Choice of Surgical Approaches

The surgeon's choice of a surgical approach plays an important role in the implantation of a THA. Each surgeon has been trained or feels more comfortable using a specific surgical approach. Once a surgeon has been trained to use a specific surgical approach either in medical school or their fellowship, they often continue using that approach due to comfort level. This is also similar to the surgeon's choice of hip implant type and their commitment with hip implant manufactures.

This program provides three of the most popular surgical approaches (Figure 4-69). Some might say that most advanced surgical approach is direct anterior approach (Figure 4-70) because it is a minimally invasive surgical technique in which the surgical procedure is approached from the anterior of the hip. With this approach being the most recently introduced to the orthopaedic community, the surgeon exposes the hip joint by moving muscles aside along their natural tissue planes, without detaching any tendons. The direct anterior approach has been documented in the literature to be superior to other surgical approaches [82-85]. The publications document that this approach leads to much quicker recovery for the patient, with less pain, and more normal function after hip replacement [82-85]. Theoretically, the virtual surgery program allows for patient positioning during direct anterior approach and moving muscles aside to expose the hip joint (Figure 4-71).

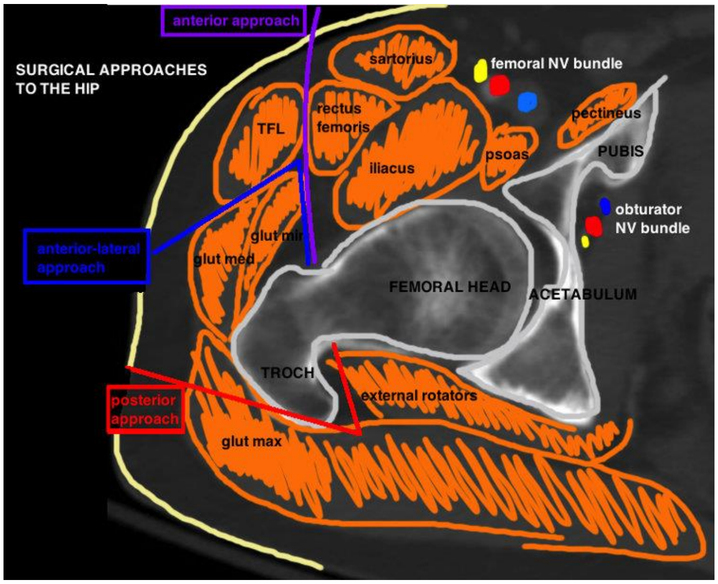

Figure 4-69: Three most popular surgical approaches of total hip replacement. Image from (hipandkneebook.com).

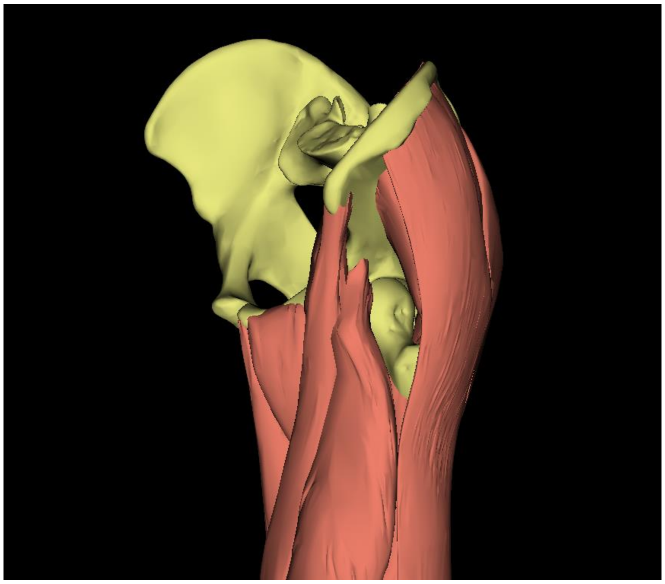

Figure 4-70: Theoretical direct anterior surgical approach.

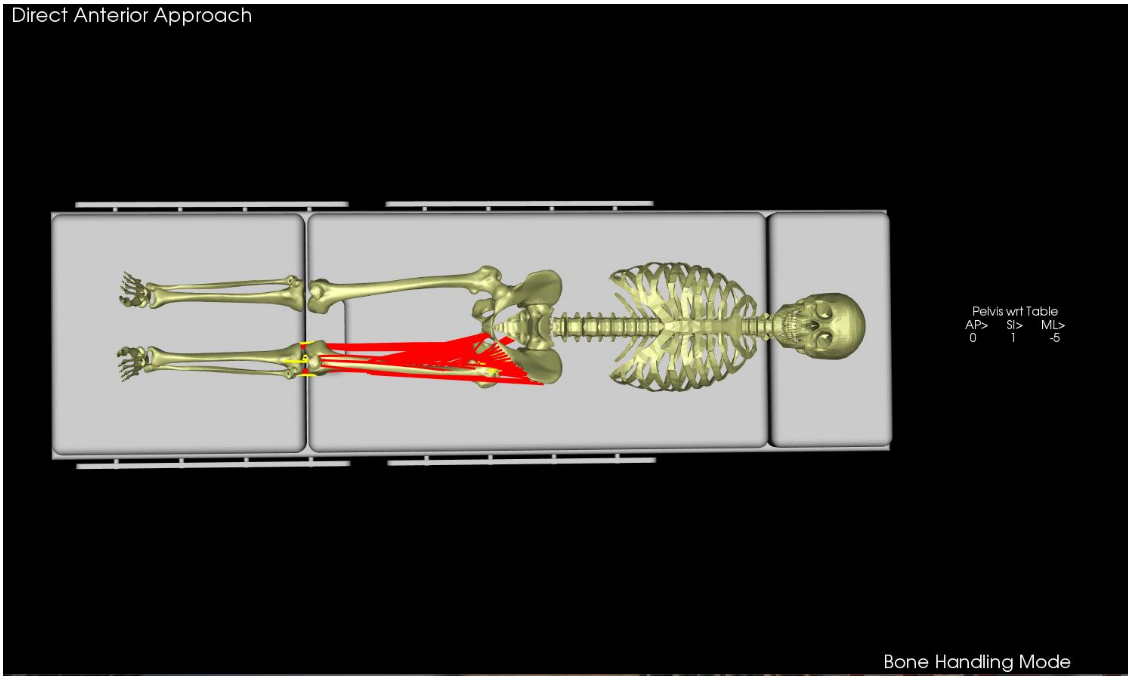

Figure 4-71: Patient positioning during direct anterior approach.

Traditionally, the posterior approach is the most common approach used to perform hip replacement (Figure 4-72). It is also has been a minimally invasive surgery where no muscles are cut to access the hip joint, but traditionally the surgeon's incision is greater than for the direct anterior approach because the surgeon has to cut through more tissue. Instead, muscles and ligaments are detached to expose the hip joint [86-89]. This virtual surgery program allows for patient positioning, detaching muscles and ligaments to expose the hip joint (Figure 4-73)

The program also has the capability to simulate the antero-lateral approach. This technique provides good exposure to the hip without trochanter osteotomy [83, 90-92]. The theoretical surgery for the antero-lateral approach is shown in Figure 4-74.

Similarly, for the direct anterior and posterior surgical approach, the virtual surgery provides options to position the theoretical patient on the surgical table properly (Figure 4-75). The flexibility of patient positioning enhances the effectiveness and accuracy of surgery. Along with the three most popular surgical approaches, additional approaches can be added to the virtual surgery module.

4.4.2 Modification of Muscles and Ligaments Property

Regardless of a chosen surgical approach, a certain amount of muscles and ligament are weakened after surgery. The virtual surgery program allows the user to retain, resect, weaken, and modify muscle and ligament properties according to the chosen surgical approach. In this simplified computer model of the hip joint, muscles and ligaments are represented as groups of individual fibers with different characteristics depending on the role of each muscle and ligament. In order to retain or resect a certain muscle or ligament

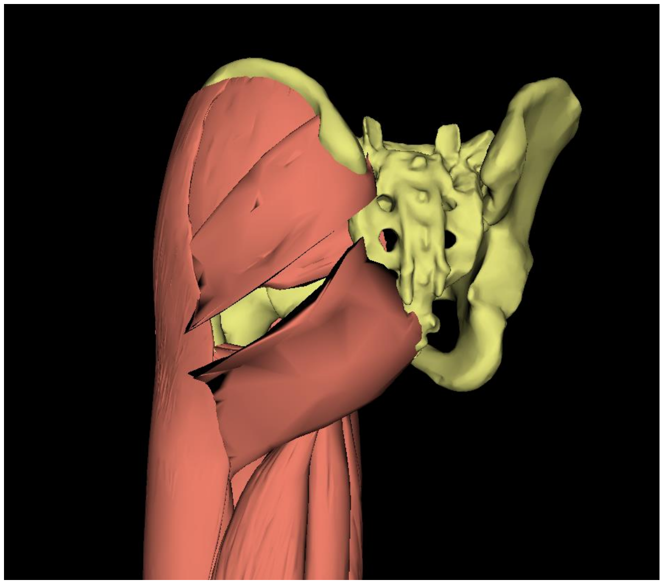

Figure 4-72: Theoretical posterior surgical approach.

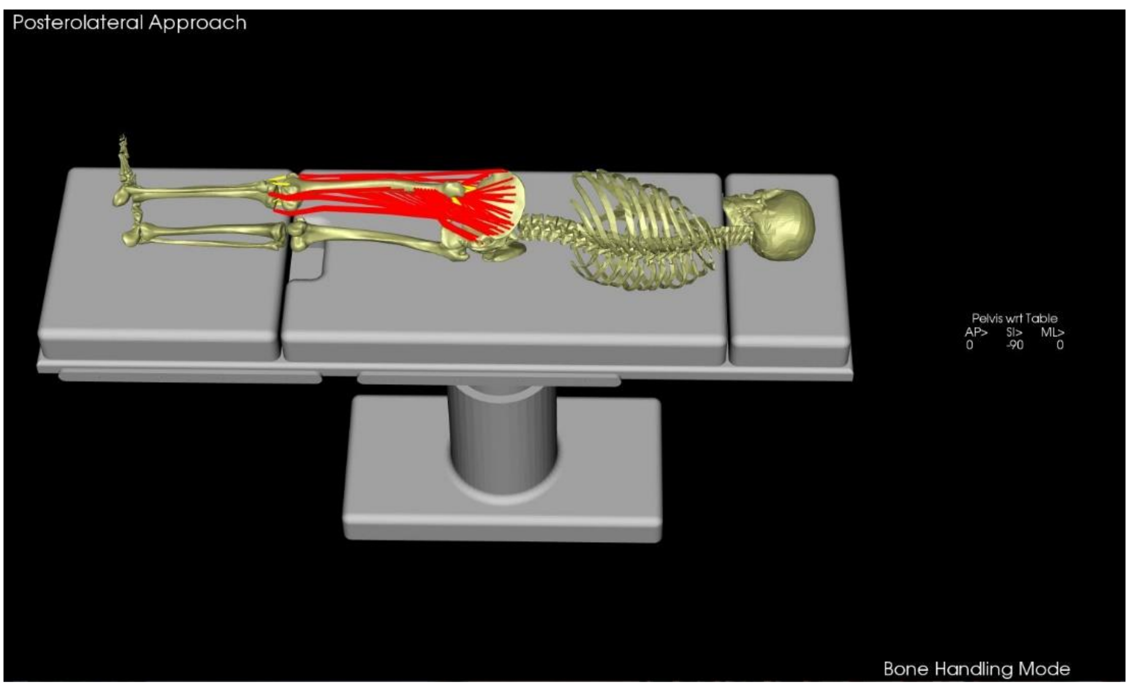

Figure 4-73: Patient positioning during posterior surgical approach.

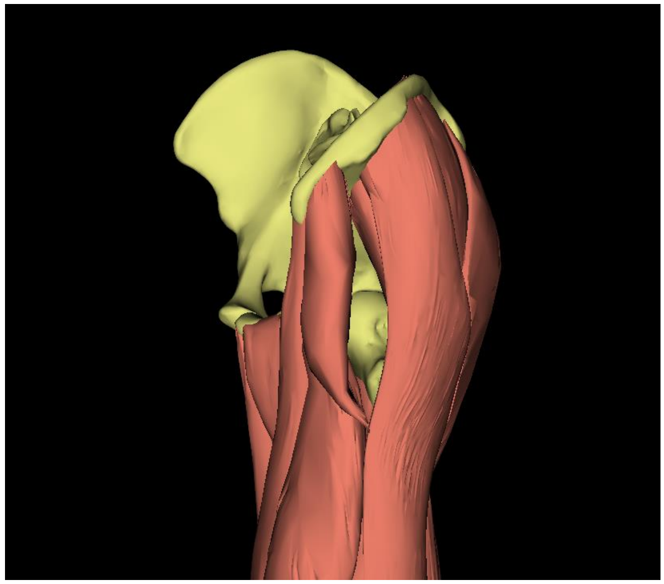

Figure 4-74: Theoretical antero-lateral surgical approach.

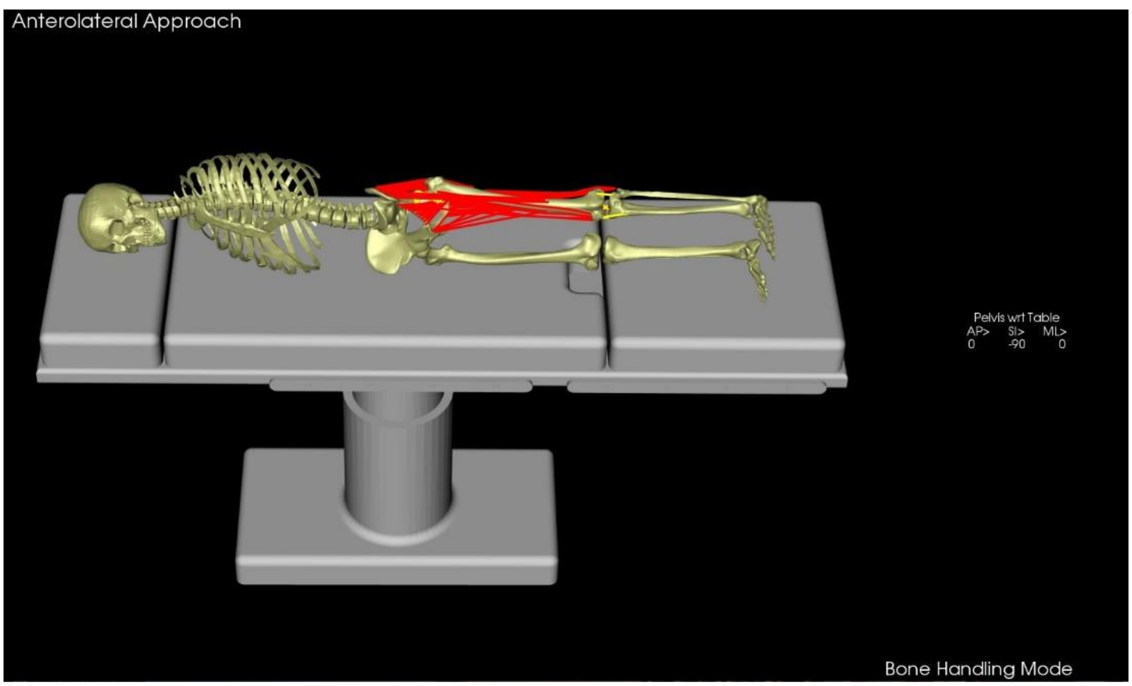

Figure 4-75: Patient positioning during antero-lateral surgical approach.

fiber, a graphic user interface (GUI) allows users to handle muscle and ligament properties. The GUI that allows users to retain and resect muscles and ligaments is shown in Figure 4-76.

4.4.3 Femoral Head Removal

Once the surgical approach has been chosen, the next step is to remove the femoral head. There are two options users can choose in their practice. The first option allows the user to manually place the neck cut. In the virtual surgery environment, a 3D CAD model of a saw is used to remove the femoral head. The user can also customize the neck cut based on their preference. Similar to a real surgery, the saw has to be moved to a proper position in order to completely remove the femoral head. As a result, a surgeon often makes multiple cuts into the femoral neck so that the head can be removed completely. The femoral head removal process after multiple properly positioned cuts is shown in Figure 4-77.

The second option available to the User is to remove the femoral head automatically. From the previous section, anatomical landmarks on the femur and pelvis have been defined. Based on the chosen femoral component and its intended placement, the femoral head can be removed without the Users with the theoretical saw.

4.4.4 Reaming Acetabulum

In order to ream the acetabulum, the femur is dislocated to expose the acetabulum. Once the User has chosen the set of bones, information is derived for the acetabulum and the proper reamer is selected, starting from the smallest size to a size through to the final size, representing the chosen acetabular shell. The program allows users to select different

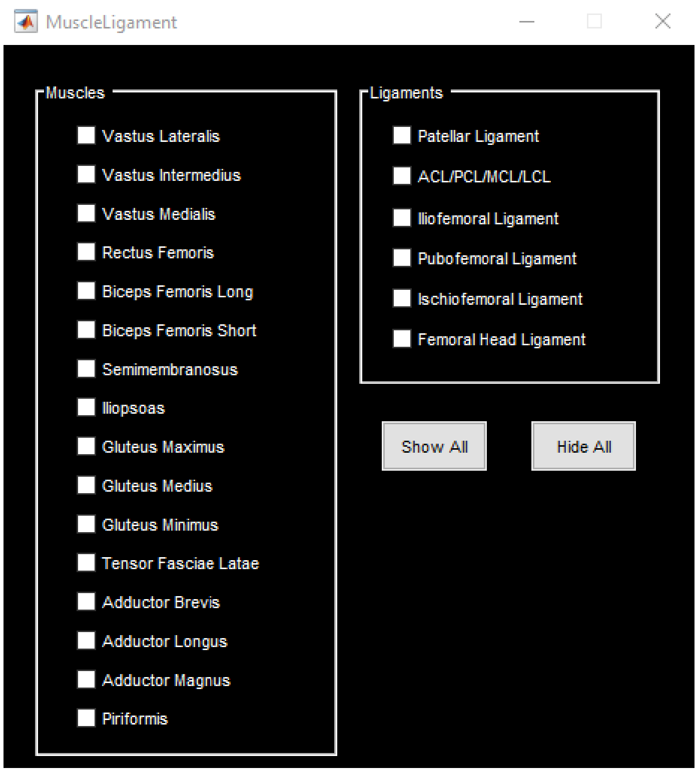

Figure 4-76: A computer graphic user interface is used to control muscle and ligament properties.

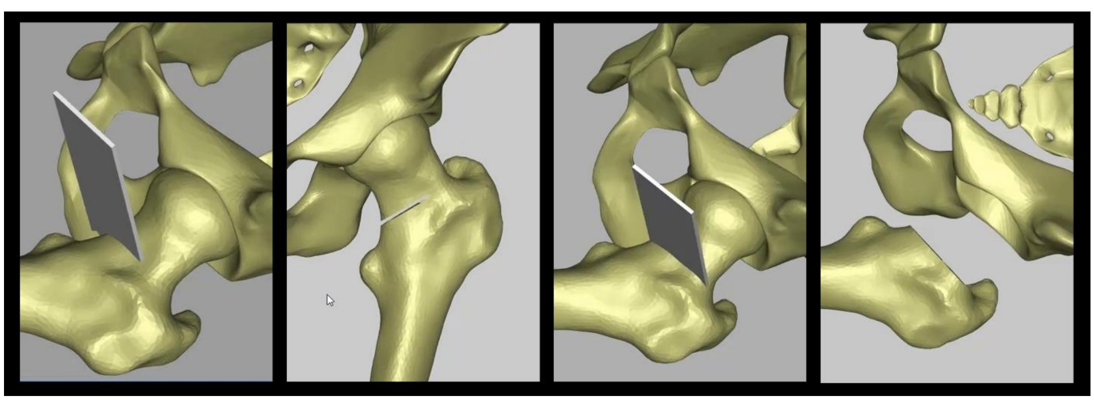

Figure 4-77: The femoral head removal process.

reamer sizes to reach the intended reaming depth. Four example sizes of reamers are shown in Figure 4-78.

The program allows Users to interactively handle the reamer to place it at a desired position. The User can translate and rotate the reamer. A relative position of the reamer with respect to the pelvis is displayed to guide the user to the reaming location. Once the reamer is placed at a desired position, all bones that are in contact with the reamer will be removed and replaced by the outer surface of the reamer (Figure 4-79). Similar to the femoral neck removal process, the User can choose either the manual process or automated process. The automated process is based on landmarks on the hip predicted in the previous section. The intended amount of reaming depends on the conditions of the hip joint and implants the surgeon intended to use. After the automated or manual process is selected, and the User can choose the "confirm" button and then the bone that is contact the with reamer will be removed, allowing for the acetabular cup placement.

4.4.5 Placing the Cup

The User can choose to place the cup either directly using the virtual surgery interface (Figure 4-80) or by using the advanced implant placement window (Figure 4-81). Similar to the advanced implant placement interface, the virtual surgery interface allows the User to interact with the acetabular cup. The User can translate and rotate the cup in order to place it at a desired position. A relative position of the acetabular cup with respect to the pelvis is calculated and displayed to guide the User throughout the cup positioning process.

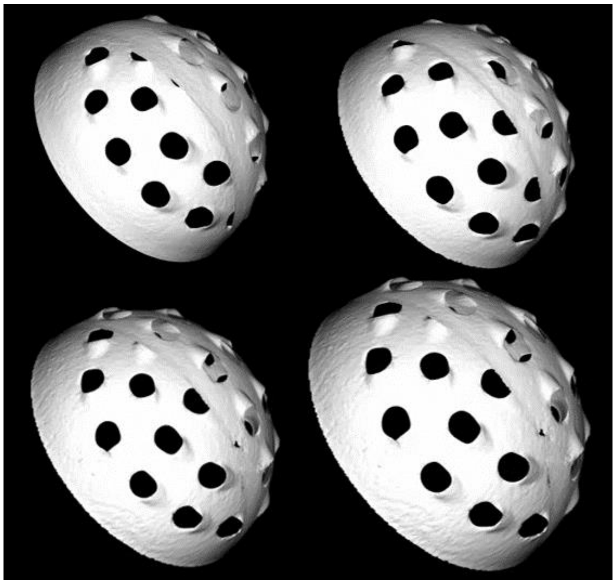

Figure 4-78: Reamer sizing options.

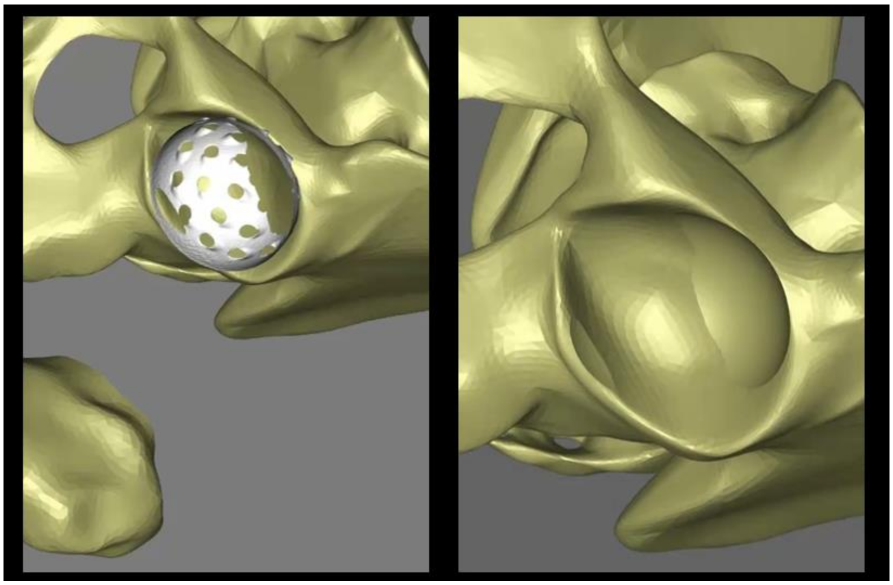

Figure 4-79: Reaming acetabulum process.

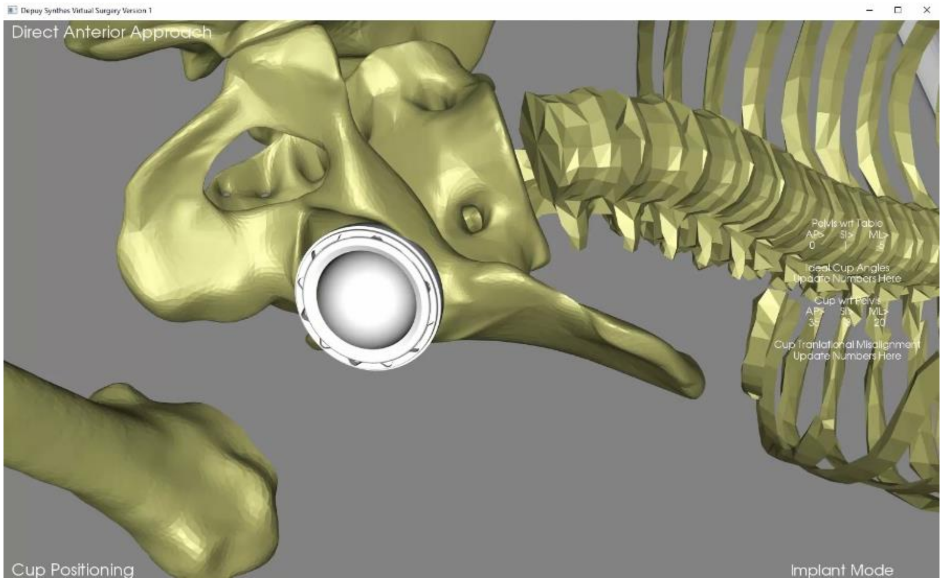

Figure 4-80: Cup positioning in the virtual surgery program.

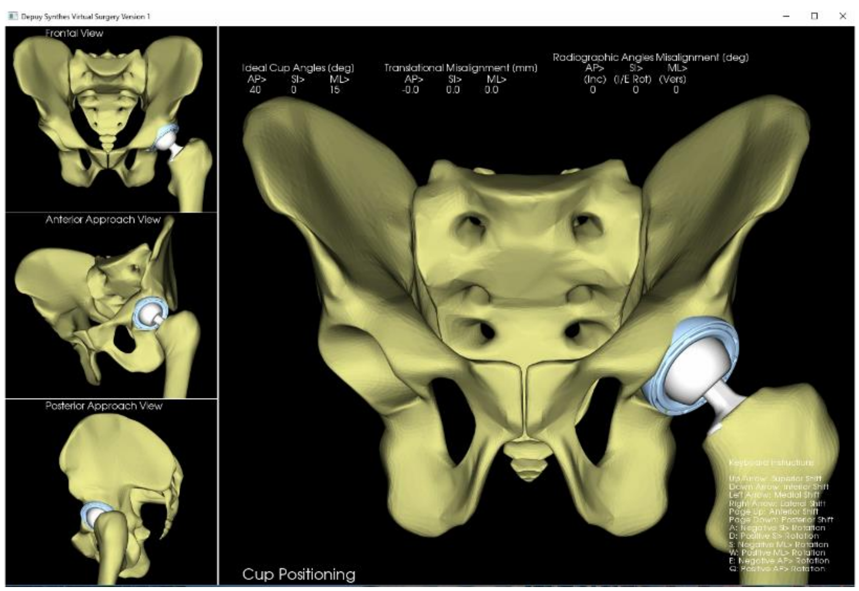

Figure 4-81: Advanced cup positioning interface.

4.4.6 Broaching Femoral Canal

Broaching the femoral canal to prepare for femoral component placement is carried out after the acetabular cup is placed. This theoretical approach is done using a Boolean operation of mesh models implemented in the VTK library [93]. The similarity of broaching and a difference operation in Boolean can be further explained. In the broaching process, a part of cancellous bone (or sometimes cortical bone) is removed. The shape of the cavity depends on the shape of the broach used for broaching. Mathematically, this process can be understood as a subtraction of the broach from the femoral canal. This approach shares a similar methodology to the difference operation in Boolean. Given two sets of data, A and B, the difference between A and B is defined as the elements that belong to A, but not B. The same concept is applied to subtract the broach from the femoral canal to create the femoral cavity. The union, intersection, and difference operation performed by the Boolean operation of two meshes are represented in Figure 4-82. The difference operation is applied to the broach and femur to create a hole for femoral component placement as shown in Figure 4-83.

4.4.7 Placing Femoral Component

Once the femoral canal cavity is prepared, the virtual surgery program guides the User to place the femoral component at a proper position. There are constraints that restrict the femoral component from being placed at an arbitrary position. As one might expect, the femoral component cannot be placed deeper than the depth of the hold created by the broach. Another restriction is if a bigger femoral component is used, the User has to choose an appropriate broach. If not, the femoral component cannot fit in the canal cavity properly,

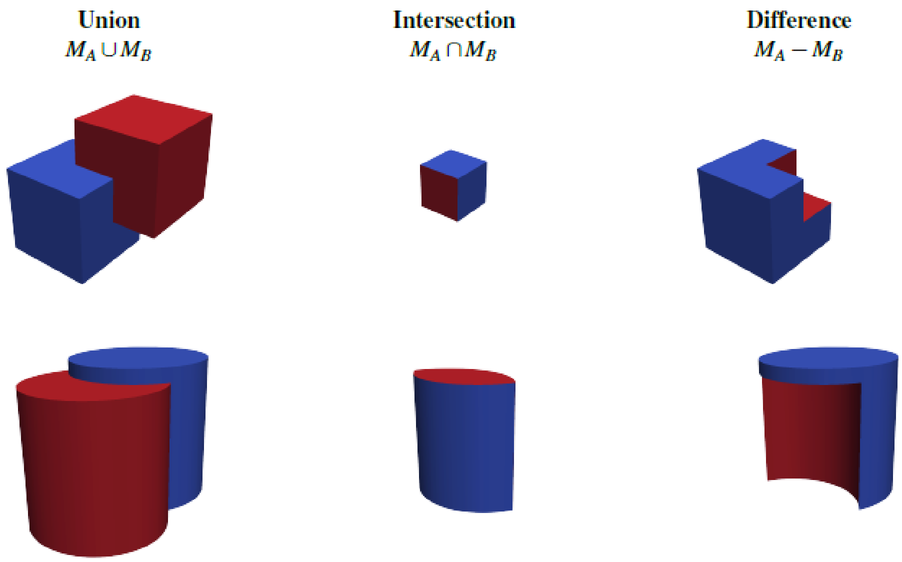

Figure 4-82: Boolean operations between two mesh models. Image from [93].

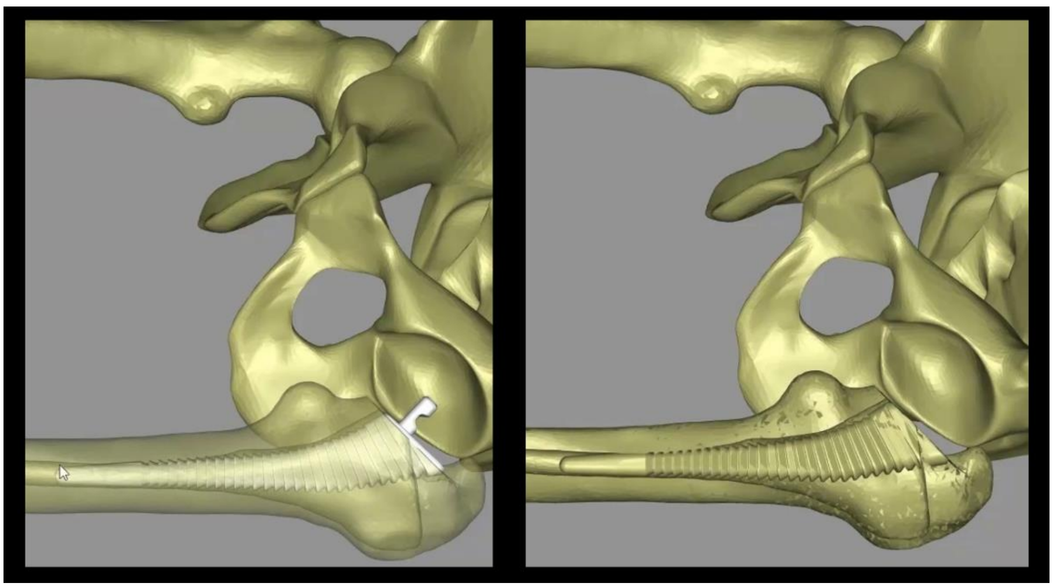

Figure 4-83: Theoretical broaching is performed though the difference operation of VTK Boolean.

resulting in hanging of the femoral component in the canal, which leads to increased leg length or instability of the femoral component fixation. The femoral component is placed at the position created by the broach is shown in Figure 4-84.

The user can either choose to place the femoral component using the virtual surgery program itself or use the advanced implant positioning tool (Figure 4-84). That tool is identical to the one used for the acetabular cup, but now it is used for the femoral component.

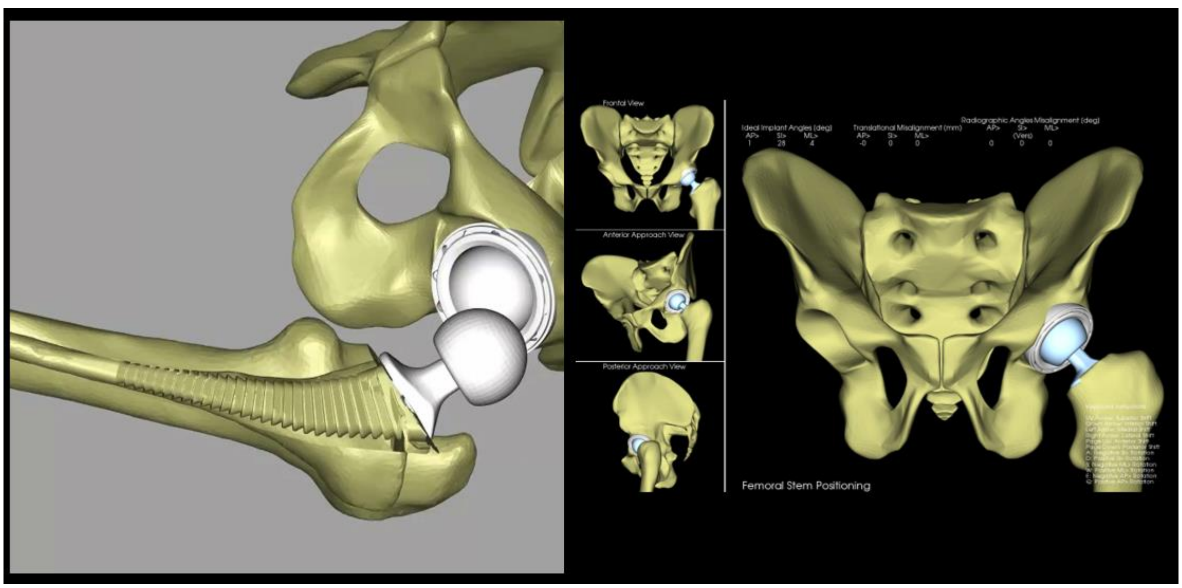

Figure 4-84: Femoral component placement using the virtual surgery program (left) and the advanced implant component positioning (right).

4.5 MATHEMATICAL MODELING ANALYSIS

In a clinical practice, it is common practice to follow up with their patients to evaluate how the implant is functioning after the surgery. The follow up should last years, throughout the lifetime of the implant. Therefore, this long-term follow up process provides a meaningful evaluation of the hip implant over a specified period of time, but minimal intra-operatively information is document and does not allow the surgeon to receive instant feedback. Fortunately, forward solution mathematical modeling of the hip joint has been developed at the Center for Musculoskeletal Research, University of Tennessee. The model functions as a theoretical joint simulator, providing instant feedback to surgeons and designers alike. This model, which has been validated, has successfully predicted separation, instability, edge loading, and other complications of total hip arthroplasty. The details about this modeling were demonstrated and explained in-depth initially by Dr. Michael LaCour in his dissertation [61]. In this section, the mathematical model will be briefly re-introduced as a follow-up to Dr. LaCour's work, rather than going through a detailed step by step to construct the entire model. In addition, a sustainable effort has been made to improve the model's performance, enhance and expand its capabilities, and provide a powerful tool for orthopedic research. Detailed modifications, improvements, and the general introduction of the original model are described in this section. It is important to note that after virtual surgery process is completed, where the hip implant components are theoretically implanted in the optimal positions, these positions can then be used in the mathematical model.

4.5.1 Description of The Original Model

The original mathematical model contains two separate simulations that represent stance and swing phase of gait. Each model features six bodies as shown in Figure 4-85: the foot (b), tibia (e), patella (c), femur (f), pelvis (a), and upper body represented by the torso (d). For both stance and swing phase models, the femoral implant component and acetabular cup are included but represented as massless bodies, commonly referred to as frames. The ankle and patellofemoral joint are modeled as spherical joints that allow for three degrees of freedom. There is one point of contact for each of these joints. At the knee, the femur and tibia are assumed to always contact at two points in the medial and lateral articulating surfaces. The hip is modeled as a ball and socket joint with multiple contact points.

In the stance phase model, known ground reaction forces are assumed to apply at the foot center and thus are imputed to the model at this point. With respect to the swing phase model, the force of the contralateral leg is specified. In both models, the ligaments are modeled as linear and/or non-linear springs [61, 94]. As the stance and swing phase simulations are fully regarded as forward solution models in nature, all muscles acting at the hip are controlled by proportional-integral-derivative controllers (PID controllers). There are three PID controllers that can be used to drive the model for the forward and inverse solution simulations. One PID controls the hip flexion/extension muscle group, one PID controls the hip abduction/adduction muscle group, and one PID controls the hip internal/external rotation muscle group. In order to allow for the translation of the femoral head within the acetabular cup, the translation of the hip joint is controlled by a contact detection algorithm. This contact detection algorithm takes surfaces of the femoral stem

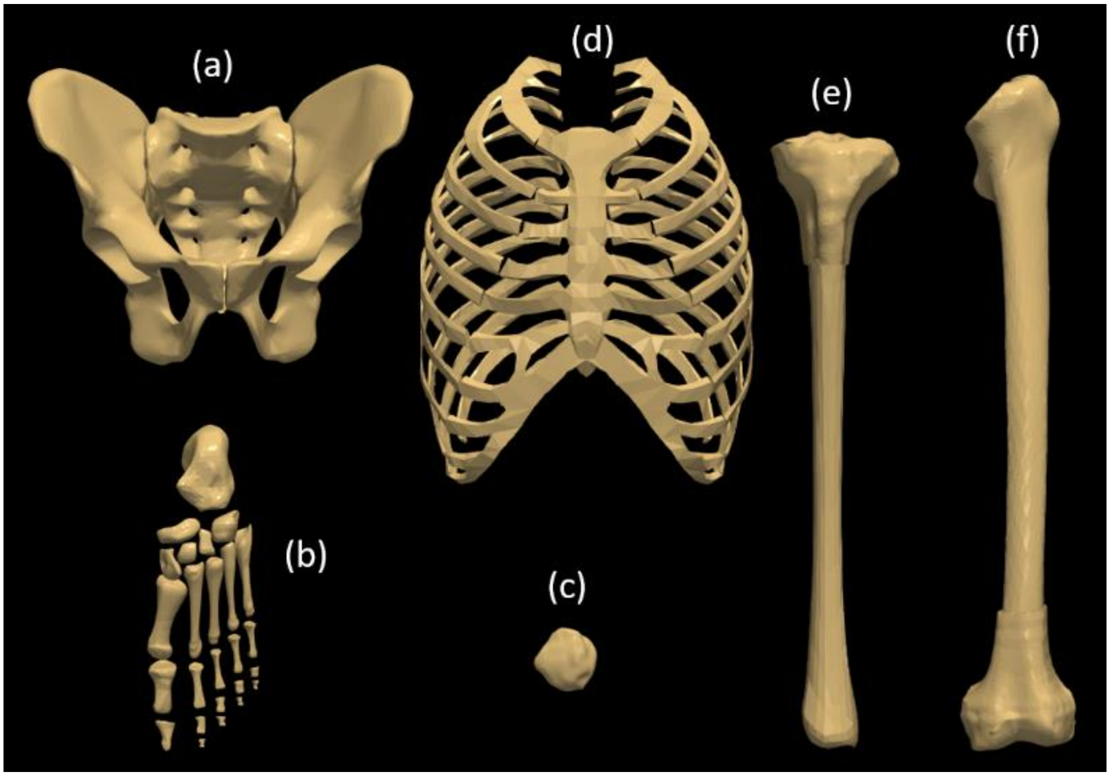

Figure 4-85: Six bones are used in the original hip model: (a) pelvis, (b) foot, (c) patella, (d) torso, (e) tibia, (f) femur.

head and inner surface of the acetabular as input data and calculates the interaction forces between the two bodies. This algorithm allows the femoral head to slide within the acetabular cup, resulting in a relative motion between two surfaces. When the distance between the two surfaces is greater than 1 mm, it is assumed that the hip separation occurs. For complete details and assumptions to model the hip, please see Dr. Lacour's dissertation [61].

4.5.2 Correction of The Hip Torques

Autolev (Motion Genesis^{TM}) is a symbolic programming language for solving multi-body dynamic problems [95-97]. The coding use for Autolev, albeit a high-level language, still exhibits multiple shortcomings that restrict users from coding and debugging efficiently. One such example is that muscles and ligaments in the human body are non-linear systems that need complex equations to represent their functionalities. Muscles and ligaments can be represented in Autolev, but only in a simplified manner. In order to have a better representation of muscles and ligaments, the dynamic system is exported into C, Matlab, or Fortran [60]. The muscle and ligament equations are modeled separately are then added to the executable file. For that reason, the complexity of the system is increased, and the system becomes challenging to handle. Another issue is that Autolev does not support contact force modeling between two rigid bodies, such as the femoral stem and the acetabular. In order to calculate the interaction force between these bodies, a contact detection algorithm is implemented in C or Matlab, and then added to the executable file. A limitation of C programming language is that it does not support object-oriented programming, therefore, the complexity of the program increases along with the number of contact surfaces. As a result, Users need to have a very strong C programming foundation in order to manage and handle the program to work as expected. Unfortunately, in the existing model, the hip torque equations have not been well formulated, resulting in an error. Below are the equations that calculate the torques acting on the femoral stem and the acetabular in the existing program.

$$\text{TORQUE\_FC} > = \sum_{I=1}^{n} r_i^{AC} \times F_i$$

$$\text{TORQUE\_AC} > = \sum_{I=1}^{n} r_i^{AC} \times (-F_i)$$

In these equations, TORQUE_FC> is the torque acting on the femoral stem, and TORQUE_AC> is the torque acting on the acetabular cup. The section r_i^{AC} is the moment arm of the force F_i that are calulated in the acetabular reference frame. The first equation calculates the torque acting on the femoral stem by using the moment arm in the acetabular reference frame. This error results in an incorrect torque acting on the femoral stem, leading to an incorrect calculation of other torques and interaction forces at other joints. In order to fix this problem, the following correct equations are written and properly implemented in the code:

$$\text{TORQUE\_FC} > = \sum_{I=1}^{n} r_i^{FC} \times F_i$$

$$\text{TORQUE\_AC} > = \sum_{I=1}^{n} r_i^{AC} \times (-F_i)$$

An experiment has been performed to illustrate the differences between the incorrect and corrected equations influence the results. In this experiment, the femoral stem and the acetabular cup are placed at their ideal position. The torques acting on the knee are shown in Figure 4-86. The red and dashed-green curves in Figure 4-86 represent the results of the existing and improved program, respectively. As the moment arm is changed, the torques acting on the knee is shown to change accordingly. As shown in Figure 4-87, the quadricep muscle and knee interaction forces are affected by the changes of moment arms as well.

4.5.3 Investigation of Artifact Spikes at The Beginning of Simulation

The existing program utilized three proportional-integral-derivative (PID) controllers to drive motions of the hip. These controllers drive muscle forces so that hip motions will approach the realistic hip motions. At the initialization of each simulation, many parameters need to be initiated and they take time to be stabilized. For that reason, a large number of artifact spikes occur during this period, which makes the model less accurate. Red rectangles in Figure 4-88 and Figure 4-89 represent these spikes in the existing simulation program. As shown in Figure 4-88 and Figure 4-89, these spikes take approximately 0.05 second to be stabilized.

In order to solve this problem, an adjustment to the simulation has been developed and implemented. Instead of simulating the model from 0 to 0.6 second as listed in the original model, the simulation was set to run from -0.1 to 0.6 second. The period from -0.1 to 0 is where artifact spikes occur, and the period from 0 to 0.6 is where the program works with stability. By eliminating the period from -0.1 to 0, a smooth simulation of the hip

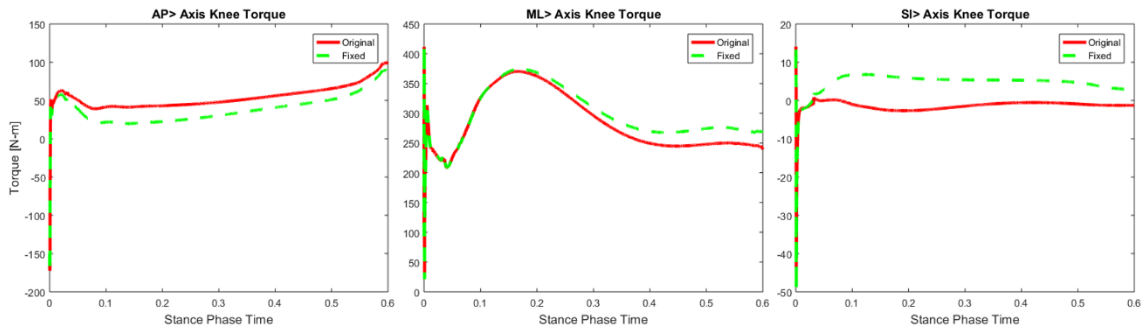

Figure 4-86: Comparison of the torques acting at the knee between the original (red) and fixed model (dash - green).

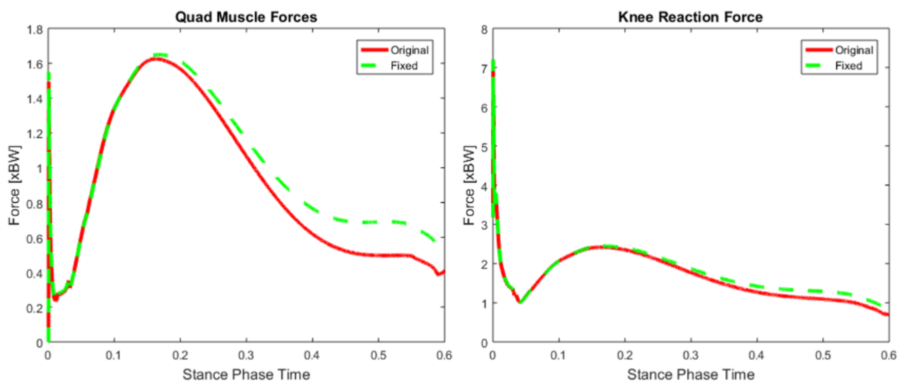

Figure 4-87: Comparison of the quadricep muscle forces and knee interaction forces between the original (red) and fixed model (dash - green).

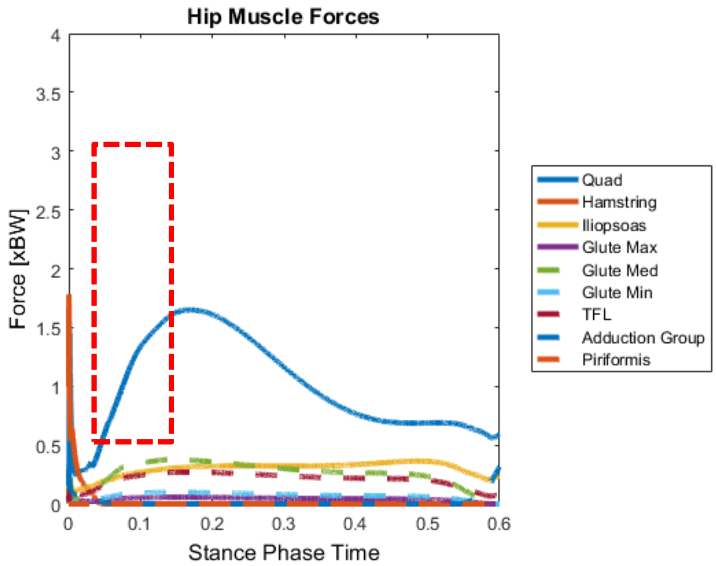

Figure 4-88: Occurrence of artifact spikes in the initialization of hip muscle forces.

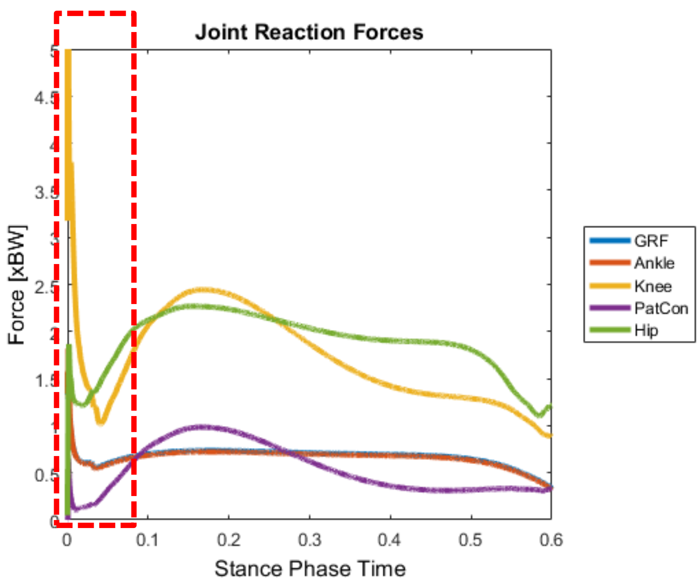

Figure 4-89: Occurrence of artifact spikes in the initialization of joint reaction forces.

model can be obtained. In Figure 4-90 and Figure 4-91 a side-by-side comparison of those spikes before and after they have been stabilized can be seen.

The improved program is usable if the hip motions of the existing program and the improved program are approximately the same. An experiment was conducted in which hip motions of the two programs were analyzed and compared. Figure 4-92, Figure 4-93, and Figure 4-94 demonstrate that the hip motions in the existing program are equivalent to the improved program, and therefore the improved program can be used to replace the existing program for future simulations.

One drawback with respect to this approach is that the PID controllers need to be redefined if the position of the implant component is changed. This restricts the capability of simulating different surgical planning settings where the user may desire to simulate different positions of the implant. This is also an issue in the existing program. The only thing that is different between the improved and existing program is that in the existing program, the spikes are influencing whether or not the PID controllers are tuned. Without a close examination of the simulation results, one may think that with the same PID controllers' parameters, the program can simulate any surgical planning settings. However, it is apparent that the PID controllers need to be tuned each time the program is used in order to simulate different surgical settings. Tuning PID parameters is a challenging task, even for skilled researchers. For this reason, there is still a need to have an automated tuning program that can be used to change the PID controllers' parameters, leading to a simulation that meets expectations. This automated tuning program is introduced in the following section.

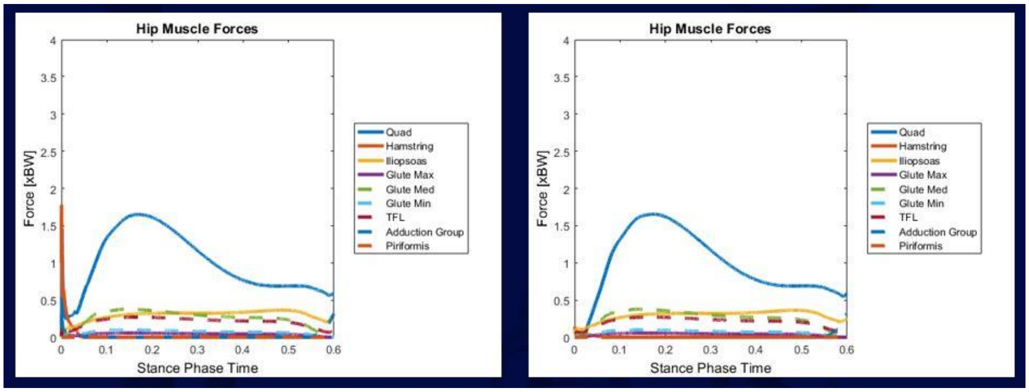

Figure 4-90: Artificial spikes (left) and stabilized spikes (right) in hip muscle forces.

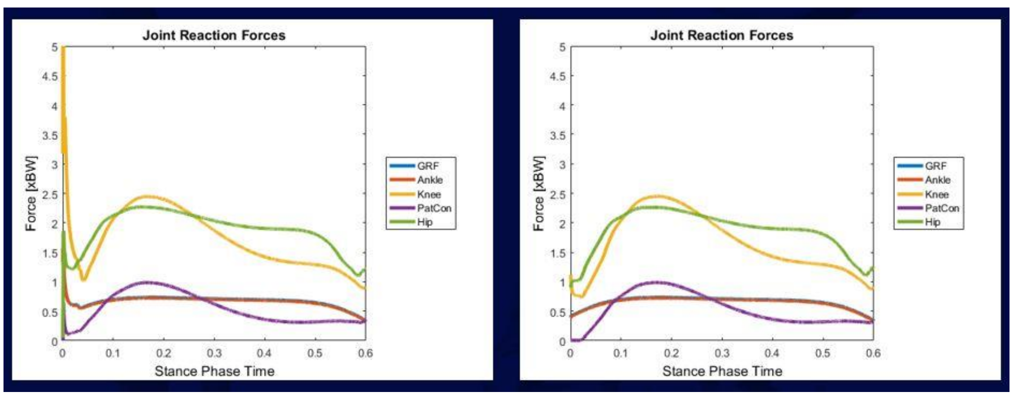

Figure 4-91: Artificial spikes (left) and stabilized spikes (right) in joint reaction forces.

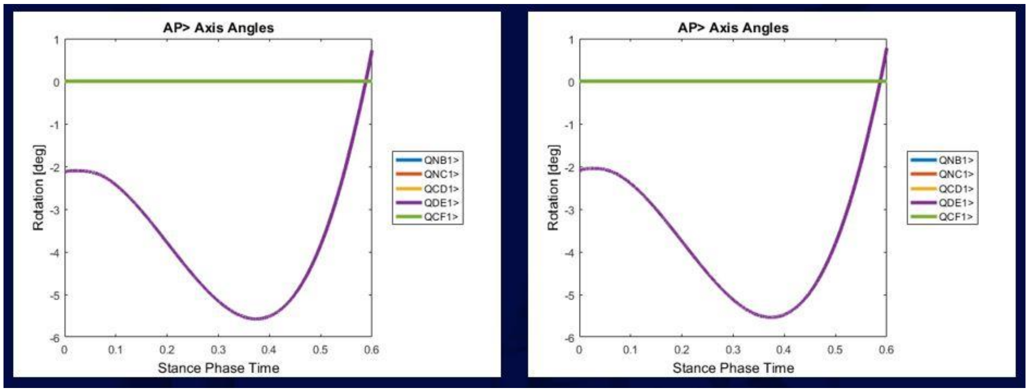

Figure 4-92: AP motions of the hip before (left) and after stabilized spikes (right).

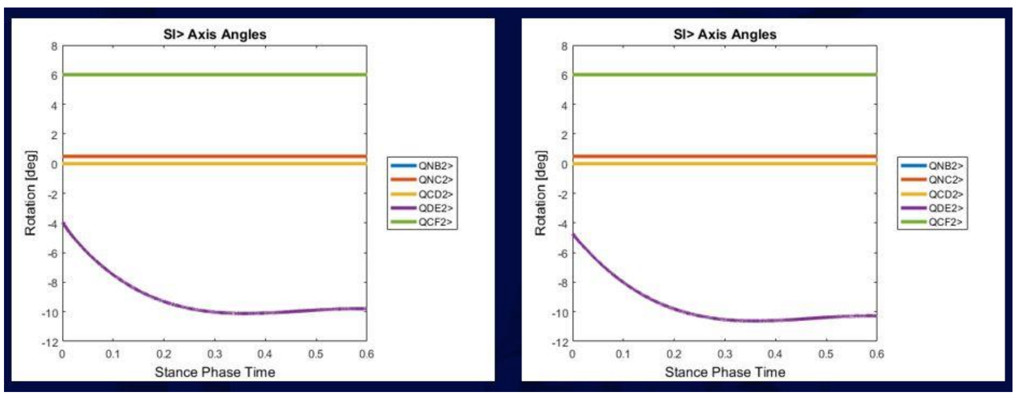

Figure 4-93: SI motions of the hip before (left) and after stabilized spikes (right).

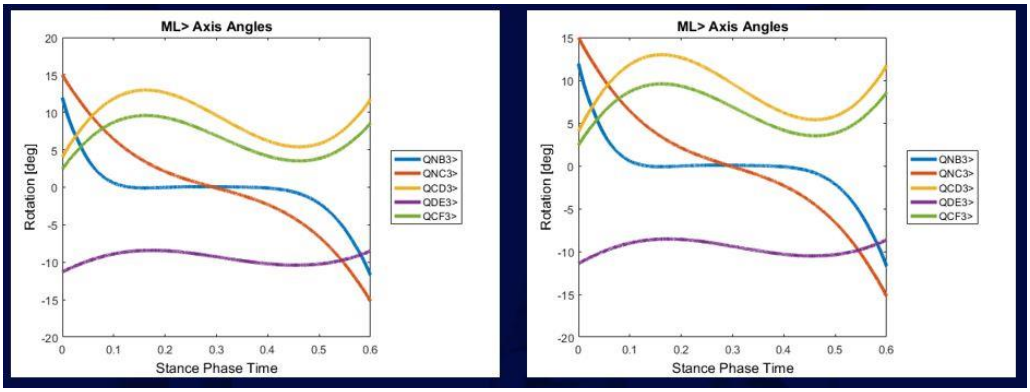

Figure 4-94: ML motions of the hip (left) and after stabilized spikes (right).

4.5.4 Automated Tuning PID Controllers

As previously discussed, the tuning process is a time-consuming and can present challenging concerns. Therefore, an automated PID tuning algorithm has been developed (Figure 4-95). The algorithm uses an optimization procedure, which uses the pattern search algorithm to automatically tune the gains for PID controllers. The cost function is the mean difference between the computed motions and the desired motions. The idea is to make the computed motions to best fit the desired motions. Therefore, the optimization program optimizes PID gains such that the differences between the computed motions and desired motions are as small as possible. The algorithm is implemented in Matlab and has successfully tuned gains to meet the requirements. A side-by-side comparison of motions as the input parameters and optimized parameters are shown in Figure 4-96.

The automated PID tuning algorithm provides many additional benefits to the mathematical model which still implements Kane dynamics within Autolev. One such benefit is the ability to save time and reduce effort to run the simulation. This is especially important for patient-specific simulations, where each simulation has different initial input parameters that require PID gains to be tuned. The algorithm offers ease of use, more efficient simulation preparation, and a simplified learning curve for new users.

4.5.5 Stability Analysis of the Mathematical Model

In an attempt to investigate the causes of the instability at the beginning of each simulation, there are several hypotheses that have been implemented. The first hypothesis is that muscle excitation, muscle forces, and initial parameters of the model are not properly initialized. Human movement is a continuous and remains a very complicated process. The

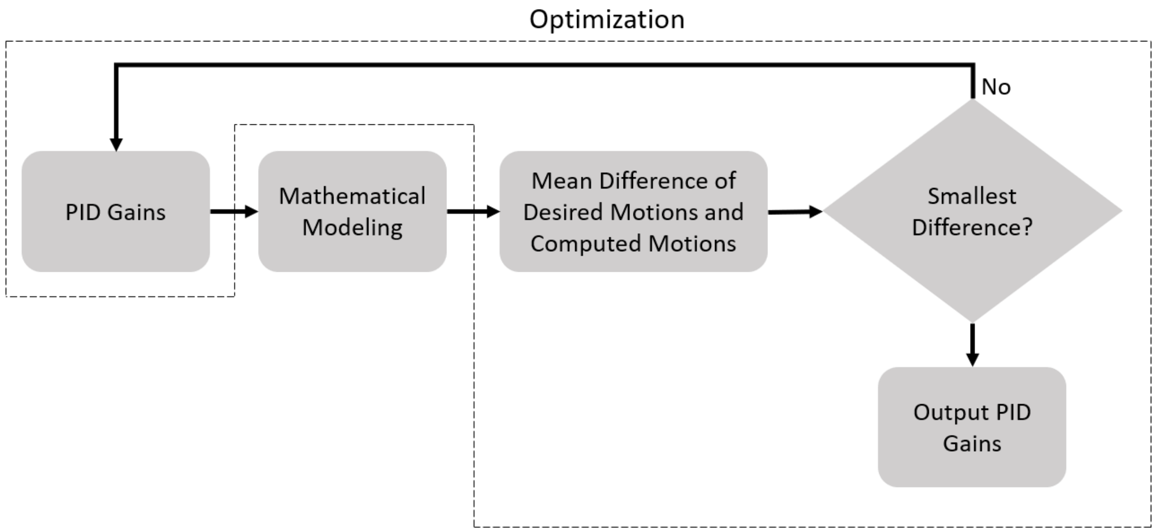

Figure 4-95: The automated turning algorithm framework.

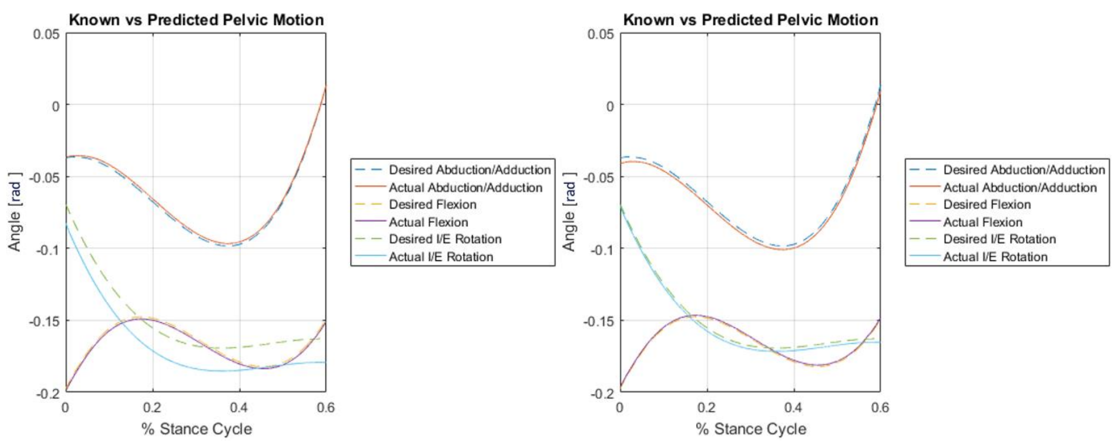

Figure 4-96: Initial input motions (left) and output motions from the automated tuning algorithm (right).

transition from stance to swing phase and vice versa is always accompanied by changes in muscle excitation. This hypothesis makes sense in the existing program because there are a lot of parameters that are not initialized at the beginning of a simulation. The second hypothesis is based on the PID controllers. The PID controller has been widely used in the control system and has been proven to be ease of use as well as reliable. However, there are limited studies that investigate how sensitive it would be in a biomechanical application. The last hypothesis concerns the performance of the contact detection algorithm, where the contact forces between two rigid bodies are measured. The contact detection algorithm used in the existing program is based on the elastic foundation with a lot of assumptions pertaining to the spring and damper coefficients. The choice of these coefficients, similar to the choice of the PID controllers' gains, is challenging and potentially produces instability in the mathematical model. In order to investigate the causes of instability, each hypothesis is isolated and analyzed.

4.5.6 Sensitivity Analysis of PID Controllers

In this section, the PID controllers are investigated. Three experiments have been performed to determine how each PID controller affects the stability of the mathematical model. In the first experiment, there is only one PID controller in the system that is used to control the flexion and extension motion of the pelvis. In Figure 4-97 a demonstration of the performance pertaining to the flexion/extension PID controller is shown. The computed hip muscle forces and the interaction forces at the knee and hip are shown in Figure 4-98.

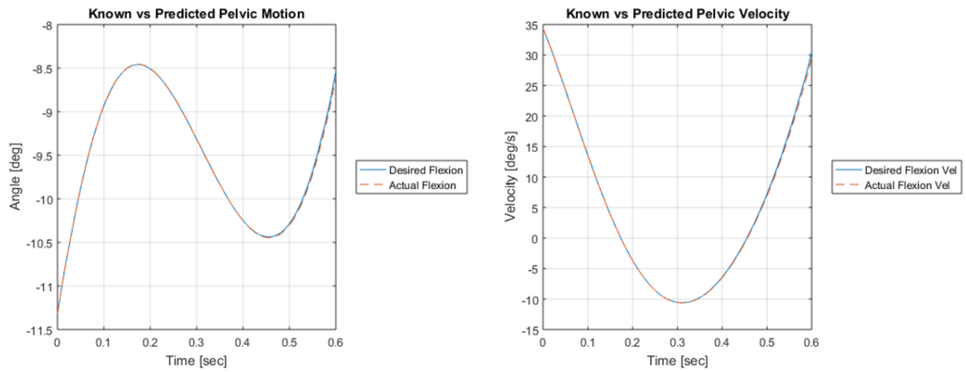

Figure 4-97: The performance of the PID controller that controls the flexion/extension motion of the pelvis.

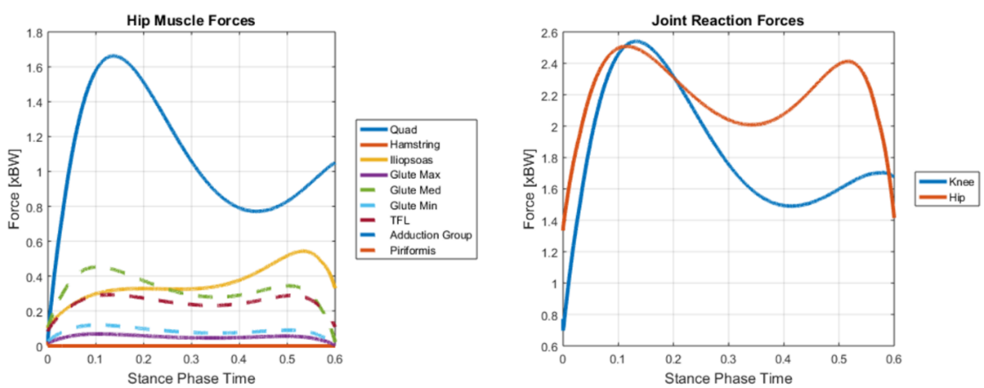

Figure 4-98: The hip muscle forces (left) and interaction forces at the knee and hip using one PID controller in the pelvis's flexion and extension.

As shown in Figure 4-98 there is no instability in the system, it can be concluded that the PID controller pertaining to the pelvis flexion/extension does not influence instability.

In the second experiment, one more PID controller is added to the system. Along with the previous PID controller, the new PID controller controls the pelvis's abduction/adduction. The performance of the two PID controllers is shown in Figure 4-99. In Figure 4-100, a demonstration of the hip muscle forces and interaction forces at the knee and hip are shown. Similar to the single PID controller experiment, adding the abduction/adduction PID controller does not yield instability.

In the third experiment, an internal/external rotation PID controller is added to the previous model, resulting in the use of three PID controllers in the system. The performance of three PID controllers are shown in Figure 4-101. In Figure 4-102, a demonstration the hip muscle forces and interaction forces at the knee and hip are shown.

The three PID controllers seem to not affect the instability of the system as shown in Figure 4-101 and Figure 4-102. Therefore, a conclusion can be drawn from these evaluations that the PID controllers reveal a satisfactory performance and do not contribute to instability of the mathematical model.

4.5.7 Sensitivity Analysis of the Contact Detection Algorithm and Initial Parameters

As it has already been proven that the PID controllers do not cause any instability in the mathematical model, they are kept in the system while analyzing the effect of the contact detection algorithm. When adding the contact detection algorithm to the system, there are a set of parameters that need to be initialized. Therefore, it is necessary to analyze

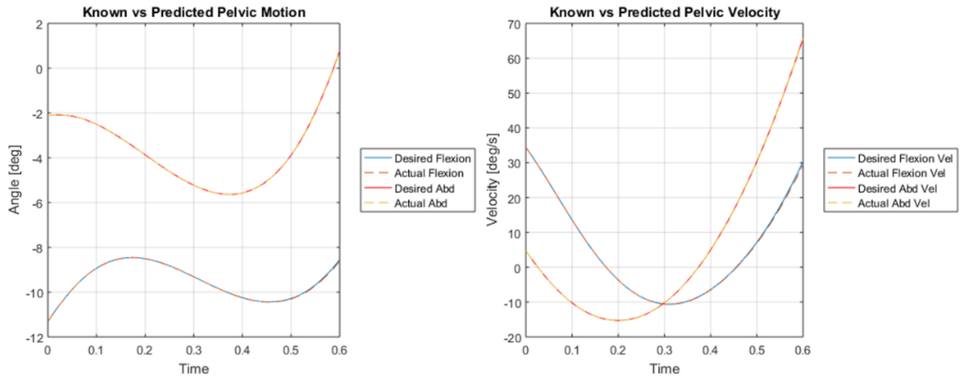

Figure 4-99: The performance of two PID controllers.

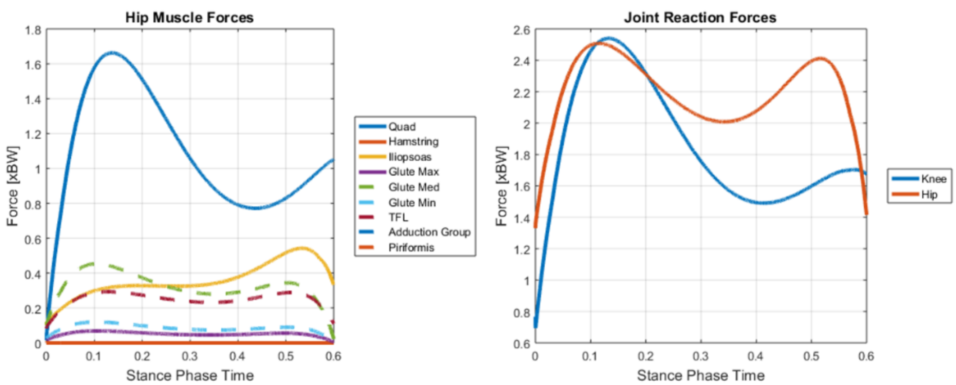

Figure 4-100: The computed hip muscle forces and interaction forces at the knee and hip while using two PID controllers.

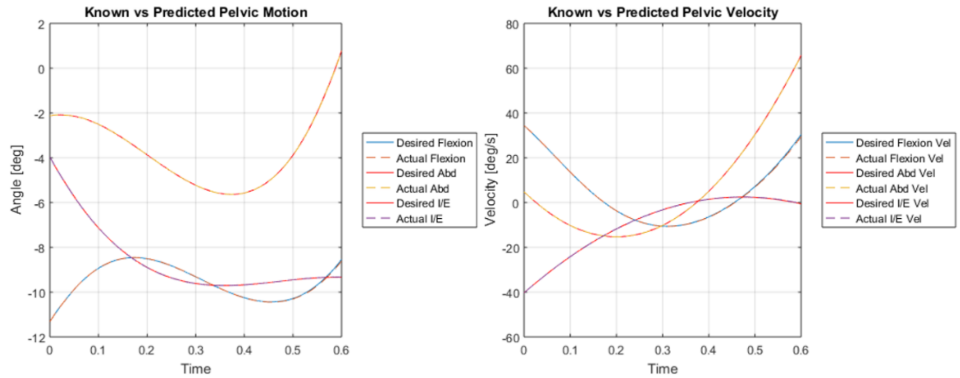

Figure 4-101: The performance of three PID controllers.

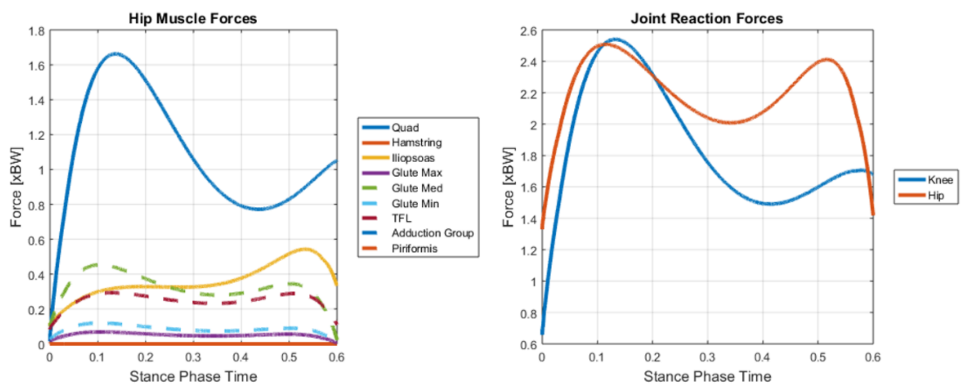

Figure 4-102: The computed muscle forces and interaction forces at the knee and hip.

how the contact detection algorithm and initial parameters affect the stability of the system. If the initial parameters have not been initialized properly, the interaction force at the hip joint will have profiles as shown in Figure 4-103.

The parameters that need to be initialized include initial muscle and ligament forces, initial hip interaction forces, spring and damper coefficients, and initial parameters for PID controllers. In this investigation, all the above parameters have been chosen carefully and tried one by one to the system to obtain the best set of initial values. The interaction forces at the hip joint and other joints, respectively, are shown in Figure 4-104 and Figure 4-105.

From results shown in Figure 4-104 and Figure 4-105, a conclusion can be drawn that for each simulation, it is necessary to obtain a good set of initial parameters in order to avoid instability at the beginning of the simulation. Finding the best set of initial parameters is the most challenging task of mathematical modeling as it takes a great deal of effort and consistency in the approaching methodology. Further studies need to be conducted to automate this process and avoid the human variability factor.

4.6 THEORETICAL AND COMPUTATIONAL ADVANCEMENT

The forward solution mathematical hip model developed in this dissertation provides an excellent theoretical approach for analysis of different surgical conditions, implant performance, and even simulate a virtual surgery of THA. Unfortunately, a thorough master of these resources is challenging without proper training and understanding of how the model works. Therefore, a user-friendly graphic user interface

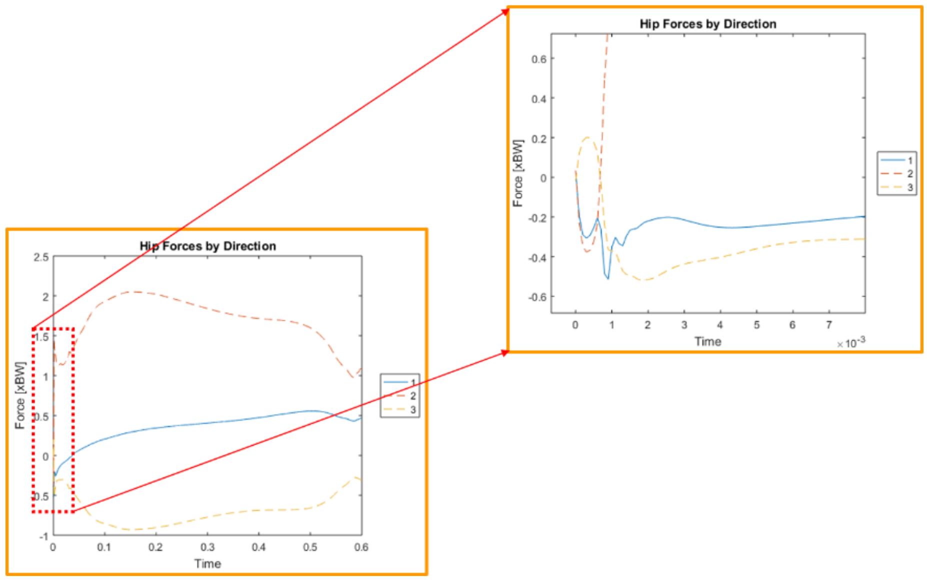

Figure 4-103: The instability occurring at the hip interaction forces caused by improper initialized parameters.

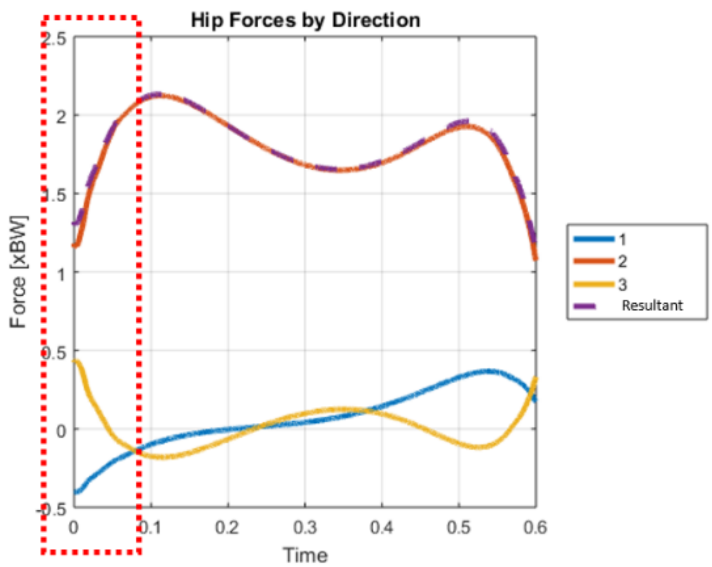

Figure 4-104: The hip forces by direction resulting of a good set of initial parameters.

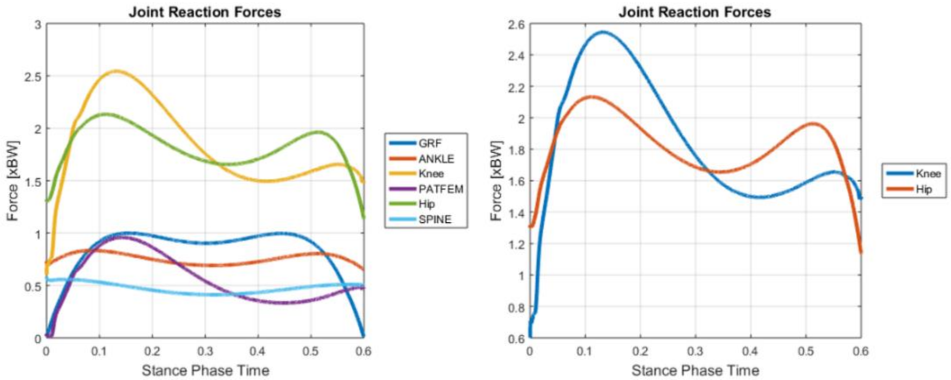

Figure 4-105: The interaction forces at each joint resulting of a good set of initial parameters.

(GUI) is needed. The infrastructure of the forward solution mathematical model is depicted in Figure 4-106.

Along with the reformed infrastructure from the existing mathematical model [61], substantial developments have been conducted in this dissertation to improve the overall performance of the mathematical hip model. New modules and more analysis tools have been implemented and added to the existing program. While the existing program only relied on Matlab and used it as a computational engine and a visualization resource, the advancements implemented within this dissertation were successfully integrated with the powerful VTK engine [75] for both computation and visualization. Details on the use of VTK will be discussed later in this section.

The mathematical model application program interface (API) is depicted in Figure 4-106. The application and analysis modules were developed in Matlab. The .NET VTK API, which is a wrapper of VTK (VTK is originally written in C++), allows for embedding the visualization engine of VTK in the .NET applications. Fortunately, the Matlab API allows the Users to communicate with .NET-based engines, and therefore the visualization engine of VTK can be employed in Matlab. VTK itself is a set of methods developed in C++ and primarily used for computer graphics, image processing, and visualization, not for a GUI development. Therefore, a shortcoming of using VTK in Matlab is that the VTK visualization window cannot be embedded in a GUI developed in Matlab, resulting in the use of a separate GUI and a visualization window. Regardless of this shortcoming, the communication between VTK and Matlab was well handled through an API developed in

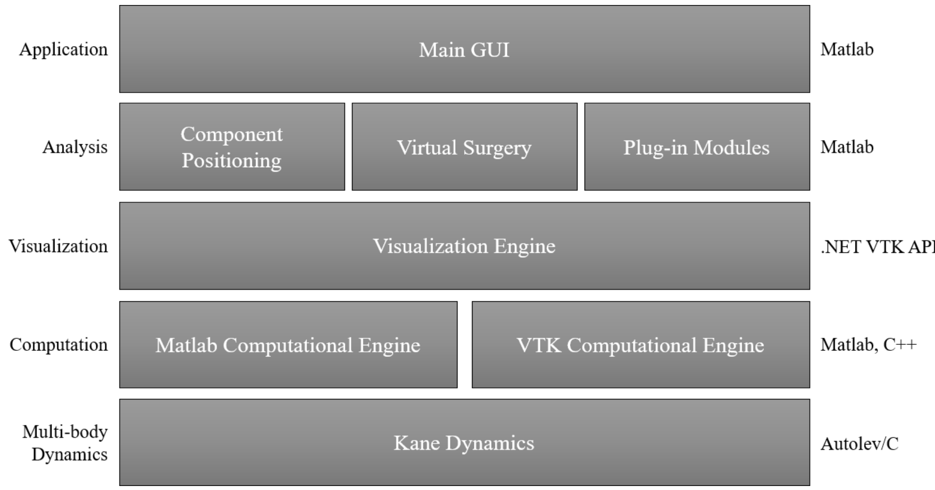

Figure 4-106: The infrastructure of the mathematical hip model.

Matlab that ensures that any changes in the VTK visualization window are immediately updated in Matlab and vice versa.

As mentioned above, not only is VTK a visualization engine, it also consists of a variety of methods, often referred to as filters, that can work as a computational engine. Fortunately, VTK filters can be employed in Matlab to do many of the required tasks that empower and accelerate the computations being carried in Matlab. Matlab, a high-level programming language for engineers, is a matrix-based integrated development environment (IDE), consisting of thousands of functions and toolboxes that provide powerful computation and simulation resources for quick development of prototypes. However, it is a computationally expensive engine, and sometimes does not meet the User needs. On the other hand, VTK is originally written in C++, a lower level programing language than Matlab. Therefore, computational time in VTK is much faster than in Matlab, for the same task.

Kane dynamics is a central component of the mathematical model developed within this dissertation. Implemented within Autolev, it is a symbolic programming language for solving multi-bodies dynamic problems. The mathematical model developed within this dissertation was originally written in Autolev [61]. Autolev was then used to compile and export the mathematical model into C. The C code of the mathematical model was later compiled in the Visual Studio that outputted an executable file of the mathematical model. This executable file takes input parameters (surgical conditions), kinematic outputs and dynamic results (surgical outcomes). Depending on the complexity of each required analysis, the mathematical hip model developed in this dissertation takes approximately two minutes to complete a simulation.

4.6.1 Main GUI and Analyses

The main GUI and plug-in analyses are built on top of Kane dynamics that was developed within Autolev, providing a user-friendly interface and allowing multiple analyses in only one platform. Rather than replacing the existing GUI and analyses in the original program, new modules have been developed in parellel and added to the main GUI. A brief introduction of each module will be represented as the following.

4.6.1.1 Anatomical Landmarking GUI

The anatomical landmarking GUI allows the User to predict anatomical landmarks on a new bone model given a set of landmarks on a template model. The algorithm driving this tool has been extensively discussed in a previous section. In this section, only a general introduction about the GUI will be discussed. As shown in Figure 4-107 the anatomical landmarking GUI contains minimal buttons, allowing ease of use.

Once the User chooses the “Load Data” button, the GUI allows the User to select a subject that he or she desires to predict the desired landmarks. The GUI guides the User step by step to complete the anatomical landmarking process. Therefore, as shown in Figure 4-107 the Initial Mapping and Run buttons are deactivated. They will be activated once the previous step is completed. As the User follows the guidance of the GUI and once the anatomical landmarking is completed on the new bone model, the visualization window will pop-up revealing the landmark prediction results as shown in Figure 4-108.

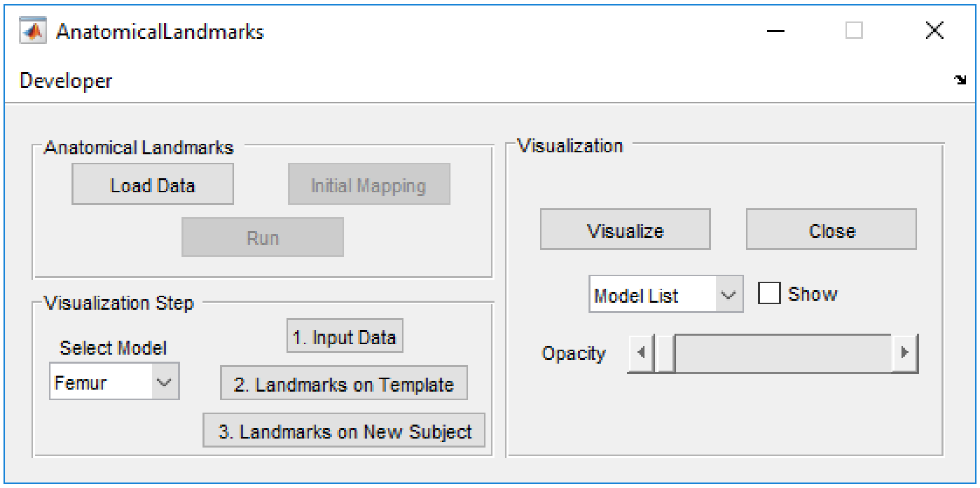

Figure 4-107: The anatomical landmarking prediction GUI.

Figure 4-108: The VTK visualization window allows to visualize the results of anatomical landmarks on the new bone model.

4.6.1.2 Implant Positioning GUI

There are two separate GUIs for cup positioning and femoral stem positioning in the existing program. In each GUI, the User can customize the position of either the cup or the femoral stem by either translating or rotating the implant CAD model. The finalized position is then saved and used for the analysis. At one time, Users can only manipulate either the cup positioning or the femoral stem positioning GUI. In an attempt to improve such inconvenience, a single GUI has been developed with a powerful visualization capability using VTK. This GUI not only preserved all functionalities of the existing program but also added more useful functions to empower it. This innovative tool allows the User to interact with the implant CAD model through both keyboard and mouse control. The User can either use the keyboard to precisely position the implant or a mouse to handle the position interactively. The interactive window in which users can interact with the implant CAD model is shown in Figure 4-109. This interactive visualization window is communicated with Matlab through a GUI (Figure 4-110). Through this GUI, information can be sent or received from the visualization window to the Matlab platform for further analyses.

An important feature of this visualization tool is that the User can manipulate the positions of both the acetabular cup and the femoral stem at a single window. The GUI allows the User to switch between the cup positioning and the femoral stem positioning mode quickly. At each mode, the implant will be highlighted accordingly to enhance the visual recognition ability. For example, in the cup positioning mode, the cup color will be highlighted while the femoral stem color remains silver; at the femoral stem mode, the femoral stem color will be highlighted while the cup color remains silver (Figure 4-109).

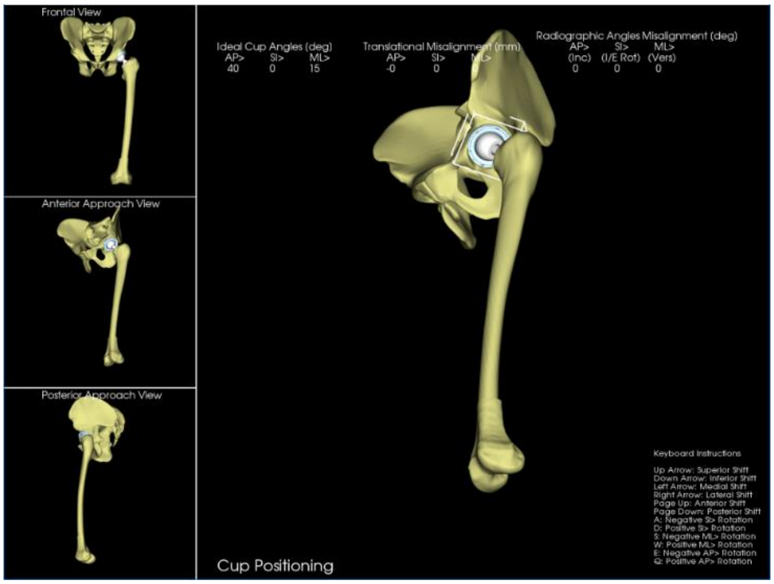

Figure 4-109: The interactive visualization window implemented in VTK that allows for positioning the implant components.

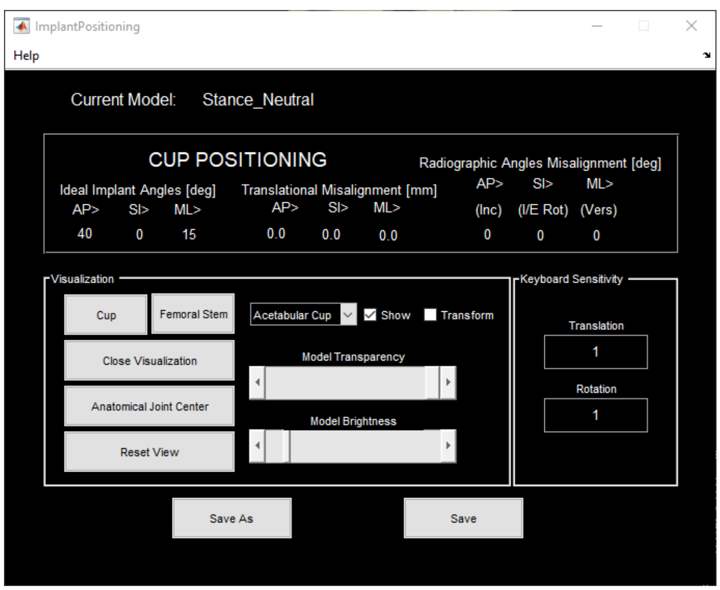

Figure 4-110: The implant positioning GUI is implemented in Matlab that works as a communicator between Matlab and VTK.

Along with the ability to highlight the color of the implant in each mode, information represented in the GUI and the visualization window is instantly synchronized. When switching between the two modes, data in the earlier mode will be saved automatically. It means that if the User makes some changes in the cup positioning mode, these changes are still available in the femoral stem positioning mode. Therefore, if the User only wants to analyze a surgical condition where the cup position is changed, they only need to make sure that the femoral stem is placed at the initial, anatomical position. The algorithm does support the User as he/she attempts to place the implants (cup and femoral stem) at the initial, anatomical positions by using the button "Anatomical Joint Center" which can be triggered by the User to restore the implant ideal position, even if they have been changed.

As shown in Figure 4-109 and Figure 4-111, there are three small views on the left stand representing the three different surgical approaches. When the User changes the position of the cup or the femoral stem from the main view, the change will be synced to these views. As shown in Figure 4-111 the cup was translated and rotated in the main view and the small views simultaneously.

4.6.1.3 Virtual Surgery GUI

Virtual surgery is a complicated program that contains three GUIs to control each surgical procedure and function as APIs to sync information between the virtual surgery environment and the Matlab platform.

The main GUI is represented in Figure 4-112, contains the necessary functions to manipulate the entire surgical process: the instrument selection, the surgical approaches,

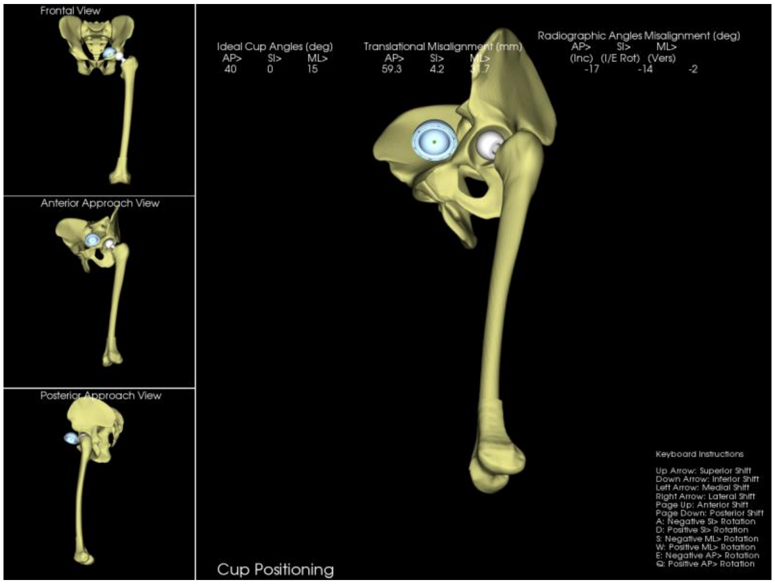

Figure 4-111: The position of the implant component is synced between the main view and three small views.

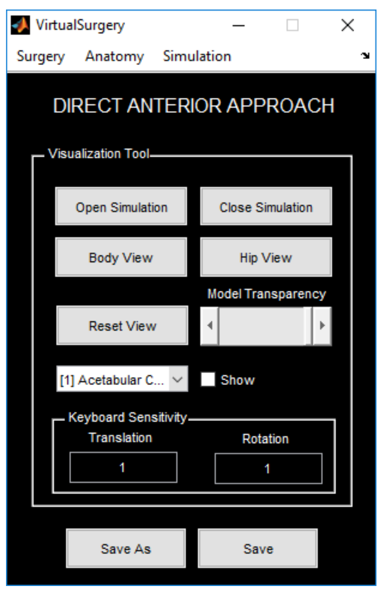

Figure 4-112: The main GUI allows the User to handle and manipulate the virtual surgery.

the soft tissue property management, etc., In the main GUI (Figure 4-112) the Surgery menu includes methods to choose a surgical approach, trigger the Instrument and Implant GUI. The Anatomy menu contains functions to manage muscle and ligament attachment sites and bony geometries. The Simulation menu consists of analysis functions and results.

The Instrument GUI contains functions and methods to manage surgical instruments including a saw, reamers, and broaches (Figure 4-113). For each surgical instrument, two placement options can be used. The auto-placement is triggered by clicking the "Auto Placement" button. In this mode, the program will utilize the implant information and anatomical landmark determination, defined in the previous section, to automatically support the User during the virtual surgery. The manual placement can be triggered by clicking the "Manual Placement" button. In this model, the program will allow the User to proceed with the surgery step by step.

The Implant GUI includes functions and methods to manage the implant position (Figure 4-114). The Cup and Femoral Stem menu allow the User to change the acetabular cup and femoral stem size, respectively. Throughout the Implants GUI, the User can access the Cup Positioning and the Stem Positioning environment. Similar to the Implant Positioning as shown in Figure 4-109, the position of the acetabular cup and the femoral stem can be managed using a single window. Auto and manual placement of the acetabular cup and the femoral stem are implemented to enhance the efficiency of the implant component placement procedure.

The virtual surgery program incorporated the three most popular surgical approaches: the direct anterior approach, the anterolateral approach, and the posterolateral

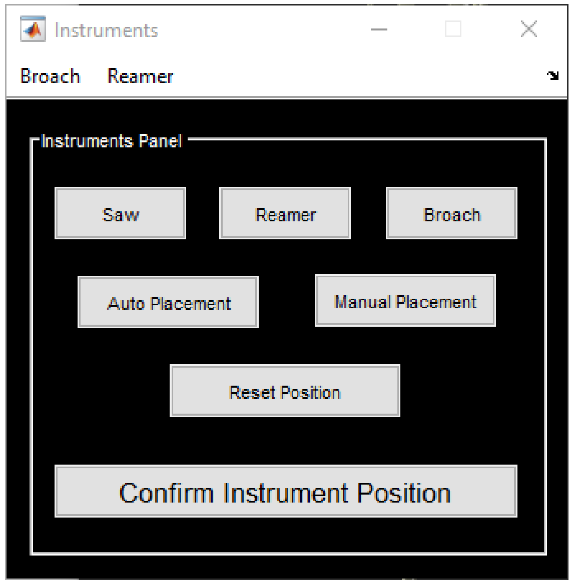

Figure 4-113: The instrument GUI allows the User to select the instruments to proceed to remove the femoral head, reaming the acetabulum or broaching the femoral canal.

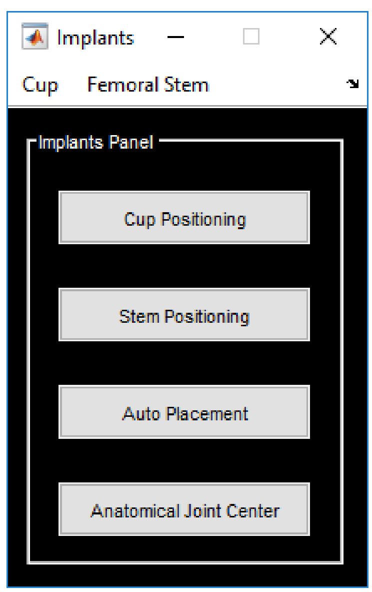

Figure 4-114: The implant GUI allows the User to handle the implant component position.

approach. For each surgical approach, Users can either view the whole scene that includes the surgical table and the patient or zoom in the hip joint where the virtual surgery is being carried out [Insert Figure]. The virtual surgery environment where the anterolateral surgical approach was chosen is shown in Figure 4-115.

4.6.2 Visualization Toolkit (VTK)

VTK [75] has been intensively used throughout this dissertation not only for visualization but also for computation. VTK, which is developed by Kitware Inc., is open-source software for 3D computer graphics, image processing, and scientific visualization. It consists of more than 2500 classes with more than 50000 public and protected class members. The core functions of VTK is written in C++ to maximize its capabilities.

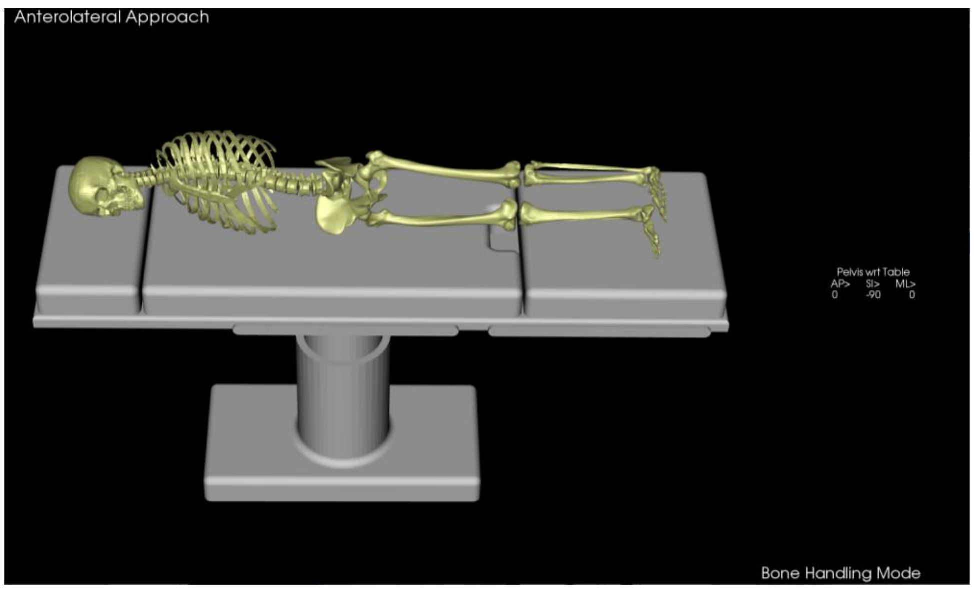

Figure 4-115: Patient and table set up for the anterolateral surgical approach.

Fortunately, VTK supports automated wrapping of the C++ core into Python, Java, Tcl, and .NET so that VTK can be reached by a variety of programmers in multiple programming languages. VTK is also cross-platform that can runs on Windows, Mac, Linux, and Unix platforms.

In this section, VTK will be briefly introduced. As VTK has been used in many aspects of this dissertation, there is no way to describe everything about how and where VTK is used. Therefore, VTK will be introduced and discussed through a fundamental example. This example was implemented in Matlab using a .NET wrapper of VTK and played as a basis for other applications of VTK used within this dissertation. For complete details of VTK, please visit the VTK official website at vtk.org.

For example, if there is a CAD model of the femoral bone with the .stl extension that needs to be visualized, the User only needs to follow the VTK visualization pipeline. The general visualization pipeline in VTK is depicted in Figure 4-116.

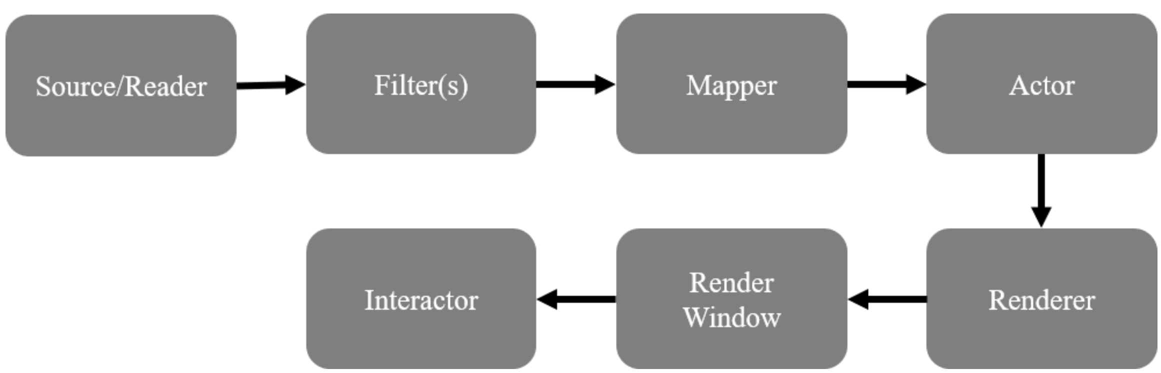

Figure 4-116: The VTK visualization pipeline.

VTK provides various source classes that can be used to construct simple geometric objects, such as points, spheres, lines, cubes, cylinders, and etc. VTK also allows the user to import mesh models in various formats like vtk, stl, obj, vtp, etc., and supports corresponding methods to read these files. For example, the User can use the vtkPolyDataReader class to load a .vtk file or the vtkSTLReader class to load a .stl file. The following codes read a .stl file that represents a femoral bone into VTK.

```
% Load the stl file
vSTLReader = vtkSTLReader.New();
vSTLReader.SetFileName('femurDemo.stl');
```

One or more filters can be used to take data as input and return the modified data. As shown in Figure 4-117 the input mesh model is applied a smooth filter. The following codes applied a Laplacian smoothing filter to the input bone model.

```
% Apply visualization filter to the input data
vFilter = vtkSmoothPolyDataFilter.New();
vFilter.SetNumberOfIterations(50);
vFilter.SetRelaxationFactor(0.5)
vFilter.SetInputConnection(vSTLReader.GetOutputPort());
```

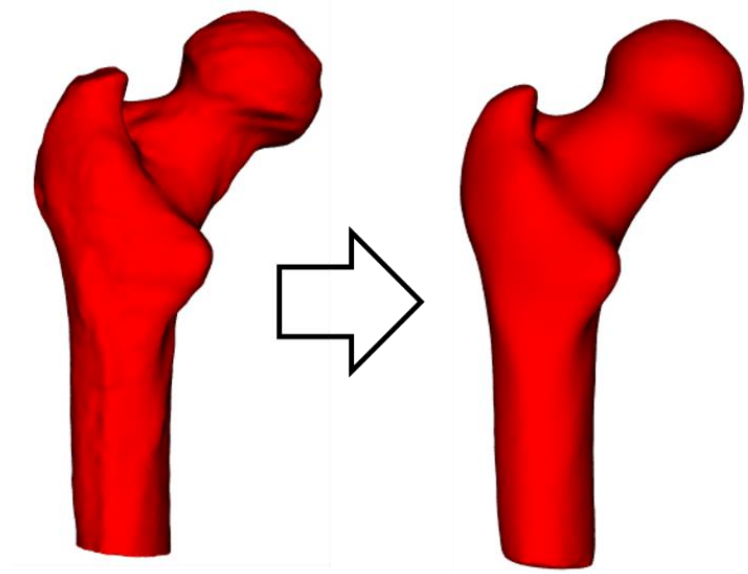

Figure 4-117: A smoothing filter is applied to the original bone model (left image), resulting in a smoothed bone model (right image).

The mappers can utilize a mapping technique to define the data that was output from the filtering process to graphics primitives like points, line, or triangles that can be understood and displayed by the renderer. Some fundamental primitives used in VTK are shown in Figure 4-118. The following codes created a vtkPolyDataMapper to transform the data into graphic primitives.

```
% Create a graphical mapper
vMapper = vtkPolyDataMapper.New();
vMapper.SetInputConnection(vFilter.GetOutputPort());
```

vtkActor represents the model in a renderer scene. In this example, the femoral bone is set at the color to be red.

```
% Create an actor
vActor = vtkActor.New();
vActor.SetMapper(vMapper);
vActor.GetProperty().SetColor(1,0,0);
```

In the rendering process, VTK converts 3D graphic primitives with a specification for lights, materials, and a camera view into a 2D image that can be displayed on the screen (Figure 4-119). In this example, the background of the scene is set to white. VTK uses a default camera and light setting if no light sources and cameras are declared.

```
% Create a scene renderer like camera, lights, ...
vRenderer = vtkRenderer.New();
vRenderer.AddActor(vActor);
vRenderer.SetBackground(1, 1, 1);
```

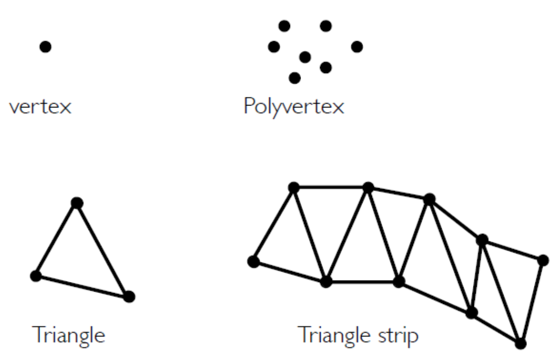

Figure 4-118: Examples of graphics primitives used in VTK.

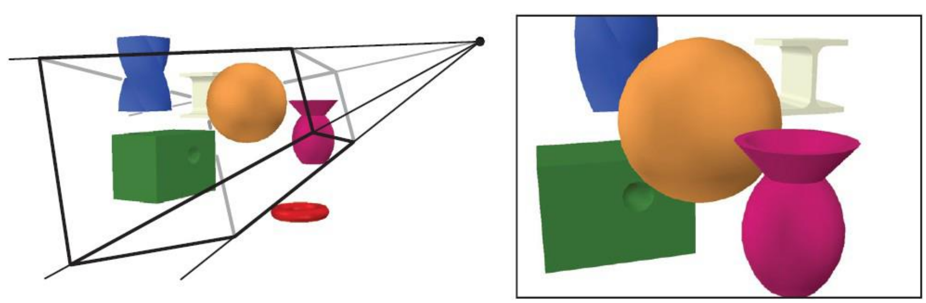

Figure 4-119: 3D graphic primitives are converted into a 2D image that can be displayed on the screen. Image from (ealtimerendering.com).

The vtkRenderWindow class creates a window for renderers to draw into. In this example, a rendering window is created and set at a resolution of 500x500 pixel.

```
% Create a window on the screen to visualize the data
vRenWin = vtkRenderWindow.New();
vRenWin.AddRenderer(vRenderer);
vRenWin.SetSize(500, 500);
```

The vtkRenderWindowInteractor class provides the ability to interact (rotate/zoom/pan) the camera, select and manipulate actors.

```
% Create support for mouse interaction
vInteractor = vtkRenderWindowInteractor();
vInteractor.SetRenderWindow(vRenWin);
```

The following codes demo the complete process to visualize a .stl file that represents a femoral bone. This program was implemented in Matlab 2016a using Windows Operating System. In this demo, the femoral bone is applied the Laplacian filter to smooth its surface. A comparison of the original and the smoothed bone model is shown in Figure 4-120.

```
NET.addAssembly('C:\Program Files\ActiViz.NET 5.8.0 OpenSource Edition\
Kitware.VTK.dll');
import Kitware.VTK.*;

% Load the stl file
vSTLReader = vtkSTLReader.New();
vSTLReader.SetFileName('femurDemo.stl');

% Apply visualization filter to the input data
vFilter = vtkSmoothPolyDataFilter.New();
vFilter.SetNumberOfIterations(50);
vFilter.SetRelaxationFactor(0.5)
vFilter.SetInputConnection(vSTLReader.GetOutputPort());

% Create a graphical mapper
vMapper = vtkPolyDataMapper.New();
vMapper.SetInputConnection(vFilter.GetOutputPort());
```

```
% Create an actor
vActor = vtkActor.New();
vActor.SetMapper(vMapper);
vActor.GetProperty().SetColor(1,0,0);

% Create a scene renderer like camera, lights,...
vRenderer = vtkRenderer.New();
vRenderer.AddActor(vActor);
vRenderer.SetBackground(1, 1, 1);

% Create a window on the screen to visualize the data
vRenWin = vtkRenderWindow.New();
vRenWin.AddRenderer(vRenderer);
vRenWin.SetSize(500, 500);

% Create support for mouse interaction
vInteractor = vtkRenderWindowInteractor();
vInteractor.SetRenderWindow(vRenWin);

% Start visualization and interaction.
vInteractor.Initialize();
vRenWin.Render();
vInteractor.Start();
vRenWin.FinalizeWrapper();
```

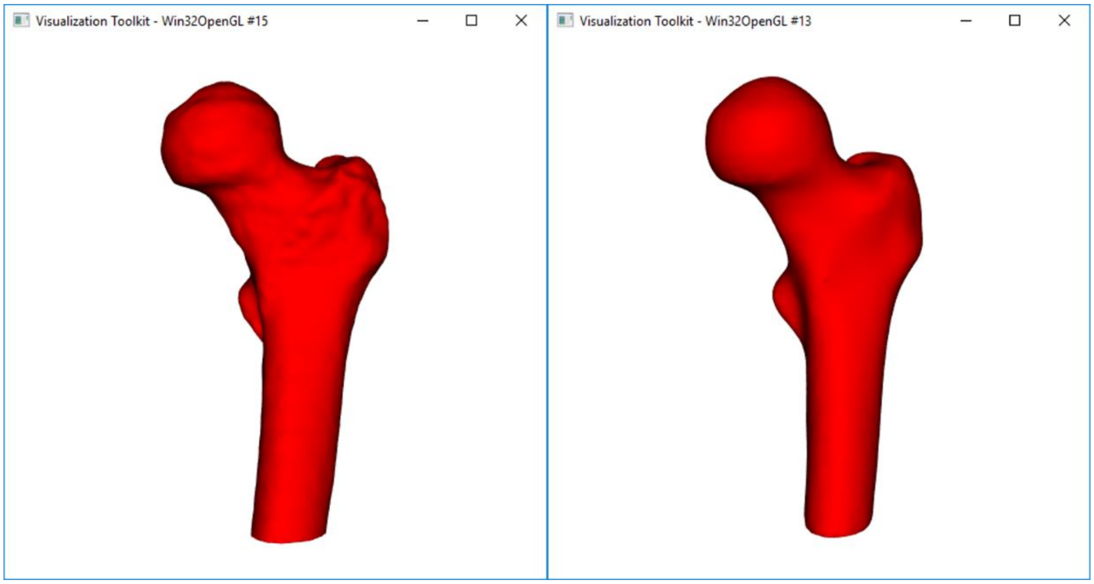

Figure 4-120: A comparison of the original femoral model (left image) and its smoothed model (right image).

In summary, a simplified introduction of VTK was discussed in this section. In fact, more complicated and advanced VTK visualization techniques are utilized in this dissertation to simulate customized simulations like virtual surgery, anatomical landmarking, measurement of femoral morphology, and etc. The readers, who desire to learn more VTK, are encouraged to visit the VTK website and online tutorials.

CHAPTER 5: RESULTS AND DISCUSSION

5.1 TOTAL HIP ARTHROPLASTY SIZING PREDICTION

Eight subjects were recruited for this study. Four of these subjects had healthy hips and the other four subjects were diagnosed with hip osteoarthritis and were candidates for total hip replacement. All eight subjects gave their consent for a CT scan with institutional review board approval (UTK IRB-15-02631-FB). 3D bone models of the pelvis and femoral bones were created using both Avizo (Thermo Fisher Scientific, Altham, MA, USA) and 3D Slicer [98] segmentation software and during the process the cancellous bone, including the femoral canal were defined. Four subjects with degenerative hips then received the Corail stem and Pinnacle acetabular Total Hip System (Depuy Synthes, IN, USA) using the direct anterior approach by a single surgeon. Before total hip arthroplasty surgery, all subjects were asked to perform gait under fluoroscopy surveillance. After total hip arthroplasty surgery, two of the four subjects with hip implants came back to the study and were again asked to perform gait under fluoroscopic surveillance. The fluoroscopic videos of each subject were then digitalized and stored in a secured server at the Center for Musculoskeletal Research located at the University of Tennessee Knoxville. Kinematics of each subject were then analyzed using a 3D to 2D registration technique [99]. From the 3D to 2D registration technique, placement of the hip implant components of the two returned subjects was also obtained.

5.1.1 Morphology of The Proximal Femur

The automated measurement of femur morphology algorithm has successfully measured the proximal femoral morphology for all subjects. A summary of the morphology of the proximal femur for all subjects is shown in Table 5-1.

For each subject, the proximal canal morphology was also analyzed and stored in the computer. The center and radius of each incircle along with the relative distance of each incircle to the anatomical femoral center were obtained and stored in a text file for further analysis. This information formed the morphology of the proximal canal, a new concept that has limited investigation. A portion of the text file that represent the canal morphology of subject one is shown in Table 5-2.

Table 5-1: Summary of proximal femoral morphology of eight subjects.

	Femoral Head Diameter	**Femoral Offset**	**Femoral Neck Shaft Angle**
Patient 1	40.379728	34.567338	134.81025
Patient 2	46.670374	44.013536	131.160583
Patient 3	43.678182	24.63496	151.413198
Patient 4	46.910389	42.948052	129.096052
Patient 5	48.925942	48.874994	115.200146
Patient 6	46.705199	43.817417	119.688905
Patient 7	40.118208	39.088136	124.283452
Patient 8	46.229955	40.860771	115.741198

Table 5-2: A portion morphology of the proximal canal of subject 1.

Radius	X-Center	Y-Center	Z-Center	Relative distance to the femoral head center
7.546765	-13.2307	134.969	-18.7258	74.828403
7.456658	-12.9346	133.969	-18.6297	75.828403
7.368849	-12.6296	132.969	-18.4748	76.828403
7.288155	-12.3906	131.969	-18.4081	77.828403
7.210743	-12.1479	130.969	-18.335	78.828403
7.087511	-11.9801	129.969	-18.3409	79.828403
6.958147	-11.7329	128.969	-18.3198	80.828403
6.828774	-11.4332	127.969	-18.2705	81.828403
6.710648	-10.9123	126.969	-18.1817	82.828403
6.616593	-10.5106	125.969	-18.1437	83.828403

As shown in Table 5-2, each row represents information of an incircle: the radius, the coordinate of the center in the global coordinate, and the relative distance of the incircle's center and the anatomical femoral centers. The femoral morphologies of subject one and two are shown in Figure 5-1 and Figure 5-7, respectively.

The proximal femoral morphology is directly influenced by the performance of the anatomical landmarking results. It is important to understand how the proposed automated prediction process for anatomical landmarks is performed. Each step in the proposed anatomical landmarking framework plays a key role and exhibits potential limitations and marginal errors.

The initial alignment is needed to reduce translational and orientational differences between the template and new bone models and to accelerate the convergent rate as well

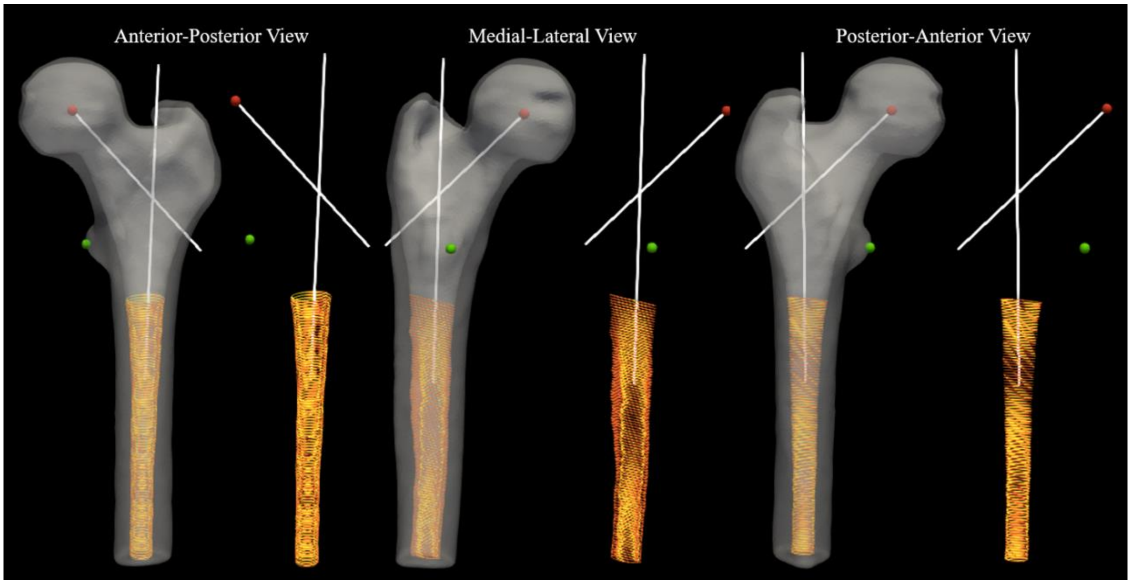

Figure 5-1: Proximal femoral morphology of subject 1.

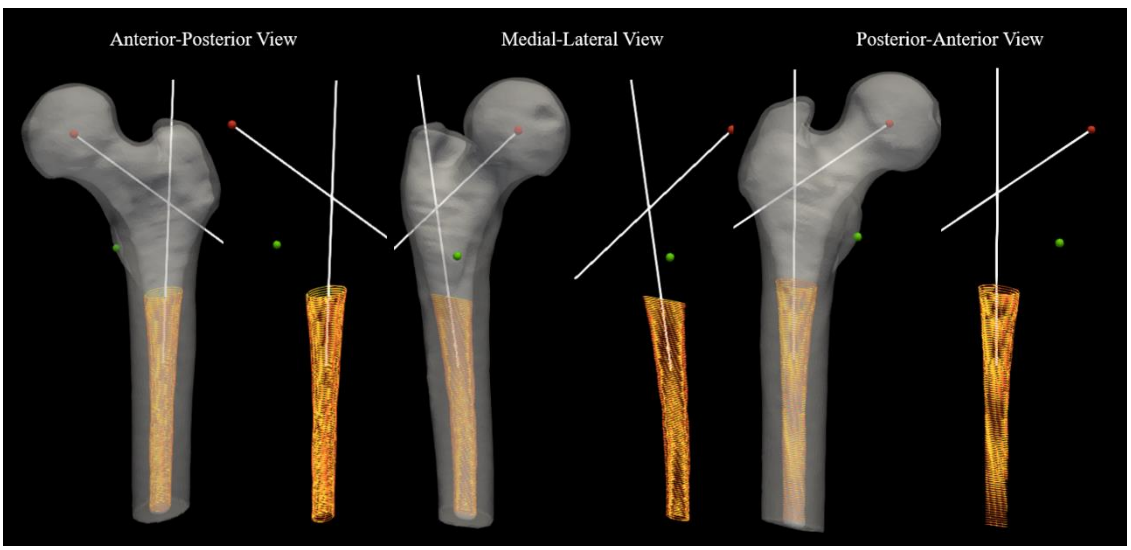

Figure 5-2: Proximal femoral morphology of subject 2.

as the accuracy of the proposed algorithm. The initial alignment proposed in this dissertation was done through an interaction with the CAD model in the visualization environment powered by the VTK library [75]. This approach seems to be straight forward to engineers, but quite challenging to orthopaedic surgeons as they prefer using the defined landmarks and have limited experience interacting with the CAD model. However, the approach was implemented in such a way that it is user-friendly. Users with minimal human anatomy background or limited CAD experience can also use the software to accelerate initial alignment process.

The ICPs algorithm [74] is robust and efficient enough to register any geometry. However, it still exhibits some limitations. ICPs algorithm always converges to the nearest local minimum of mean square error, and therefore, always exists a transformation matrix that best aligns the template to the new bone model. If the initial alignment is not close enough, the ICPs algorithm still converges but not to the best alignment position. Malalignment of two bone models can result in inaccurate predicted landmarks on the new bone model.

Given a good initial alignment, the initial global registration works well if the new bone model does not have a high deformity. Even though the ICPs algorithm added the scaling factor that deforms the template bone model to match the new bone model, high deformity of the new bone model would contribute to an unexpected alignment, resulting in poor corresponding regions between the two bone models. High deformity or abnormal femoral bone geometry can occur in many ways. One such way is in patients with increased femoral anteversion and femoral neck retroversion, in which the femoral head is shaped with an inward/outward twisting, leading to the knee and feet to turn inward/outward (Figure 5-3).

Another common type of high deformity of the femur is hip dysplasia (Figure 5-4). Hip dysplasia often occurs in new born babies in which the hip socket does not fully cover the femoral head, causing the hip joint to become partially or completely dislocated. A normal socket can be defined by the shape of a bowl, whereas a dysplastic hip more resembles a saucer in shape. This disorder, if not diagnosed and treated early, may develop and lead to one leg being longer than the other. It may lead to an increase or decrease in the femoral neck shaft angle as well.

Femoral abnormalities including coxa valga and coxa vara (Figure 5-5) make it challenging to predict the anatomical landmarks using the proposed algorithm. While the template femoral bone model was selected to be a normal femoral bone with the femoral neck shaft angle at about 135-degree, coxa valga and coxa vara femurs are challenging to align with the normal femur. Fortunately, the proposed algorithm is robust enough to overcome this challenge. Three of the eight subjects participating in this study had the coxa vara femurs (the femoral neck shaft angle is smaller than 125 degrees) and one subject had the coxa valga femur (the femoral neck shaft angle is greater than 139 degrees). The proposed algorithm still successfully measured the morphology of these subjects.

Osteoarthritis and the development of osteophytes also contribute to deformity of the femoral head, leading to inaccurate landmark prediction. Osteophytes form along with osteoarthritis, which limits joint movement and typically causes pain (Figure 5-6). To

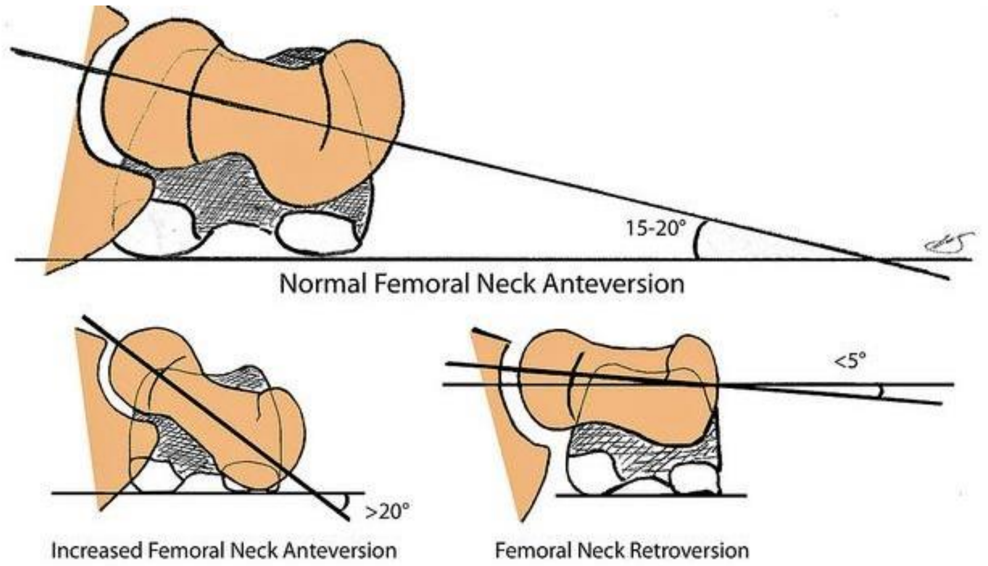

Figure 5-3: Increased femoral neck anteversion and femoral neck retroversion. Image from (www.orthobullets.com).

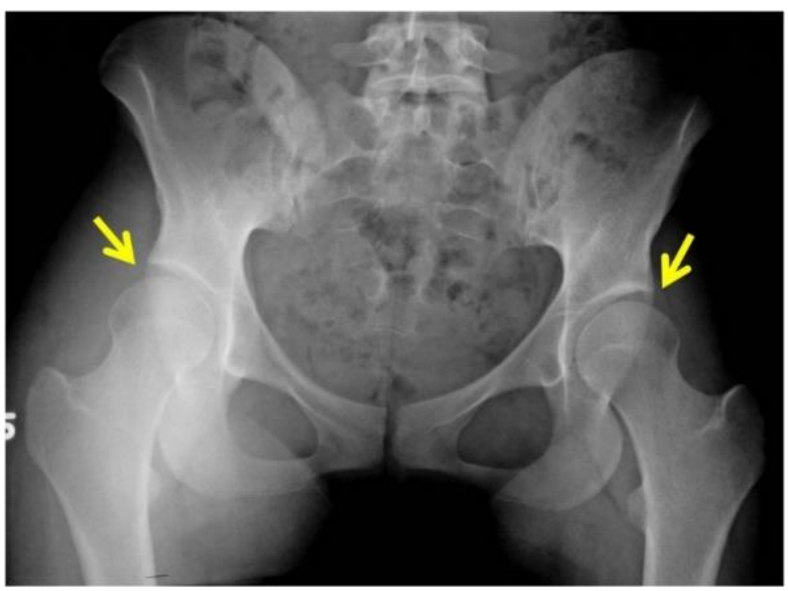

Figure 5-4: X-ray image of a patient with hip dysplasia causing on leg to be longer/shorter than the other. Image from (http://clohisyhipsurgeon.com).

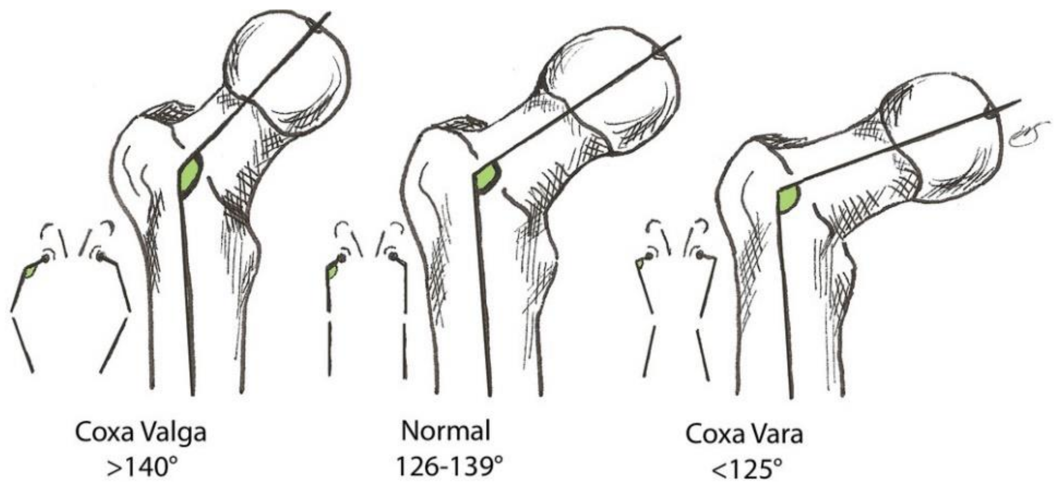

Figure 5-5: Coxa valga and coxa vara hip with abnormal femoral neck shaft angle. Image from (www.pinterest.es).

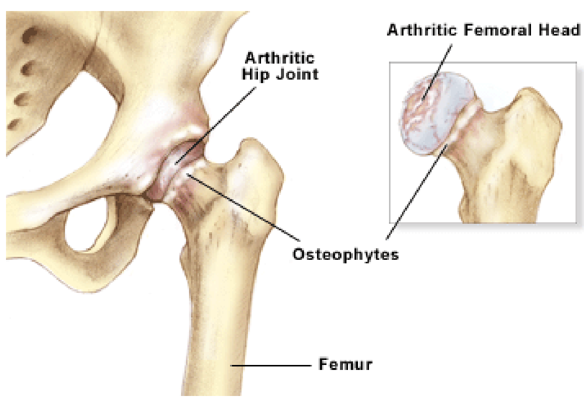

Figure 5-6: Hip osteoarthritis and osteophytes causing deformity of the femoral head. Image from (www.thesteadmanclinic.com).

address this problem, four subjects, who were diagnosed to be in the late stages of hip osteoarthritis and candidates for total hip arthroplasty, were recruited for this study. The proposed algorithm utilized a statistical approach to determine a mean sphere that fits the femoral head point cloud. The spherical fitting function was run multiple times to fit the femoral head point cloud. Each time it generated a fitting sphere. The final sphere, representing the femoral head, is determined to be an average sphere with respect to all fitting spheres.

5.1.2 Prediction of Total Hip Arthroplasty Sizing

Similar to the morphology of the proximal femur, morphology of each femoral stem in the database was obtained. A portion of morphology of the standard size 8 Corail stem is shown in Table 5-3.

Table 5-3: A portion morphology of the standard size 8 Corail stem.

Radius	X-Center	Y-Center	Z-Center	Relative distance to the stem head center
10.19949	-13.5994	156.784	-15.8475	46.013
10.13173	-13.5721	155.784	-15.9436	47.013
10.00146	-13.3065	154.784	-16.114	48.013
9.614732	-13.2073	153.784	-16.5332	49.013
9.568398	-13.0862	152.784	-16.6144	50.013
9.503381	-13.0739	151.784	-16.7034	51.013
9.376675	-12.9752	150.784	-16.8626	52.013
9.072728	-12.68	149.784	-17.2008	53.013
9.006381	-12.5916	148.784	-17.2495	54.013

The automated total hip arthroplasty sizing prediction algorithm has successfully predicted the implant size for each subject. Due to lack of implant components in the database, a small number of Corail stem and Pinnacle acetabular models were used for analysis. Therefore, the result shown in this section is based on the available implant models in the database. The predicted implant sizing information for all patients was summarized in Table 5-4.

In order to illustrate the meaning of each number and information as shown in Table 5-4, the sizing information of patient 1 was chosen to be discussed. The information in the stem column represents the stem size. The predicted stem is a standard Corail stem with size 10. In the head column, +5 is the femoral head length, 28 mm represents the femoral head diameter, and 12/14 is two diameters at the ends of the femoral neck taper. For each femoral head size, there are a variety of neck lengths, allowing for adjustments to soft tissue tension and leg length equality. In the shell column, 50 mm OD represents the outer diameter size of the shell. In the liner column, neutral is liner type, 20 mm ID is the inner diameter of the liner, and 50 mm OD is the outer diameter of the liner.

Two random patients were selected for analysis to see how the predicted femoral stem fits the canal. The cross-sectional, slice, and contact map analysis for the fit of the predicted femoral stem within the canal of patient 1 were shown in Figure 5-7, Figure 5-8, and Figure 5-9, respectively.

Table 5-4: Summary of the prediction implant sizing information for all patients.

	Stem	Head	Shell	Liner
Patient 1	10 Standard	+5, 28 mm, 12/14 taper	50 mm OD	Neutral 28 mm ID, 50 mm OD
Patient 2	12 High Offset	+1, 36 mm, 12/14 taper	58 mm OD	Neutral 36 mm ID, 58 mm OD
Patient 3	11 Standard	+5, 32 mm, 12/14 taper	54 mm OD	Neutral 32 mm ID, 54 mm OD
Patient 4	12 Standard	+5, 36 mm, 12/14 taper	58 mm OD	Neutral 36 mm ID, 58 mm OD
Patient 5	12 High Offset	+5, 36 mm, 12/14 taper	60 mm OD	Neutral 36 mm ID, 60 mm OD
Patient 6	10 High Offset	+5, 36 mm, 12/14 taper	58 mm OD	Neutral 36 mm ID, 58 mm OD
Patient 7	8 Standard	+5, 28 mm, 12/14 taper	50 mm OD	Neutral 28 mm ID, 50 mm OD
Patient 8	12 Standard	+5, 36 mm, 12/14 taper	56 mm OD	Neutral 36 mm ID, 56 mm OD

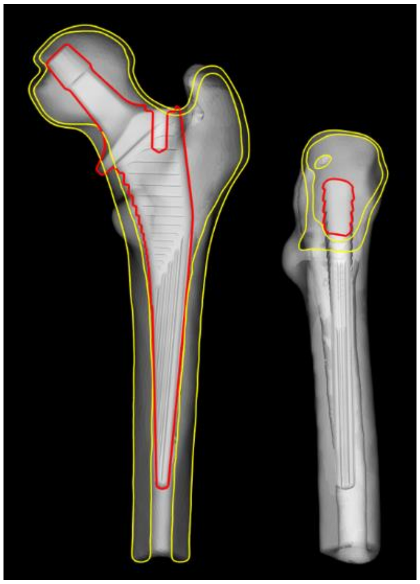

Figure 5-7: Cross-sectional analysis for the fit of the predicted femoral stem within the canal of patient 1.

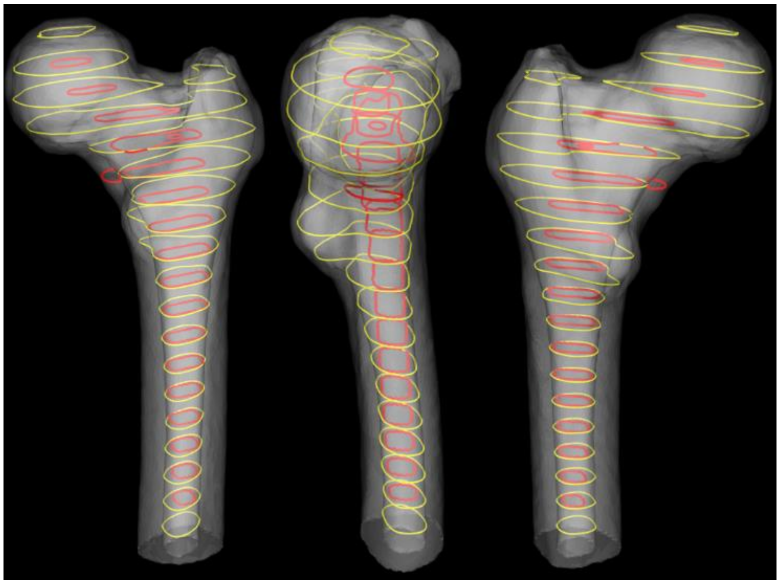

Figure 5-8: Slice analysis for the fit of the predicted femoral stem within the canal of patient 1.

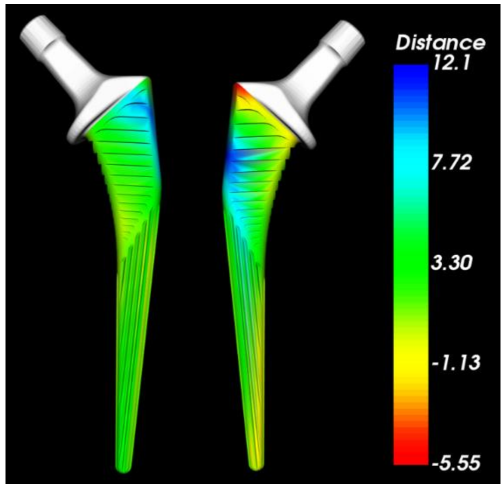

Figure 5-9: Contact analysis for the fit of the predicted femoral stem within the canal of patient 1.

The cross-sectional, slice, and contact map analysis for the fit of the predicted femoral stem within the canal of patient 8 are shown in Figure 5-10, Figure 5-11, and Figure 5-12, respectively.

5.2 FORWARD SOLUTION MODEL ANALYSIS

The forward solution mathematical model developed in this dissertation has played as a basis for the evaluation and prediction of post-operative surgical outcomes. This model is fully capable of simulating different surgical conditions including the implant sizing choices, component placement, reaming and cutting locations, surgical approaches. The model takes surgical conditions as input parameters (pre-operative surgical planning) and calculate and predict kinematics, dynamics of the hip joint post-operatively (possible surgical outcomes).

5.2.1 Functionally Translational Safe Zone

Previous research has defined the existence of a “safe zone” pertaining to the acetabular cup implantation during THA. It is believed that if the cup is implanted at 40°±10° inclination and 15°±10° anteversion, the risk of dislocation is reduced [1]. However, recent studies have documented that even when the acetabular cup is placed within the safe zone, high than expected incidence of dislocation and instability does still exist due to the combination of patient-specific configuration, cup diameter, head size, and surgical approach [100-102]. The “safe zone” only looks into the angular orientation of the cup and completely ignores its translational location. The translational location of the cup can lead to a mismatch between the anatomical hip center and the implant cup center, a concept that has not been widely explored. Therefore, the objective of this section is to

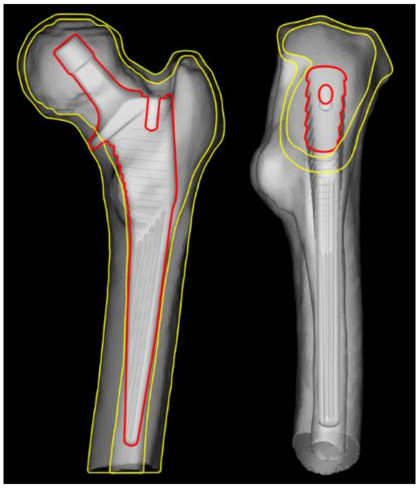

Figure 5-10: Cross-sectional analysis for the fit of the predicted femoral stem within the canal of patient 8.

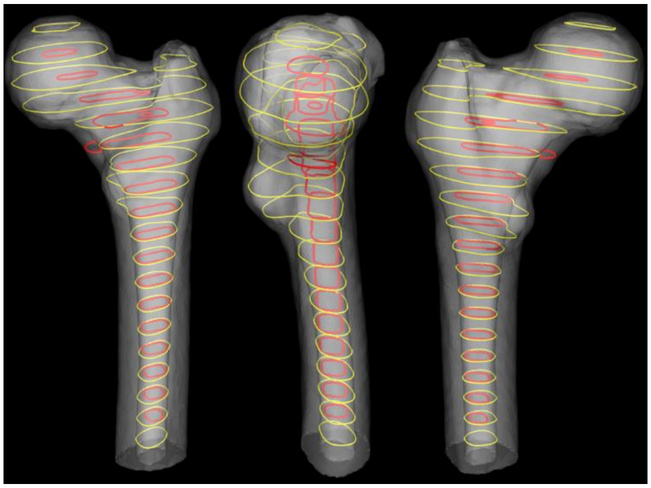

Figure 5-11: Slice analysis for the fit of the predicted femoral stem within the canal of patient 8.

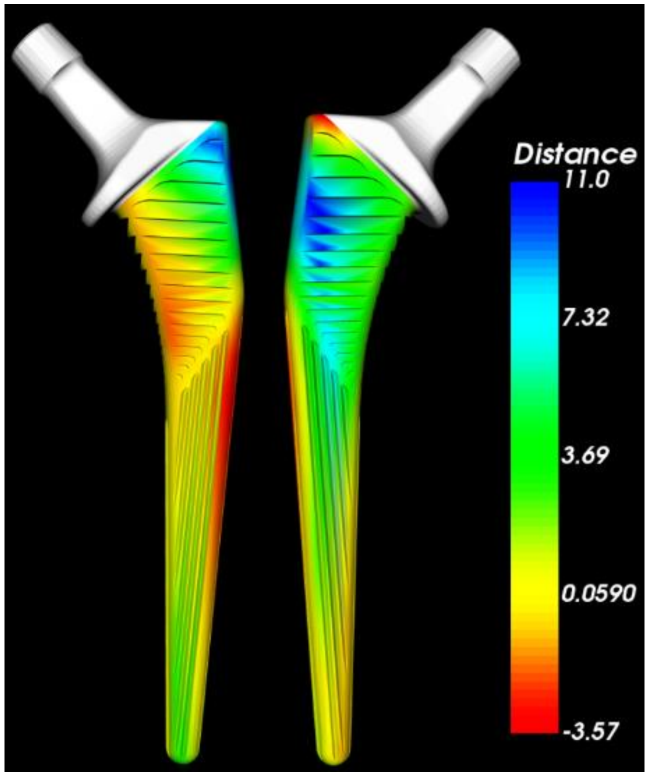

Figure 5-12: Contact analysis for the fit of the predicted femoral stem within the canal of patient 8.

define a zone within which the implanted joint center can be altered with respect to the anatomical joint center, but not influence the likelihood of post-operative hip separation or dislocation. Due to its shape, we define this region as the “optimal conic” safe zone.

There are two steps to identify the optimal conic. The first step is to define a baseline simulation. The baseline was defined where the acetabular cup center was matched to the anatomical hip center, and the orientation of the acetabular cup was 40°/15° (inclination/anteversion). This position is called the ideal position. As shown in Figure 5-13 the placement of the acetabular cup is at the ideal position.

The contact mechanics and muscle/ligament forces in stance phase are shown as in Figure 5-14, Figure 5-15, and Figure 5-16, respectively. The contact mechanics and muscle/ligament forces in swing phase are shown as in Figure 5-17, Figure 5-18, and Figure 5-19, respectively.

In the second step, the acetabular cup orientation remained the same, the location of the cup was shifted in 1 mm increments in all directions to identify the region within which a mismatch between the anatomical hip center and the implant cup center did not lead to separation or instability in the joint. It was observed that during both swing and stance phase when the acetabular cup was placed within the optimal conic with the slant height of 5±1 mm, there appeared no hip instability or dislocation risk associated with the virtual patient. The placement of the acetabular cup within the optimal conic is shown in Figure 5-20.

The contact mechanics and muscle/ligament forces in stance phase are shown in Figure 5-21, Figure 5-22, and Figure 5-23, respectively. The contact mechanics and muscle/ligament forces in swing phase are shown in Figure 5-24, Figure 5-25, and Figure 5-26, respectively.

Furthermore, as the acetabular cup was gradually re-positioned towards the boundary of the optimal conic, hip instability became apparent and tended to increase. When the acetabular cup was placed at the boundary of the optimal conic, slight edge loading occurred at the cup during stance phase, and the hip separation magnitude increased up to 2 mm during swing phase, resulting in a decrease in the contact area and increase contact stress. The placement of the acetabular cup at/near the rim of the optimal conic is shown in Figure 5-27.

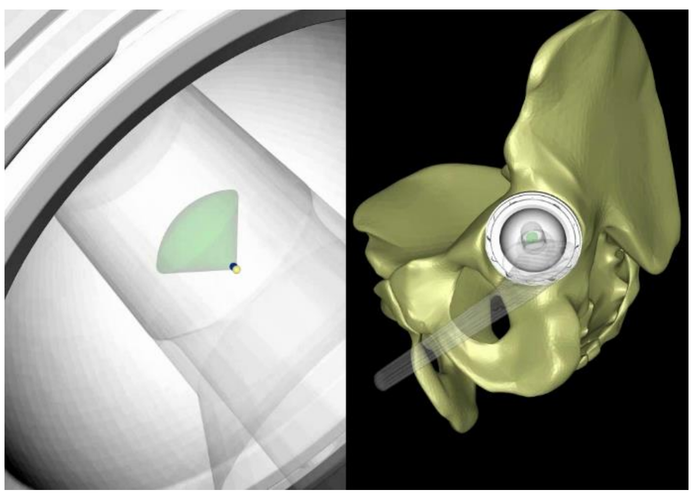

Figure 5-13: The placement of the acetabular cup at the ideal position. The acetabular cup center (yellow dot) is placed at the anatomical hip center. The conic is represented in green, and its center is fixed at the anatomical hip center. The dark blue dot represents the femoral component head center.

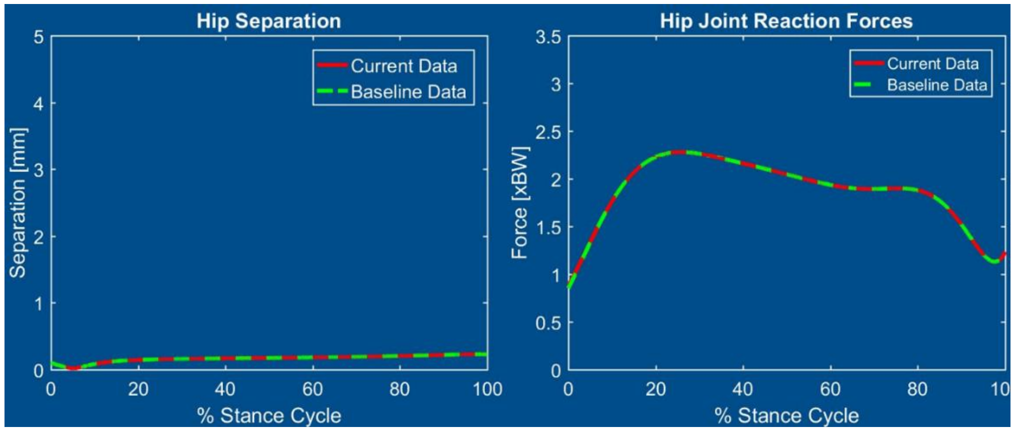

Figure 5-14: Hip separation and hip forces during stance phase when the acetabular cup is placed at the ideal position.

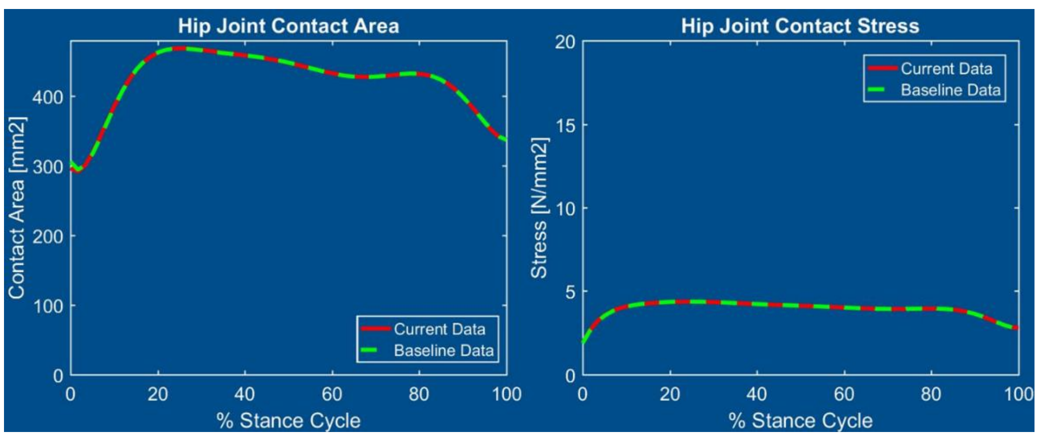

Figure 5-15: Contact area and contact stress at the hip joint during stance phase when the acetabular cup is placed at the ideal position.

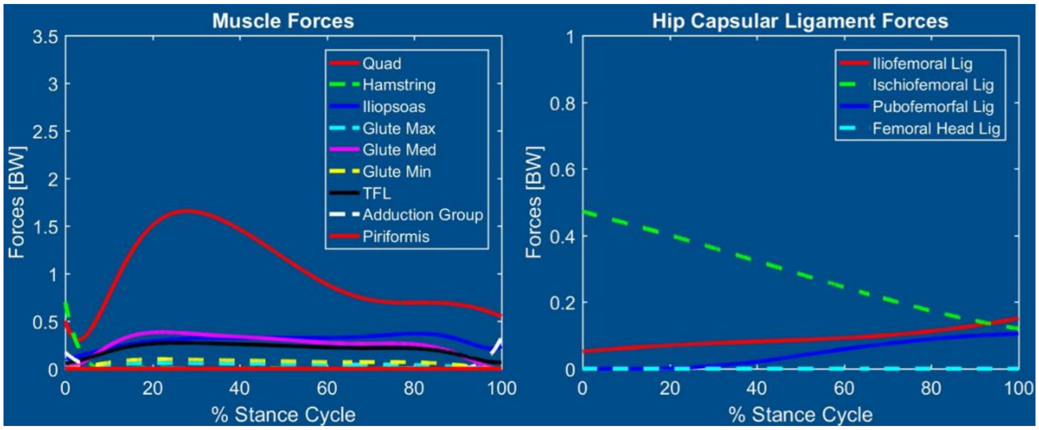

Figure 5-16: Hip muscle and ligament forces during stance phase when the acetabular cup is placed at the ideal position.

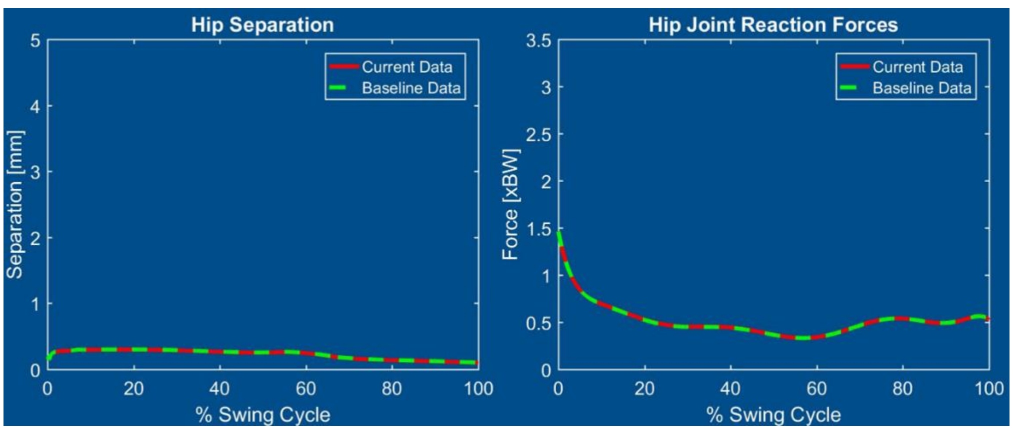

Figure 5-17: Hip separation and hip forces during swing phase when the acetabular cup is placed at the ideal position.

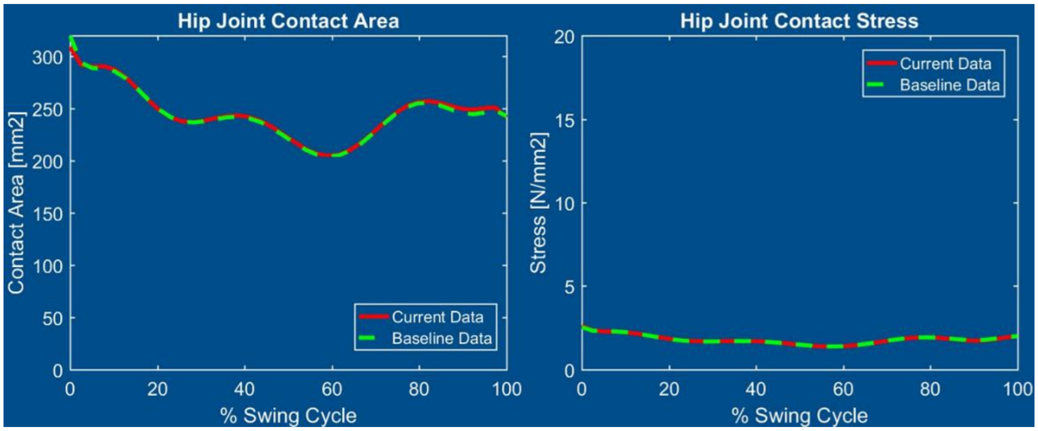

Figure 5-18: Contact area and contact stress at the hip joint during swing phase when the acetabular cup is placed at the ideal position.

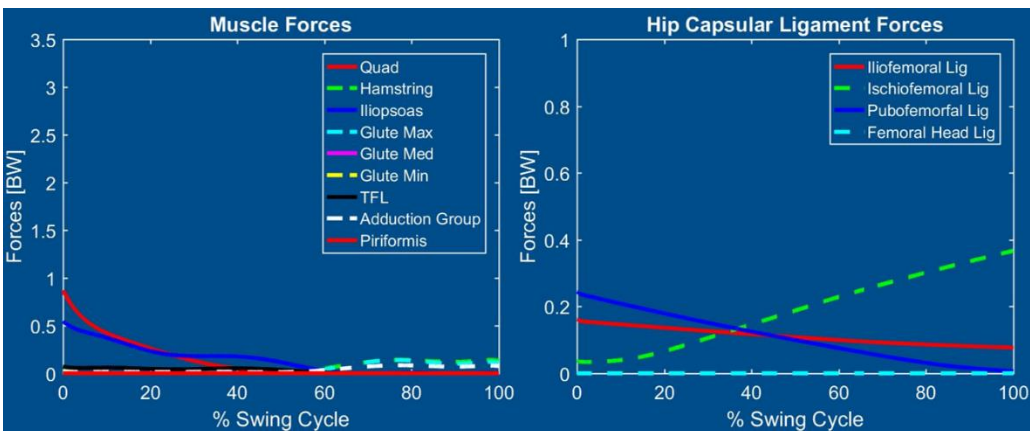

Figure 5-19: Hip muscle and ligament forces during swing phase when the acetabular cup is placed at the ideal position.

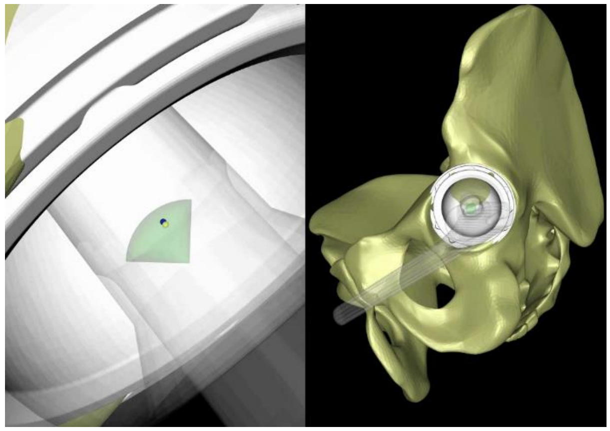

Figure 5-20: The placement of the acetabular cup within the conic. The acetabular cup center (yellow dot) is placed inside the conic. The conic is represented in green, and its center is fixed at the anatomical hip center. The dark blue dot represents the femoral component head center.

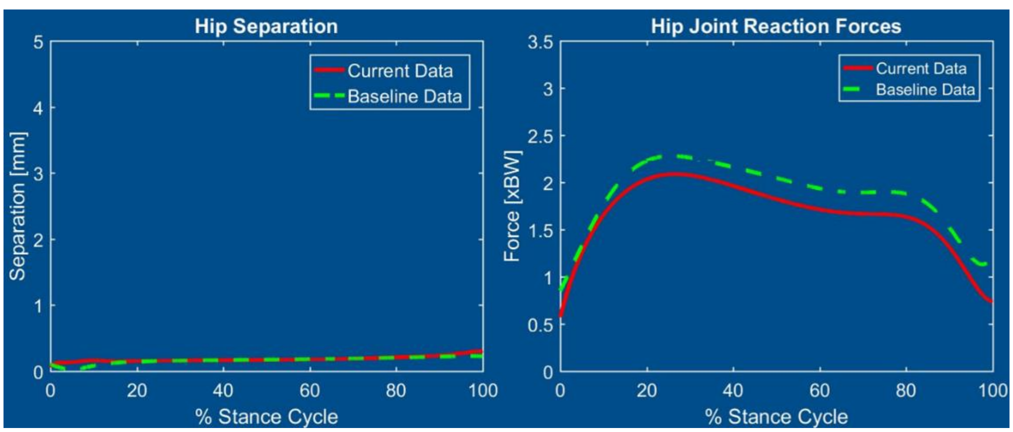

Figure 5-21: Hip separation and hip forces during stance phase when the acetabular cup is placed within the conic.

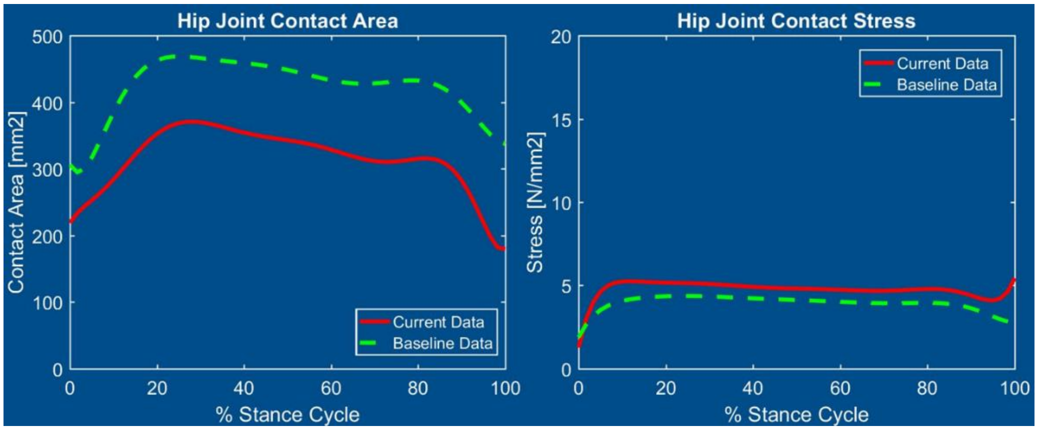

Figure 5-22: Contact area and contact stress at the hip joint during stance phase when the acetabular cup is placed within the conic.

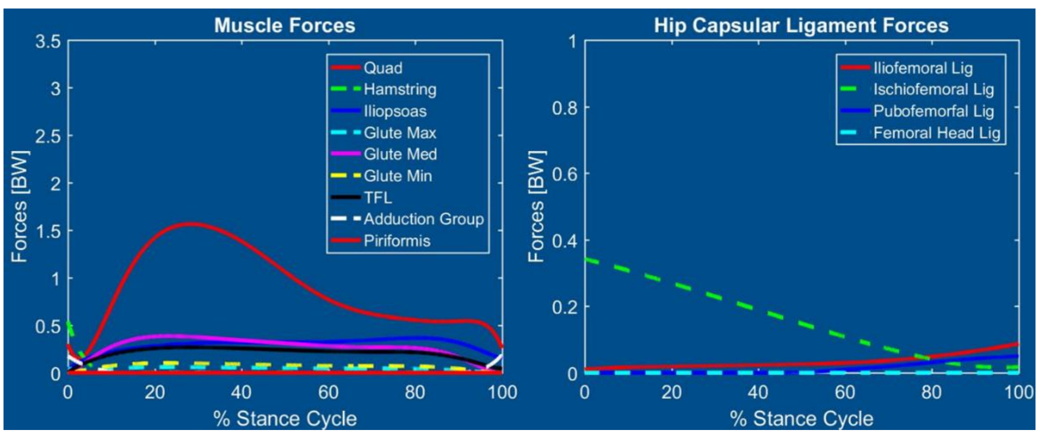

Figure 5-23: Hip muscle and ligament forces during stance phase when the acetabular cup is placed within the conic.

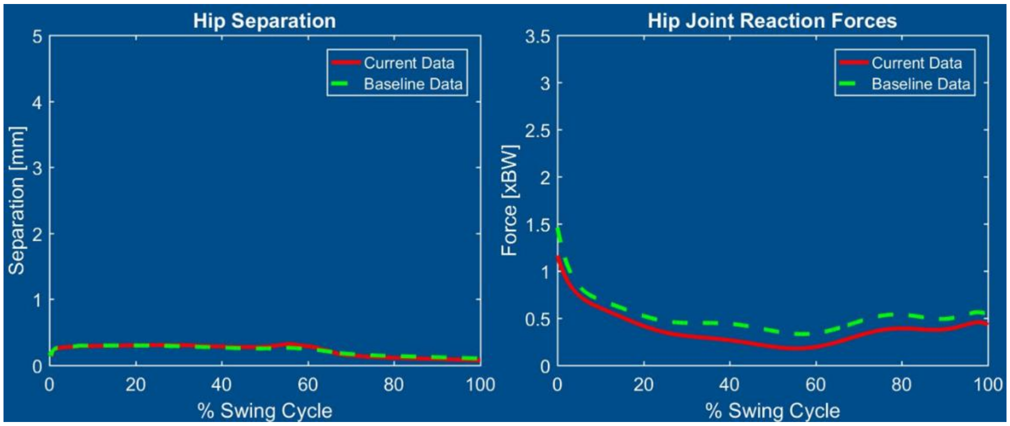

Figure 5-24: Hip separation and hip forces during swing phase when the acetabular cup is placed within the conic.

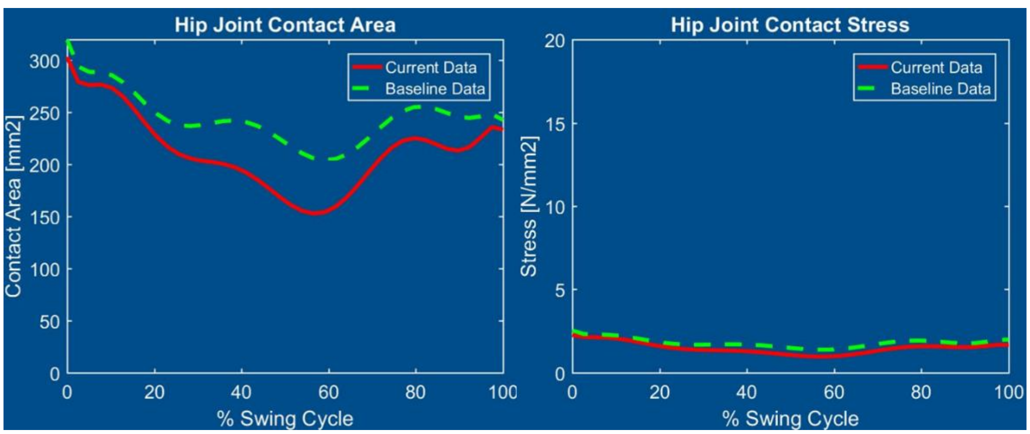

Figure 5-25: Contact area and contact stress at the hip joint during swing phase when the acetabular cup is placed within the conic.

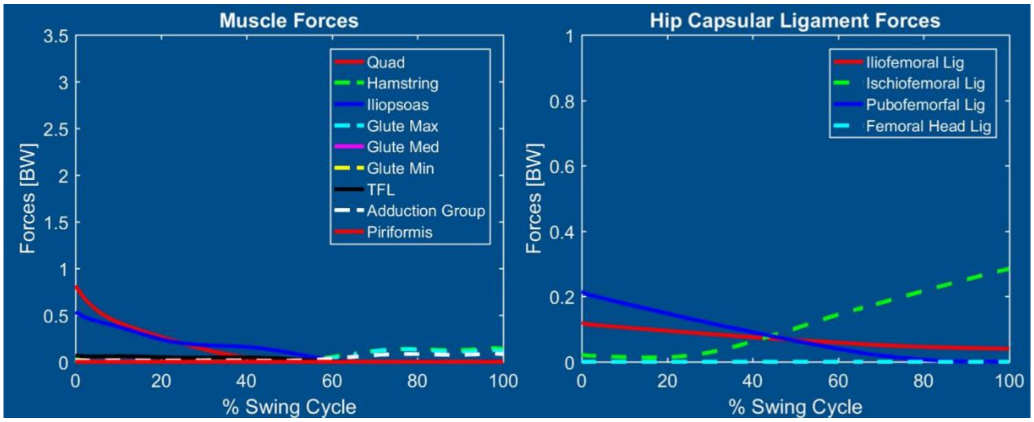

Figure 5-26: Hip muscle and ligament forces during swing phase when the acetabular cup is placed within the conic.

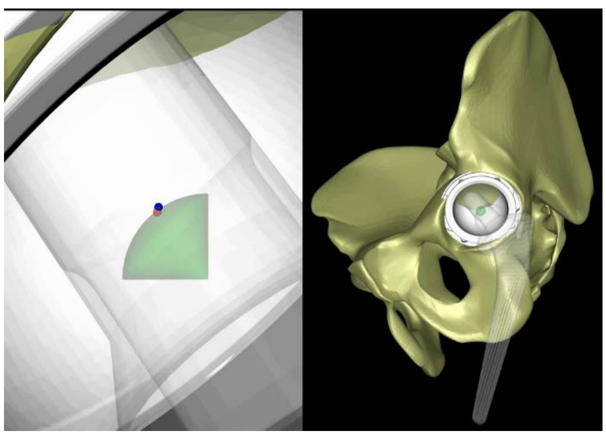

Figure 5-27: The placement of the acetabular cup at the rim of the conic. The acetabular cup center (red dot) is placed at the rim of the conic. The conic is represented in green, and its center is fixed at the anatomical hip center. The dark blue dot represents the femoral component head center.

The contact mechanics and muscle/ligament forces in stance phase are shown in Figure 5-28, Figure 5-29, and Figure 5-30, respectively. The contact mechanics and muscle/ligament forces in swing phase are shown Figure 5-31, Figure 5-32, and Figure 5-33, respectively.

As the acetabular was re-positioned outside of the optimal conic, there appeared to be severe edge loading during stance phase with the magnitude of hip separation up to 2.5 mm and severe hip separation during swing phase with the magnitude of hip separation up to 3.5 mm. Also, in both swing and stance phase, the cup stress increased significantly, resulting in an increased risk of wear leading to early complications. This find especially occurred during swing phase, where the femoral head moved back from the maximum of separation into contact with the acetabular cup, generating a squeaking sound. The placement of the acetabular cup outside the optimal conic is shown in Figure 5-34.

The contact mechanics and muscle/ligament forces in stance phase are shown in Figure 5-35, Figure 5-36, and Figure 5-37, respectively. The contact mechanics and muscle/ligament forces in swing phase are shown in Figure 5-38, Figure 5-39, and Figure 5-40, respectively.

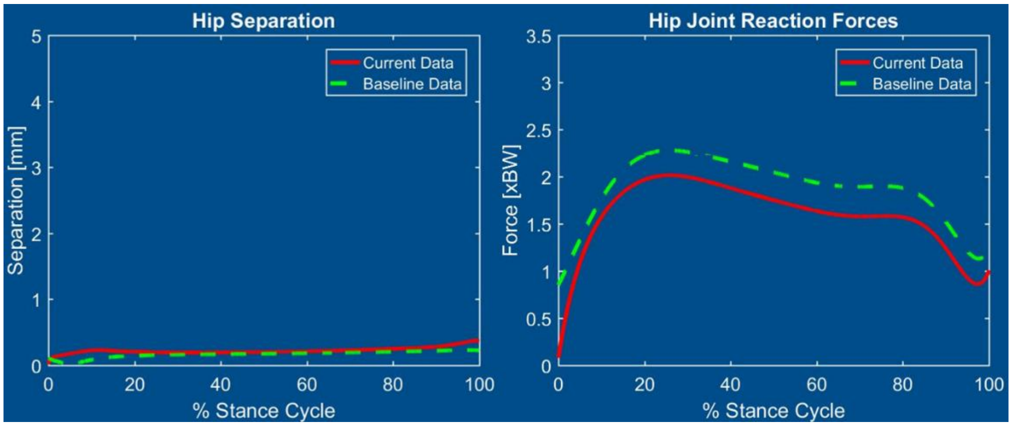

Figure 5-28: Hip separation and hip forces during stance phase when the acetabular cup is placed at the rim of the conic.

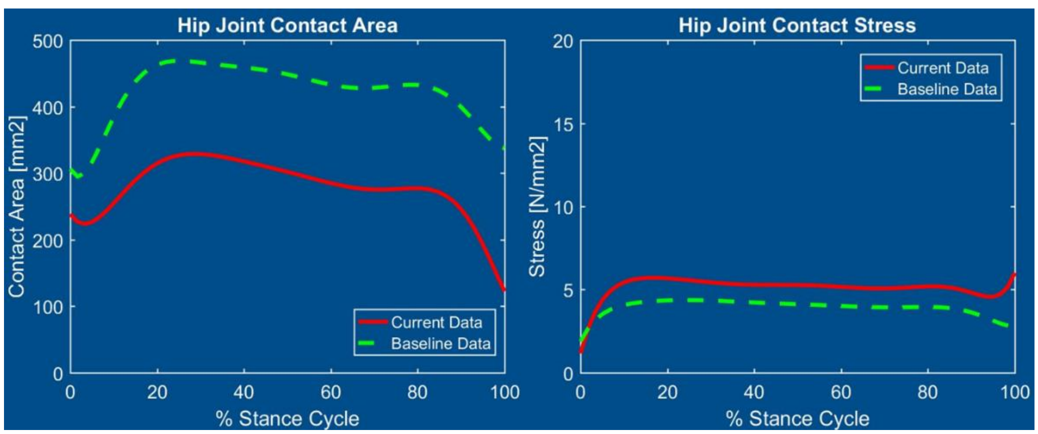

Figure 5-29: Contact area and contact stress at the hip joint during stance phase when the acetabular cup is placed at the rim of the conic.

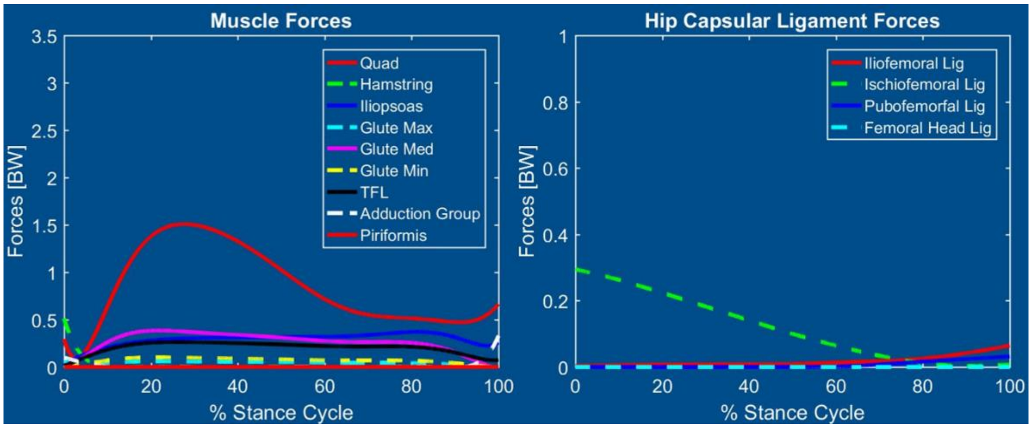

Figure 5-30: Hip muscle and ligament forces during stance phase when the acetabular cup is placed at the rim of the conic.

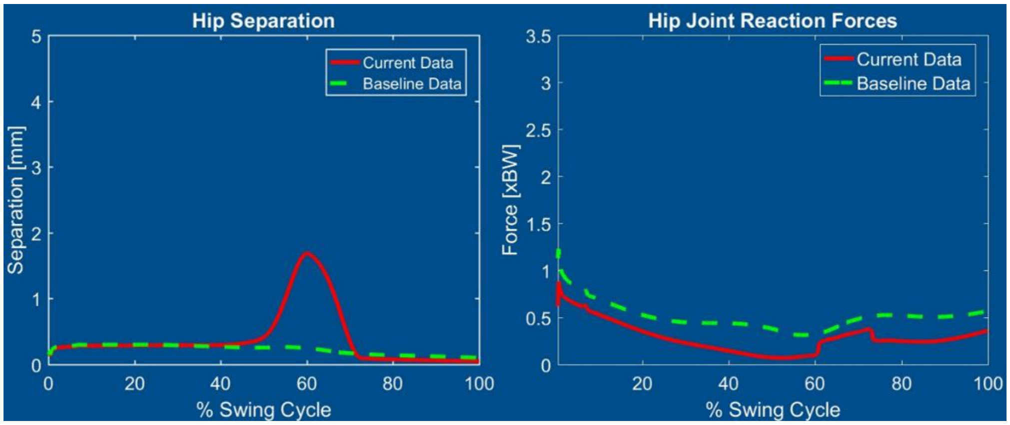

Figure 5-31: Hip separation and hip forces during swing phase when the acetabular cup is placed at the rim of the conic.

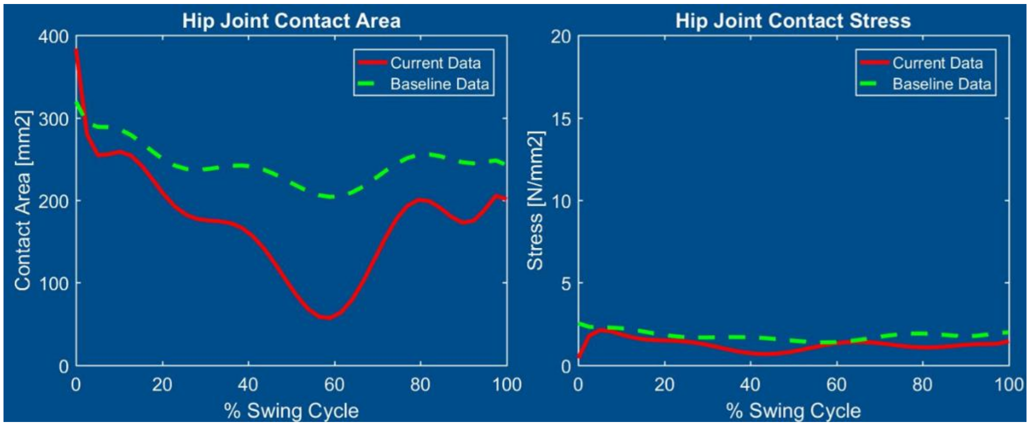

Figure 5-32: Contact area and contact stress at the hip joint during swing phase when the acetabular cup is placed at the rim of the conic.

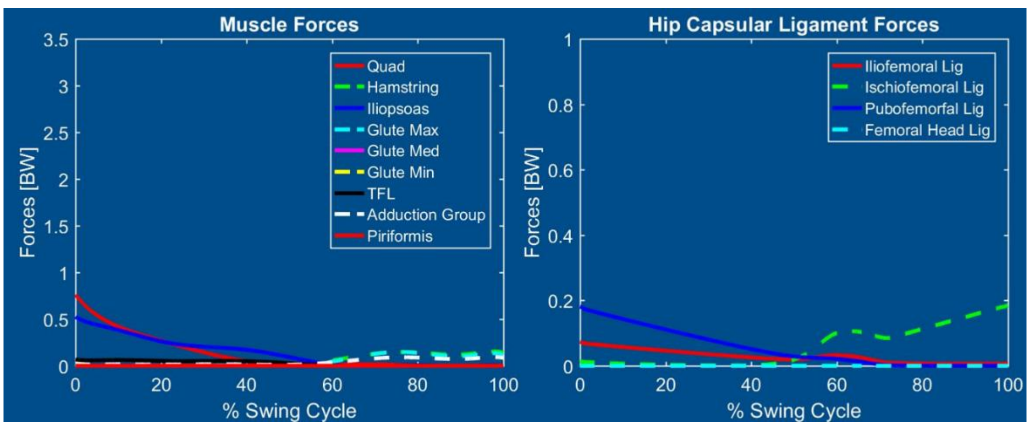

Figure 5-33: Hip muscle and ligaments forces during swing phase when the acetabular cup is placed at the rim of the conic.

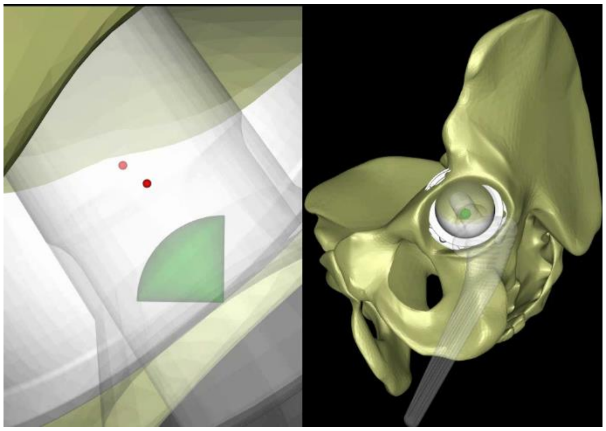

Figure 5-34: The placement of the acetabular cup outside the conic. The acetabular cup center (red dot) is placed outside the conic. The conic is represented in green, and its center is fixed at the anatomical hip center. The pink dot represents the femoral component head center.

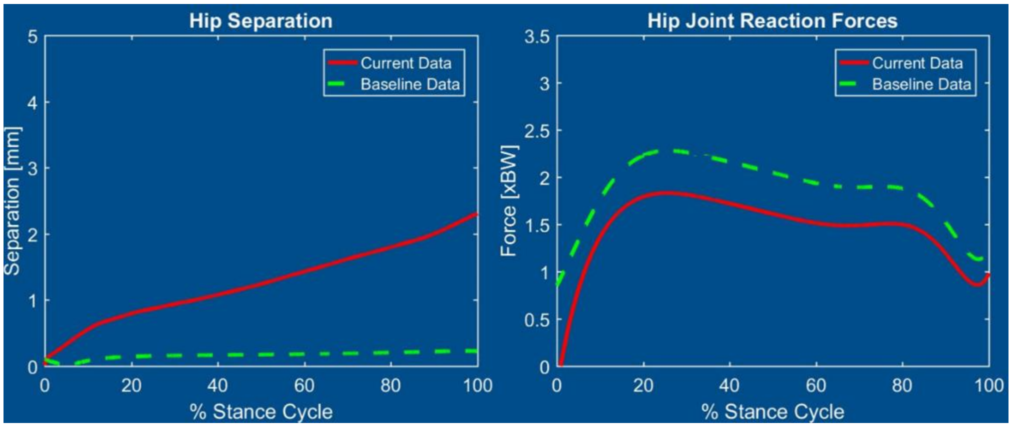

Figure 5-35: Hip separation and hip forces during stance phase when the acetabular cup is placed outside the conic.

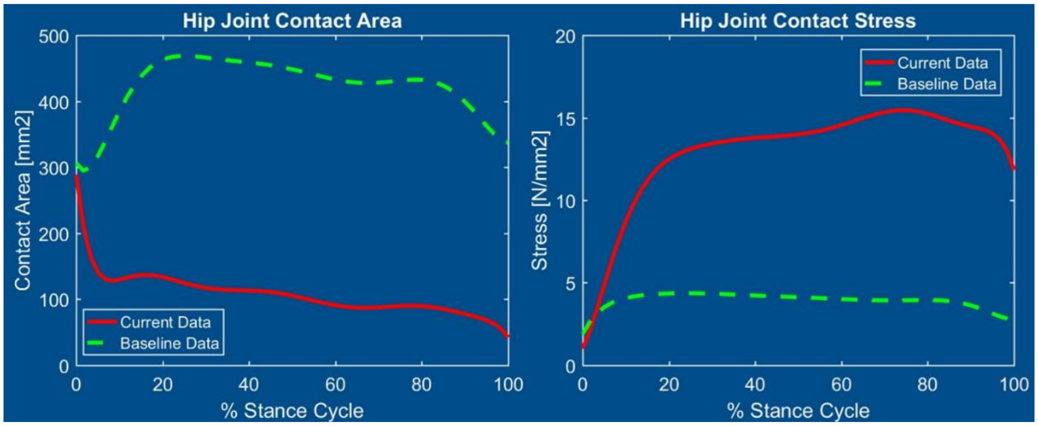

Figure 5-36: Contact area and contact stress at the hip joint during stance phase when the acetabular cup is placed outside the conic.

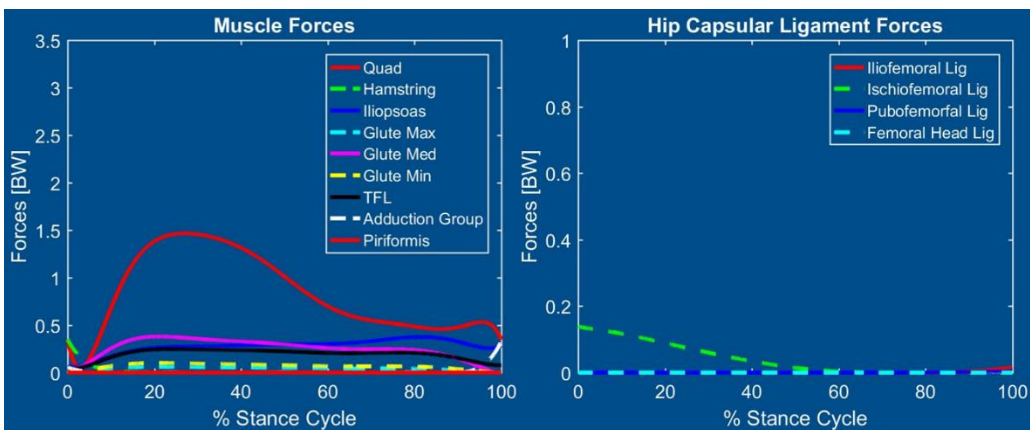

Figure 5-37 Hip muscle and ligament forces during stance phase when the acetabular cup is placed outside the conic.

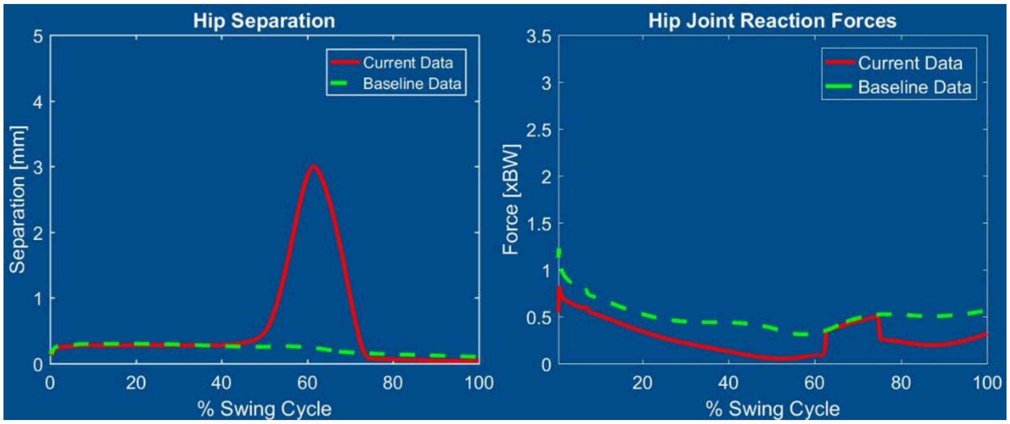

Figure 5-38: Hip separation and hip forces during swing phase when the acetabular cup is placed outside the conic.

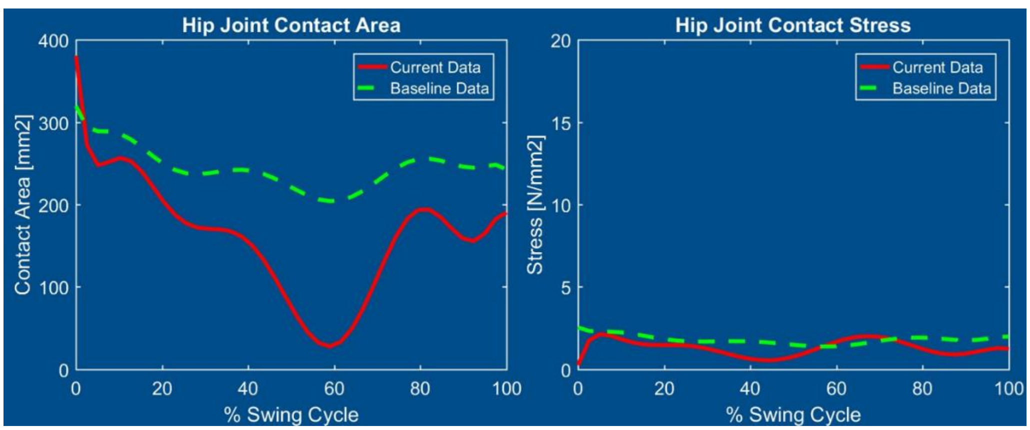

Figure 5-39: Contact area and contact stress at the hip joint during swing phase when the acetabular cup is placed outside the conic.

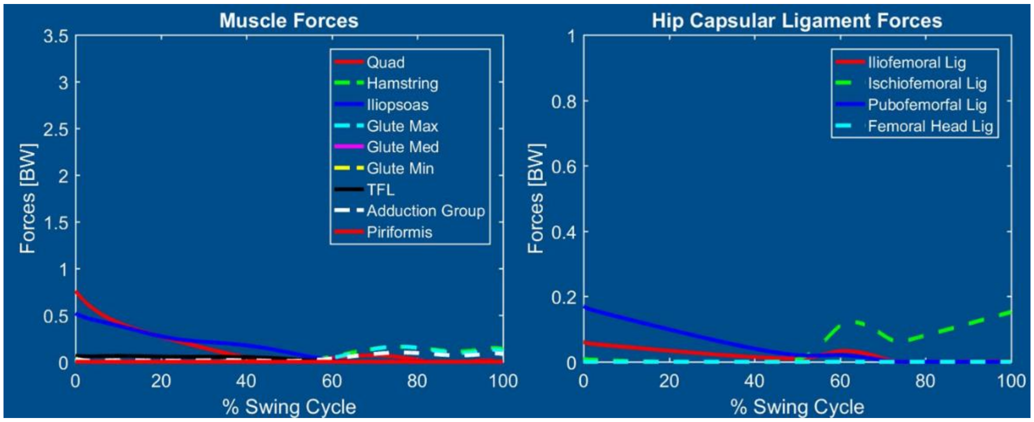

Figure 5-40: Hip muscle and ligament forces during swing phase when the acetabular cup is placed outside the conic.

5.2.2 Leg Length Discrepancy Analysis

Leg length discrepancy (LLD) has been proven to be one of the most concerning issues associated with THA. Long-term follow-up studies have documented that the presence of LLD had a direct correlation with patient dissatisfaction, dislocation, back pain, and early complications. Several researchers have sought to minimize limb length discrepancy based on pre-operative radiological templating or intra-operative measurements. While it is often a common occurrence in clinical practice to compensate for LLD intra-operatively, the center of rotation of the hip joint has been unintentionally changed due to excessive reaming. Although some surgeons do intentionally ream up to 10 mm in the medial direction so that they can get better cup fixation. Therefore, the clinical importance of LLD is still difficult to solve and remains a concern for clinicians. In this dissertation, an extensive analysis has been conducted to exam the effects of leg length discrepancy using the mathematical model in both stance and swing phase of gait.

During swing phase, it was determined that shortening the leg lead to the loosening of the hip capsular ligaments, with momentum of the lower leg increasing to a level where the ligaments could not properly constrain to the hip, and thus, leading to the femoral head sliding from within the acetabular cup (Figure 5-41). This pistoning motion led to decrease contact area and increase contact stress within the cup. Hip separation and contact mechanics when the leg length was shortened are shown in Figure 5-41 and Figure 5-42, respectively. Hip capsular ligament and quadricep muscle forces when the leg length was shortened are shown in Figure 5-43. Muscle forces at the hip when decreasing leg length are shown in Figure 5-44, Figure 5-45, and Figure 5-46.

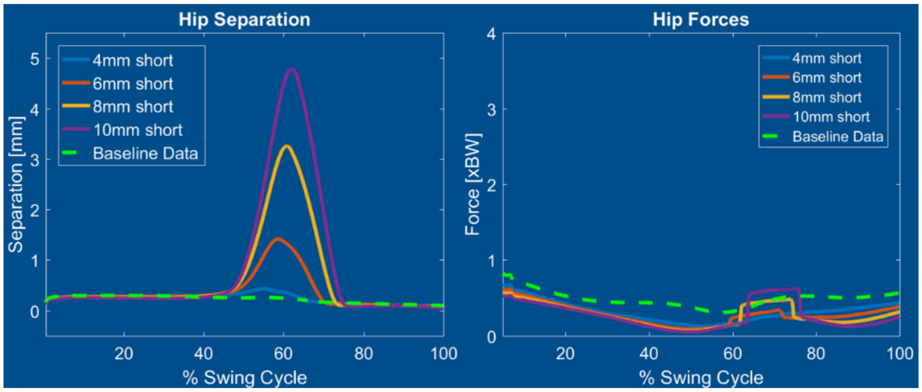

Figure 5-41: Comparison of hip separations and hip forces during swing phase when the leg length is shortened.

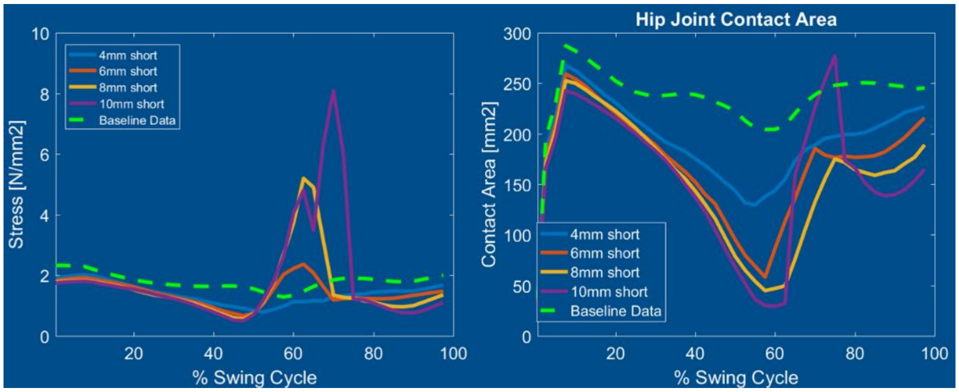

Figure 5-42: Comparison of hip contact stresses and contact areas during swing phase when the leg length is shortened.

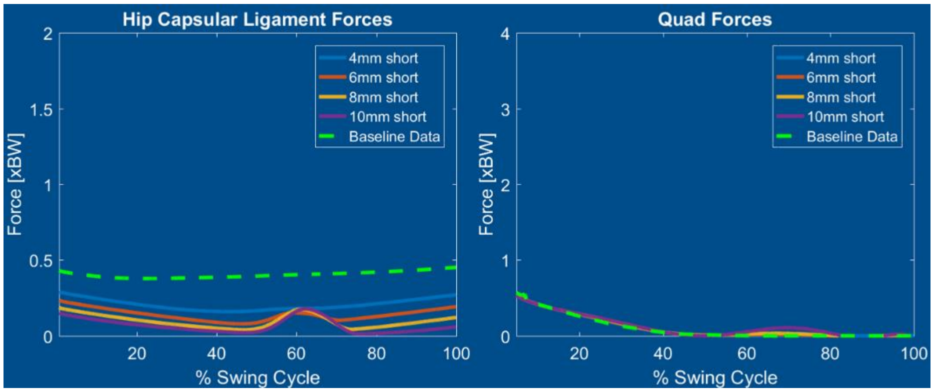

Figure 5-43: Comparison of hip capsular ligament and quadricep muscle forces during swing phase when the leg length is shortened.

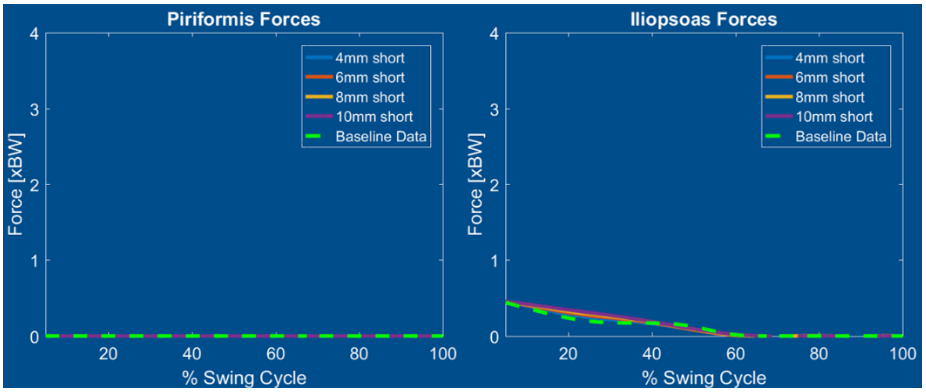

Figure 5-44: Comparison of piriformis and iliopsoas muscle forces during swing phase when the leg length is shortened.

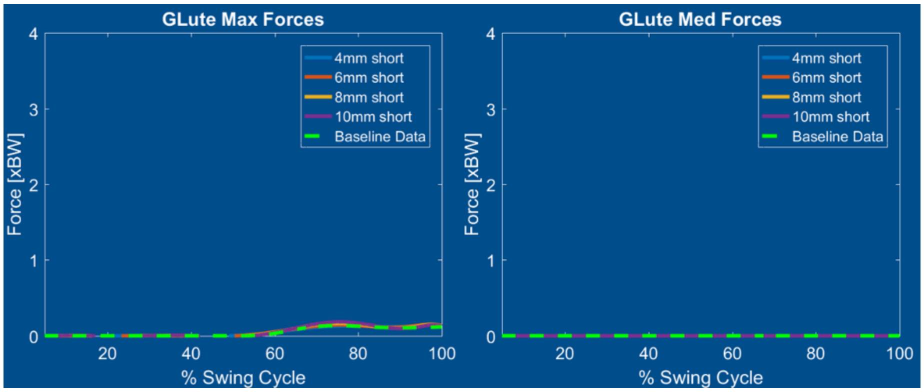

Figure 5-45: Comparison of gluteus maximus and gluteus medius muscle forces during swing phase when the leg length is shortened.

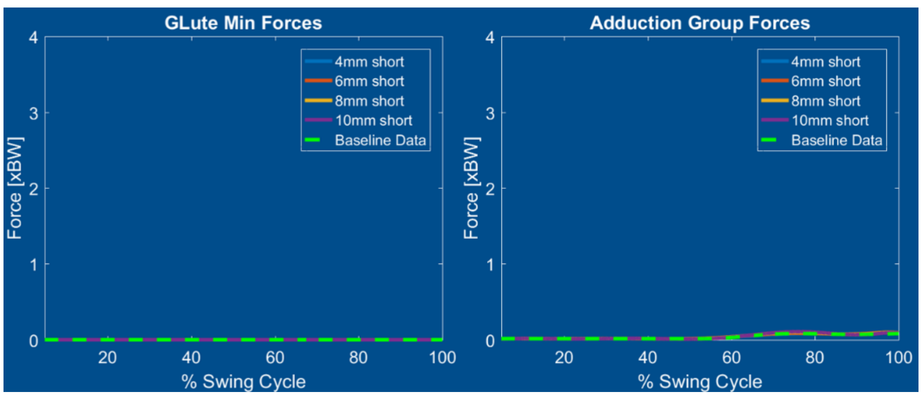

Figure 5-46: Comparison of gluteus minimus and adduction muscle group forces during swing phase when the leg length is shortened.

Lengthening the leg did not yield femoral head sliding, but it did increase joint tension and contact stress. A tight hip may be an influential factor leading to back pain and poor patient satisfaction. Hip separation and contact mechanics when the leg length was lengthened are shown in Figure 5-47 and Figure 5-48, respectively. Hip capsular ligament and quadricep muscle forces when the leg length was lengthened are shown in Figure 5-49. Muscle forces at the hip when decreasing leg length are shown in Figure 5-50, Figure 5-51, and Figure 5-52.

During stance phase, it was determined that shortening the leg lead to femoral head sliding and thus leading to decreased contact area and an increase in contact stress. Hip separation and contact mechanics when the leg length was shortened are shown in Figure 5-53 and Figure 5-54, respectively. Hip capsular ligament and quadricep muscle forces when the leg length was shortened is shown in Figure 5-55. Muscle forces at the hip when the leg length was shortened are shown in Figure 5-56, Figure 5-57, and Figure 5-58.

Lengthening the leg caused an increase in capsular ligaments tension leading to higher stress in the hip joint. Hip separation and contact mechanics when the leg length was lengthened are shown in Figure 5-59 and Figure 5-60, respectively. Hip capsular ligament and quadricep muscle forces when the leg length as lengthened is shown in Figure 5-61. Muscle forces at the hip when the leg length was lengthened are shown in Figure 5-62, Figure 5-63, and Figure 5-64.

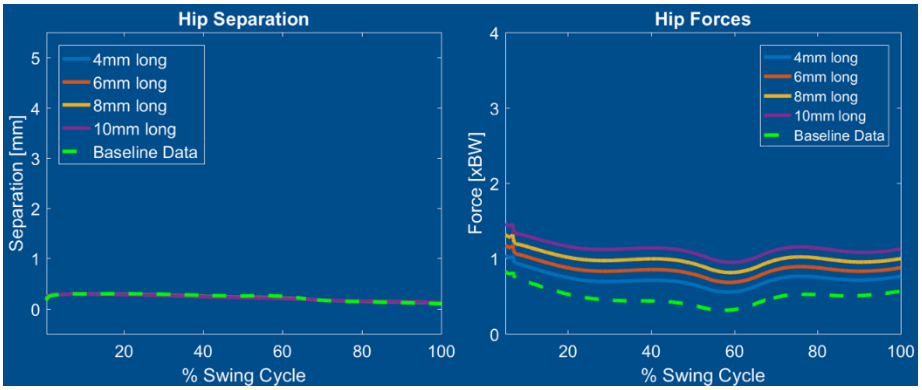

Figure 5-47: Comparison of hip separations and hip forces during swing phase when the leg length is lengthened.

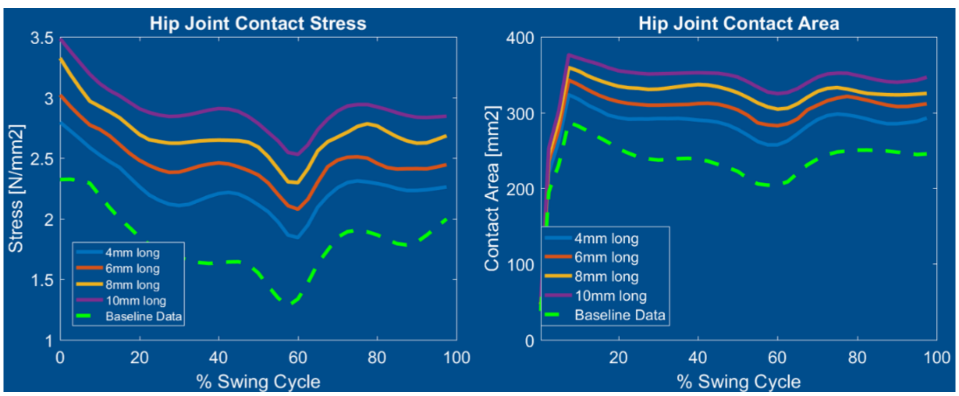

Figure 5-48: Comparison of hip contact stresses and contact areas during swing phase when the leg length is lengthened.

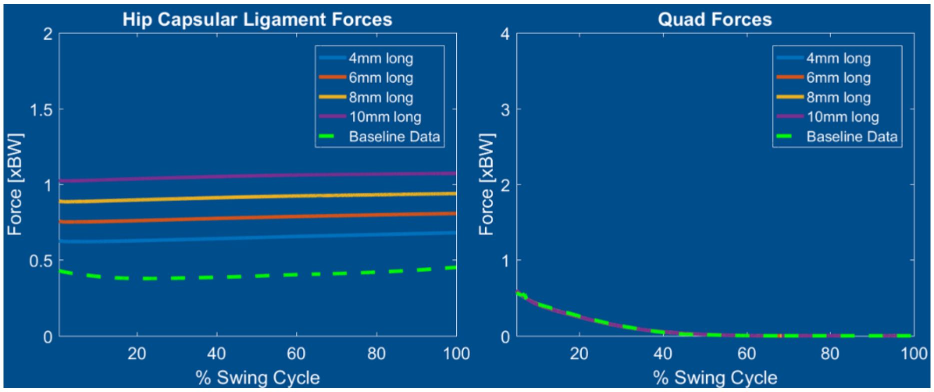

Figure 5-49: Comparison of hip capsular ligament and quadricep muscle forces during swing phase when the leg length is lengthened.

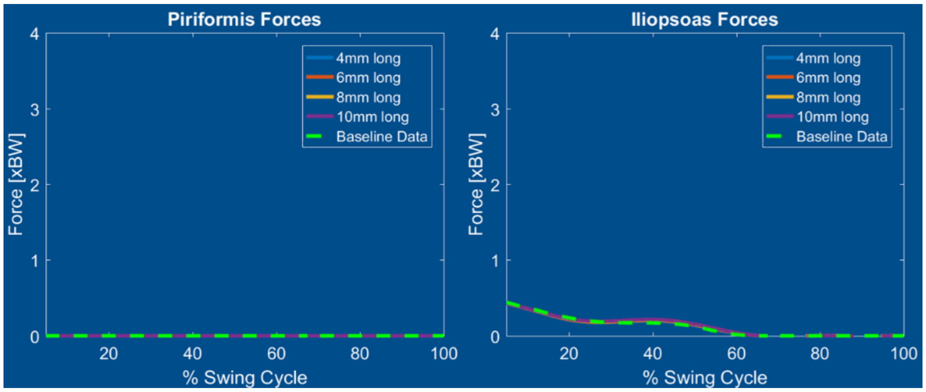

Figure 5-50: Comparison of piriformis and iliopsoas muscle forces during swing phase when the leg length is lengthened.

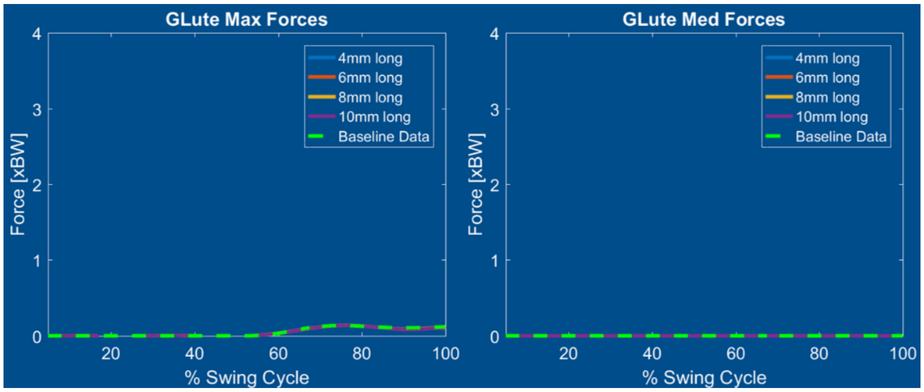

Figure 5-51: Comparison of gluteus maximus and gluteus medius muscle forces during swing phase when the leg length is lengthened.

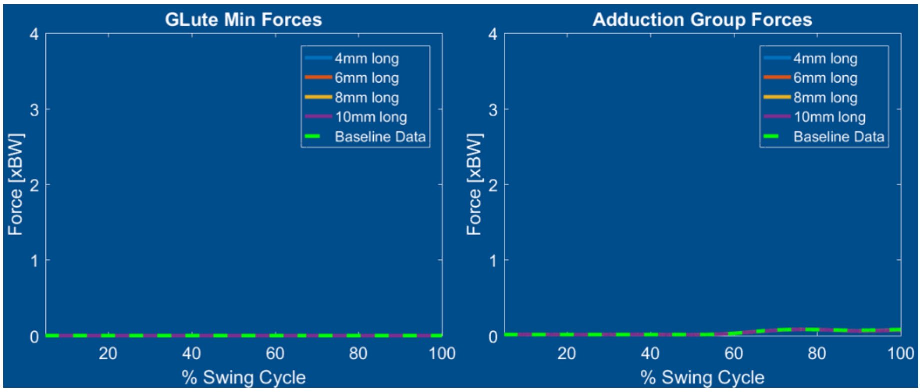

Figure 5-52: Comparison of gluteus minimus and adduction muscle group forces during swing phase when the leg length is lengthened.

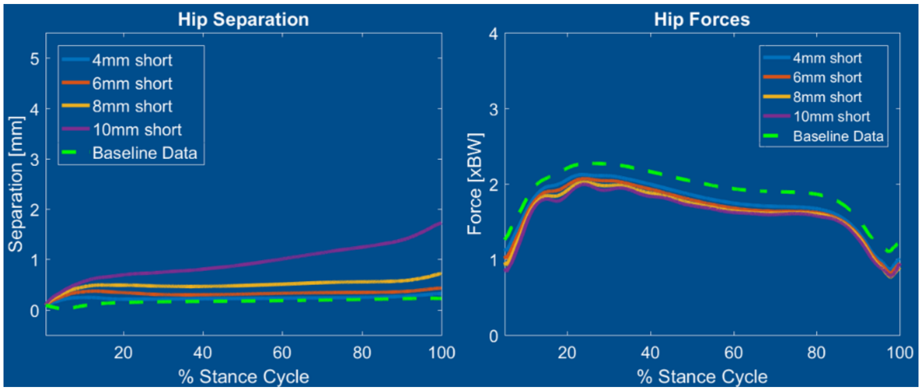

Figure 5-53: Comparison of hip separations and hip forces during stance phase when the leg length is shortened.

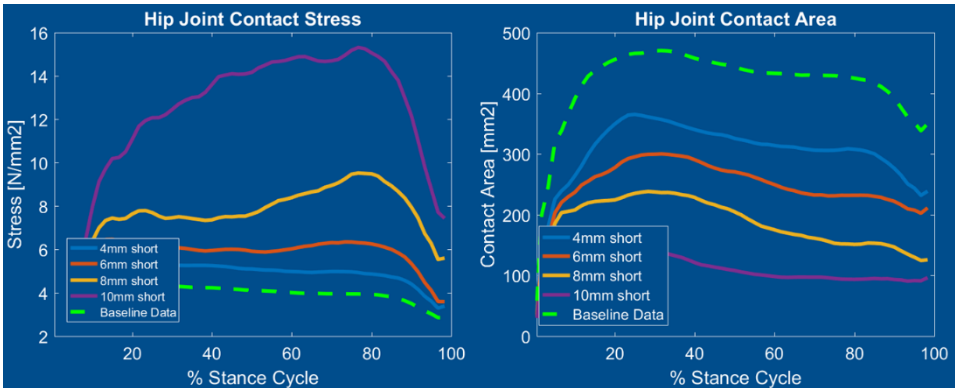

Figure 5-54: Comparison of hip contact stresses and contact areas during stance phase when the leg length is shortened.

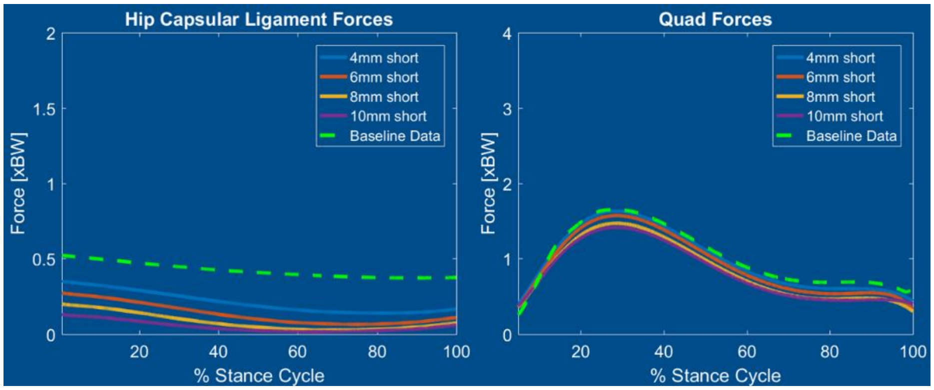

Figure 5-55: Comparison of hip capsular ligament and quadricep muscle forces during stance phase when the leg length is shortened.

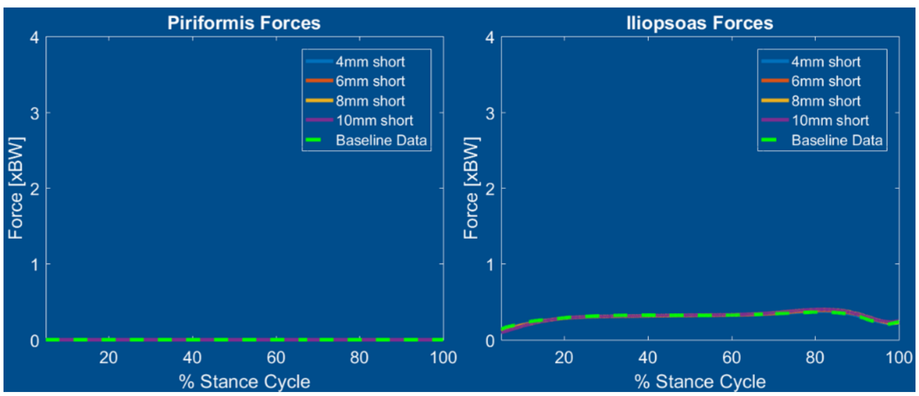

Figure 5-56: Comparison of piriformis and iliopsoas muscle forces during stance phase when the leg length is shortened.

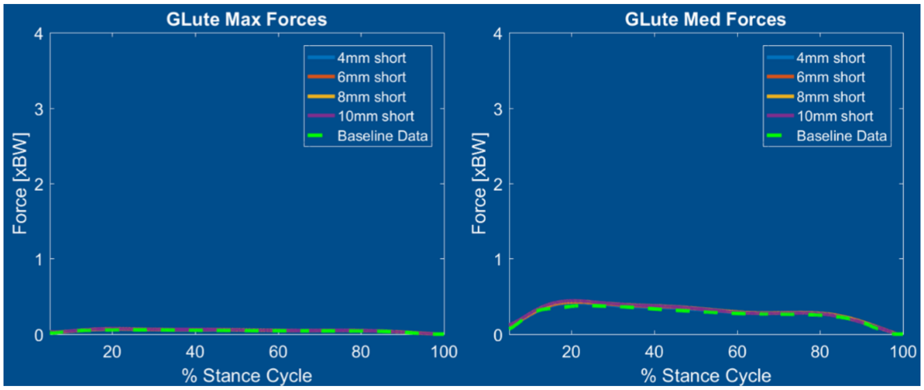

Figure 5-57: Comparison of gluteus maximus and gluteus medius muscle forces during stance phase when the leg length is shortened.

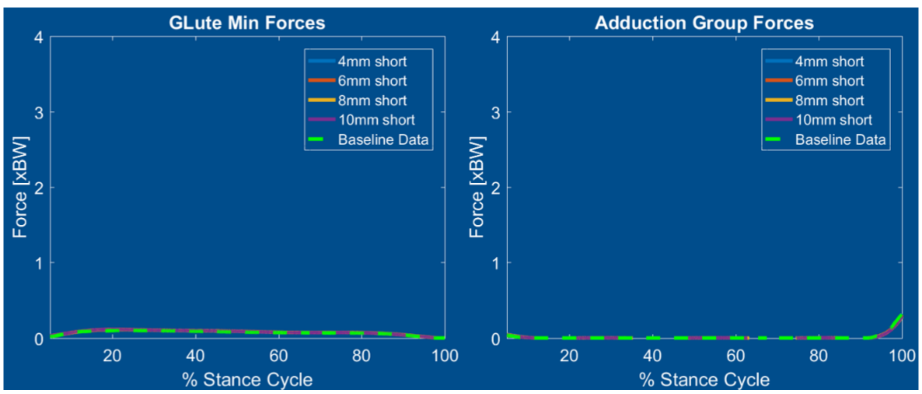

Figure 5-58: Comparison of gluteus minimus and adduction muscle group forces during stance phase when the leg length is shortened.

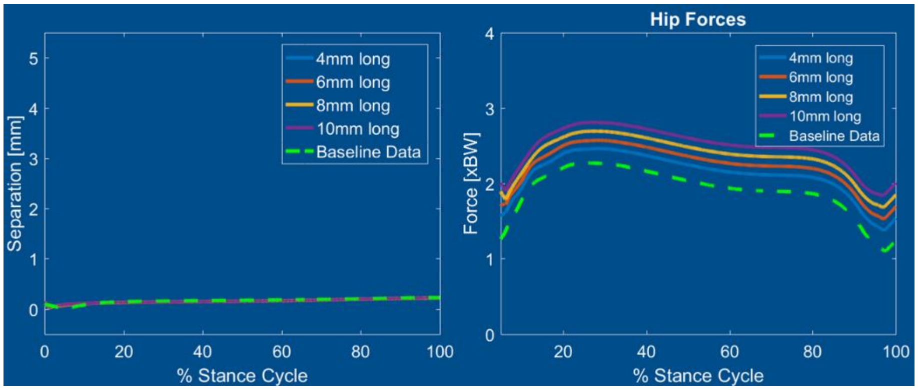

Figure 5-59: Comparison of hip separations and hip forces during stance phase when the leg length is lengthened.

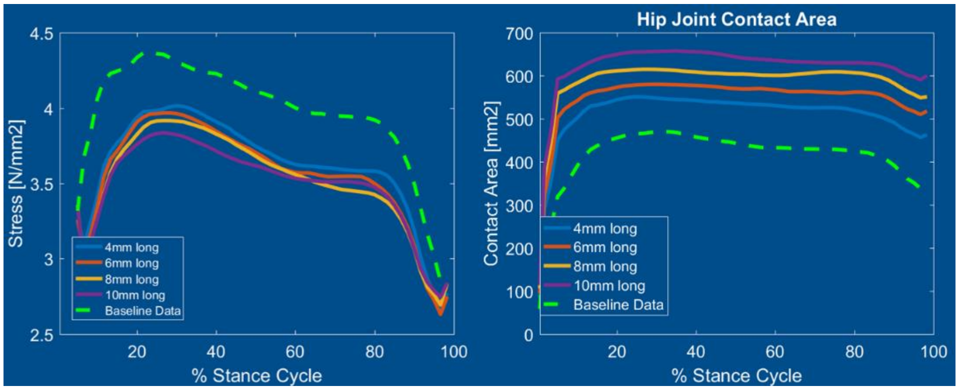

Figure 5-60: Comparison of hip contact stresses and contact areas during stance phase when the leg length is lengthened.

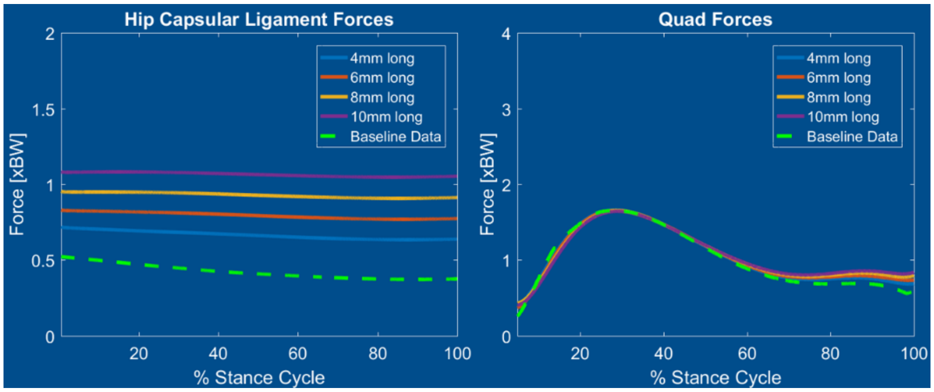

Figure 5-61: Comparison of hip capsular ligament and quadricep muscle forces during stance phase when the leg length is lengthened.

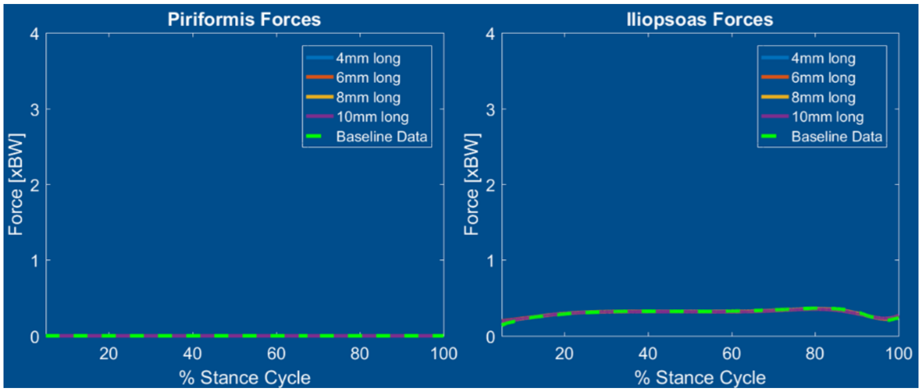

Figure 5-62: Comparison of piriformis and iliopsoas muscle forces during stance phase when the leg length is lengthened.

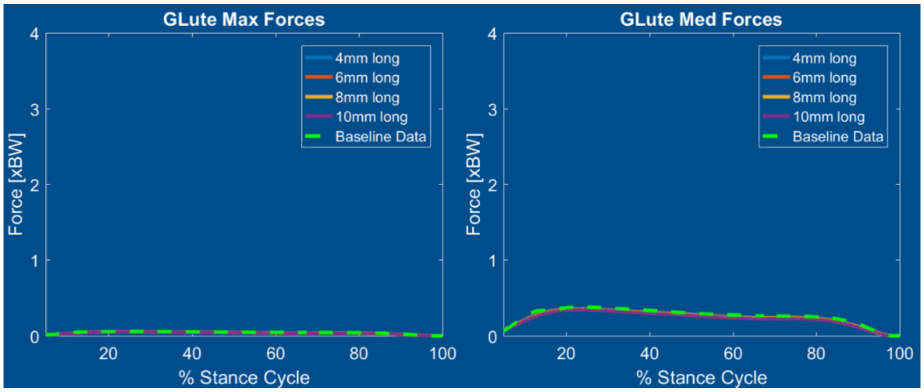

Figure 5-63: Comparison of gluteus maximus and gluteus medius muscle forces during stance phase when the leg length is lengthened.

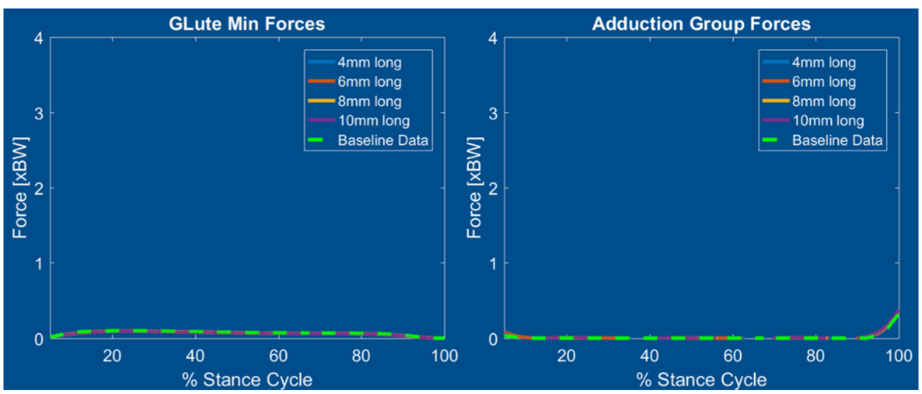

Figure 5-64: Comparison of gluteus minimus and adduction muscle group forces during stance phase when the leg length is lengthened.

CHAPTER 6: VALIDATION

6.1 FEMORAL STEM AND ACETABULAR CUP SIZING

The automated total hip arthroplasty sizing prediction algorithm is validated using the component choice made by the surgeon for each patient. As described in the previous section, four of the eight subjects participating in this study, who were diagnosed severe osteoarthritis, were assessed following a total hip arthroplasty surgery performed by a single surgeon using the Corail stem and Pinnacle acetabular hip system. Please keep in mind that the implant sizing, predicted by the proposed algorithm, is based on available implant CAD models in our database. If there are more implant CAD models, the proposed algorithm may generate more accurate results. In four hip arthroplasty components (femoral stem, head, liner, shell), the femoral stem is the only component that the proposed algorithm predicted its size. Sizes of the other three components were estimated based on a rule of thumb in the orthopaedic surgeon community [81]. The comparison of the femoral stem predicted by the computer algorithm and the surgeon is shown in Table 6-1.

As represented in Table 6-1, the predicted femoral stem sizes are highly consistent with the surgeon's choice. The only difference is that two in four subjects the surgeon chose the coxa vara stems (KLA stems). As we do not have coxa vara stems in our database, the proposed algorithm was looking for the closest available femoral stem. It may be the reason leading to the difference. However, the femoral morphologies shown in Table 5-1 confirmed that the surgeon's choices of coxa vara stems were reasonable and concise to the measured results. Specifically, the neck shaft angle of patient two and eight calculated by the proposed algorithm were 131 and 115 degrees, respectively.

Table 6-1: Comparison of the femoral stem size predicted by the proposed algorithm and the surgeon's selection.

	Stem (Prediction)	Stem (Surgeon Selection)
Patient 2	12 High Offset	KLA 12 High Offset
Patient 3	11 Standard	11 Standard
Patient 5	12 High Offset	KLA Size 12 High Offset
Patient 8	12 Standard	12 Standard

As depicted in Figure 6-1 the side by side comparison of the femoral stem predicted by the proposed algorithm and the surgeon's selection for patient 5. The predicted femoral stem head, acetabular shell, and acetabular liner were compared to the surgeon's choice and are shown in Table 6-2, Table 6-3, and Table 6-4, respectively.

As shown in above tables, the predicted sizes of the acetabular shell, liner, and femoral stem head are larger than the surgeon's selections. Please keep in mind that the sizes of the femoral stem head and the acetabular liner are dependent of the acetabular shell size, while the size of the acetabular shell was approximated by the following formula [81]:

$$\text{Size of the Shell} = \text{Femoral Head Diameter} + 8\ \pm 2\ (\text{mm})$$

The size of the acetabular shell in Table 6-3 was estimated using the upper bound of the above equation and therefore looked larger than the surgeon's choice. If the lower bound is used, Table 6-3 is revised as follow. As shown in Table 6-5, the predicted sizes of the acetabular shell are plus/minus one size the surgeon's choice. This shows the consistency and reliability of the predicted algorithm.

6.2 FEMORAL STEM AND ACETABULAR CUP PLACEMENT

As stated in Chapter 5, section 1, only two subjects returned to participate in the post-operative fluoroscopy study. Fluoroscopic videos of these two subjects were recorded and analyzed using a 3D to 2D registration technique [99]. As shown in Figure 6-2 the positions of hip implant components and bone models are obtained from the above-mentioned 3D to 2D registration technique. Through this analysis, the positions of the hip

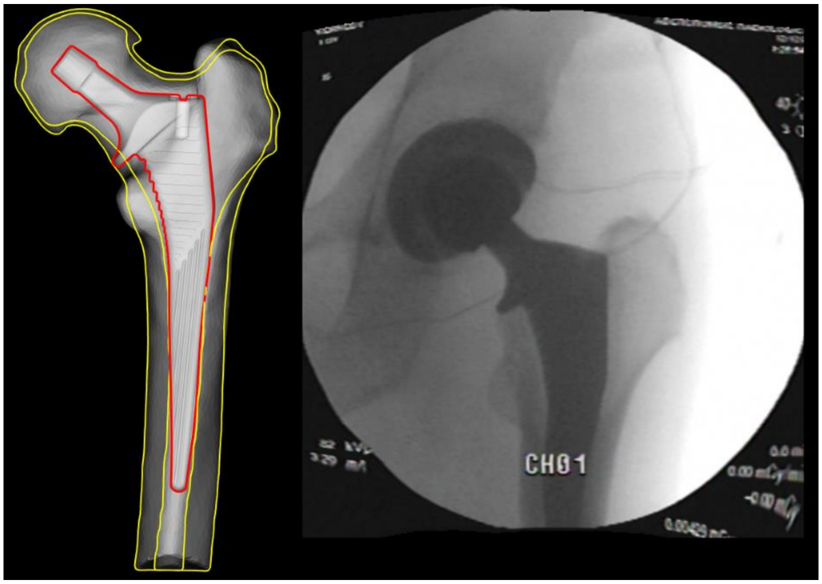

Figure 6-1: Comparison of the femoral stem predicted by the proposed algorithm (left image) and the surgeon's selection (right image) for patient 5.

Table 6-2: Comparison of the predicted femoral stem head and the surgeon's choice.

	Head (Prediction)	Head (Surgeon Selection)
Patient 2	+1, 36 mm, 12/14 taper	+1, 32mm, 12/14 taper
Patient 3	+5, 32 mm, 12/14 taper	+9, 32mm, 12/14 taper
Patient 5	+5, 36 mm, 12/14 taper	+1, 32mm, 12/14 taper
Patient 8	+5, 36 mm, 12/14 taper	+5.0, 32mm, 12/14 taper

Table 6-3: Comparison of the predicted acetabular shell and the surgeon's choice.

	Shell (Prediction)	Shell (Surgeon Selection)
Patient 2	58 mm OD	52 mm OD
Patient 3	54 mm OD	52 mm OD
Patient 5	60 mm OD	54 mm OD
Patient 8	56 mm OD	52 mm OD

Table 6-4: Comparison of the predicted acetabular liner and the surgeon's choice.

	Liner (Prediction)	Liner (Surgeon Selection)
Patient 2	Neutral 36 mm ID, 58 mm OD	Neutral 32mm ID 52mm OD
Patient 3	Neutral 32 mm ID, 54 mm OD	Neutral 32mm ID 52mm OD
Patient 5	Neutral 36 mm ID, 60 mm OD	Neutral 32mm ID 54mm OD
Patient 8	Neutral 36 mm ID, 56 mm OD	Neutral 32mm ID 52mm OD

Table 6-5: Revised sizes of the acetabular shell using the lower bound.

	Shell (Prediction)	Shell (Surgeon Selection)
Patient 2	54 mm OD	52 mm OD
Patient 3	50 mm OD	52 mm OD
Patient 5	56 mm OD	54 mm OD
Patient 8	52 mm OD	52 mm OD

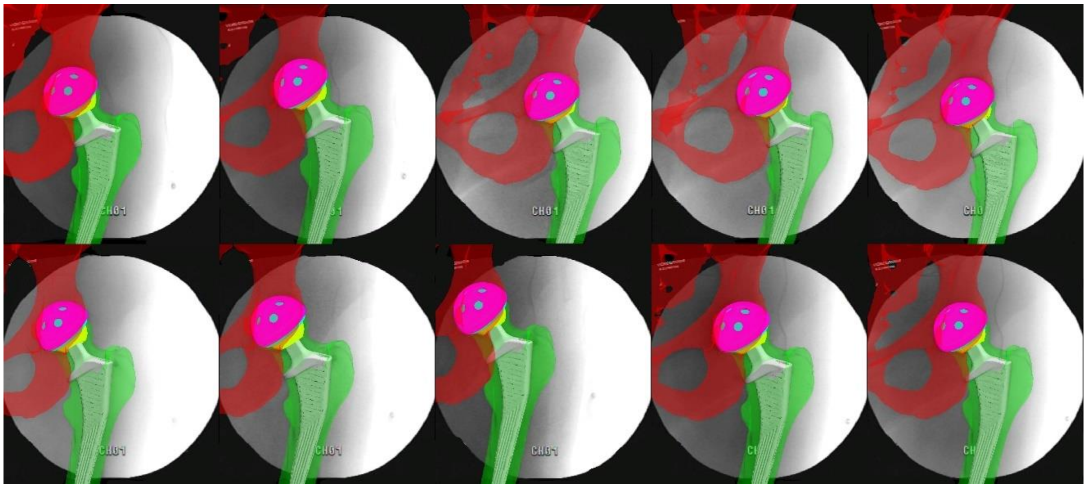

Figure 6-2: A 3D to 2D registration technique is used to obtain the position of hip implants and bone models.

implant components for each subject were obtained and compared to the predicted positions of the same subject by the proposed program.

The comparisons of the acetabular cup version, inclination, and femoral stem version obtained from the proposed program and fluoroscopy analysis are represented in Table 6-6, Table 6-7, and Table 6-8 , respectively.

As represented in above tables, the predicted acetabular version differs 13 degrees for patient 2 and 7 degrees for patient 5, while the predicted acetabular inclinations are close to the measured inclination from fluoroscopy. The predicted femora stem version differs 8 degrees for patient 2 and 4 degrees for patient 5. Such differences can be explained because of the difference in the criteria of implant placement between the surgeon and the proposed algorithm. While the proposed algorithm attempted to restore anatomical positions of the acetabular cup and the femoral stem, the surgeon's criteria vary compared to the criteria set in our algorithm. This algorithm can be personalized for each such, using similar criteria used by the surgeon. Therefore, the future work for the proposed algorithm should have the capability to adapt to the objective criteria pertaining to the surgeon's experience and preference. As shown in Figure 6-3 the positions of the hip implant components obtained from the proposed algorithm and the X-ray image using a 3D to 2D registration technique are compared.

6.3 HIP SEPARATION

During the preoperative examination, surgeons can determine whether a patient, with a degenerative hip, is a candidate for THA. Although research studies have been conducted to investigate in vivo kinematics of degenerative hips using fluoroscopy,

Table 6-6: Comparison of the acetabular version obtained from the predicted program and fluoroscopy.

	Cup Version (Prediction)	Cup Version (Fluoroscopy)
Patient 2	19.83	33.03
Patient 5	17.61	24.57

Table 6-7: Comparison of the acetabular inclination obtained from the predicted program and fluoroscopy.

	Cup Inclination (Prediction)	Cup Inclination (Fluoroscopy)
Patient 2	49.7	45.19
Patient 5	53.17	41.77

Table 6-8: Comparison of the femoral stem version obtained from the predicted program and fluoroscopy.

	Stem Version (Prediction)	Stem Version (Fluoroscopy)
Patient 2	10.24	17.95
Patient 5	4.85	8.81

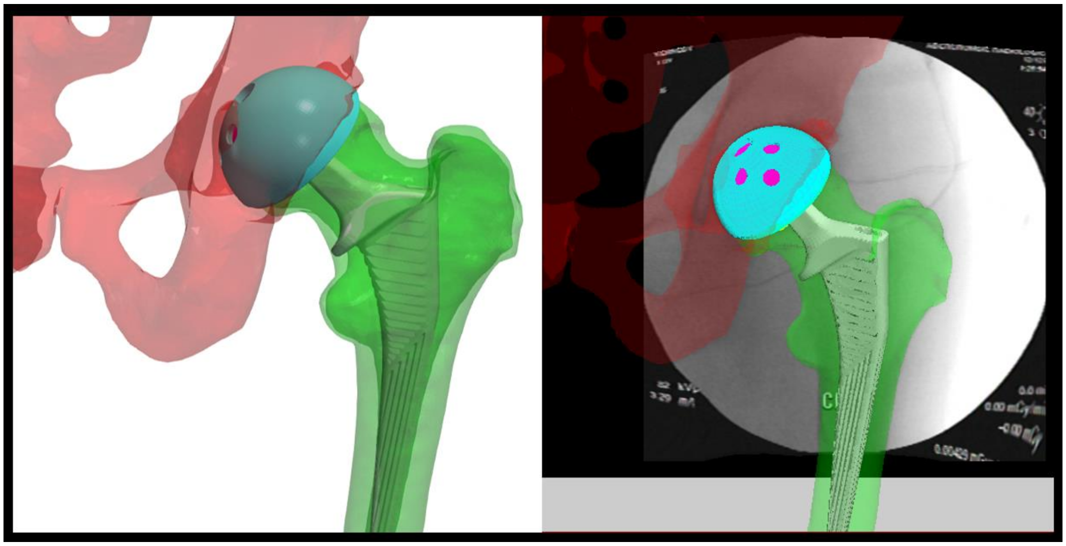

Figure 6-3: A side by side comparison of the implant positions obtained from the proposed algorithm (left image) and an X-ray image (right image).

surgeons do not have assessment tools they can use in their practice to further understand patient assessment. Ideally, if a surgeon could have a theoretical tool that efficiently allows for predictive post-operative assessment after virtual surgery and implantation, they would have a better understanding of joint conditions before surgery. The objectives of this section were (1) to use the forward solution hip model to theoretically predict the in vivo kinematics of a degenerative hip joint, gaining a better understanding joint conditions leading to THA and (2) compare the predicted kinematic patterns with those derived using fluoroscopy.

One subject was chosen for this validation who previously participated in a fluoroscopy study in Center for Musculoskeletal Research at the University of Tennessee Knoxville. This patient was diagnosed to be in the late state of osteoarthritis and was a candidate for total hip replacement. The patient was asked to perform gait under fluoroscopic surveillance. Kinematic analysis using a 3D to 2D registration method [99] revealed that the patient experienced hip separation where the femoral head slid within the acetabulum with the separation magnitude great than 1 mm [61].

During stance phase, kinematic patterns of degenerative hips were similar to the kinematic patterns of THA subjects with a malpositioned acetabular cup. Further evaluation revealed that if the cup was placed at a position other than its native, anatomical center, abnormal forces and torques acting within the joint lead to the femoral component sliding within the acetabular cup. It was hypothesized that in degenerative hips, similar to THA, the altered center of rotation is a leading influence of femoral head sliding. The comparison of hip separation during stance phase resulted from the fluoroscopy and the forward solution mathematical model is presented in Figure 6-4.

During swing phase, it was determined that this femoral head sliding is caused by hip capsular laxity, resulting in reduced joint tension. At the point of maximum velocity of the foot, the momentum of the lower leg becomes too great for capsule to properly constrain the hip, leading to the femoral component pistoning in the outward direction. The comparison of hip separation during swing phase resulted from the fluoroscopy and the forward solution mathematical model is presented in Figure 6-5.

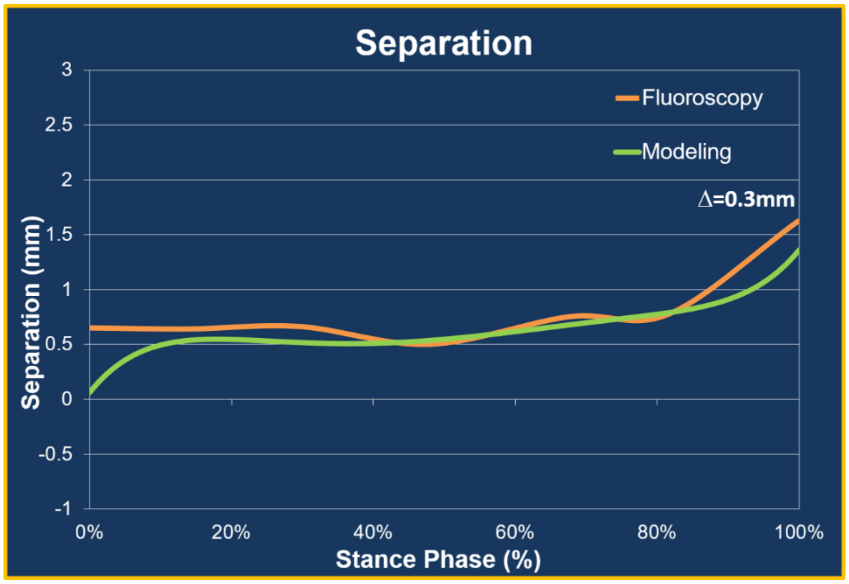

Figure 6-4: Hip separation obtained from fluoroscopic analysis and mathematical model during stance phase.

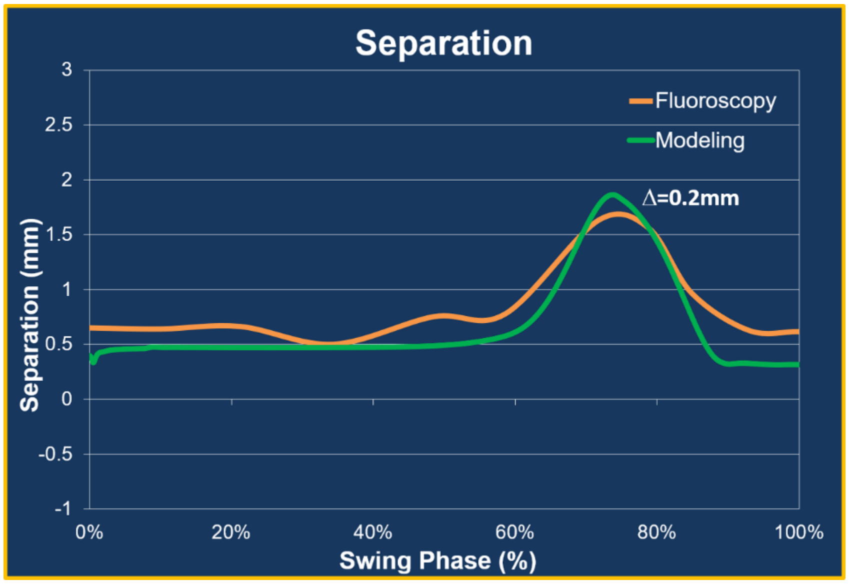

Figure 6-5: Hip separation obtained from fluoroscopic analysis and mathematical model during swing phase.

CHAPTER 7: CONTRIBUTIONS AND FUTURE WORK

7.1 CONTRIBUTIONS

In summary, this dissertation is focused on the development and implementation of a methodology to estimate the size of total hip arthroplasty for a given subject, a virtual surgery platform for both surgeons and engineers, and a methodology to predict post-operative surgical outcomes of a total hip arthroplasty surgery. In this endeavor, this dissertation involves considerable unique features, novelties, and contributions to the field of orthopaedic research. They include:

1. An automated procedure, within a forward solution mathematical model, that successfully predicts anatomical landmarks on a new bone model, given a known set of anatomical landmarks on a template bone model.
2. A new approach to measure the proximal femoral morphology, within a forward solution mathematical model, that has been proven to work efficiently for both normal and abnormal femoral bone geometries.
3. A novel concept of the proximal femoral canal morphology, within a forward solution mathematical model, that is used to estimate the size of total hip arthroplasty for a given subject, and provide meaningful information pertaining to the geometry of the proximal femoral canal.
4. A novel concept of the femoral stem morphology, within a forward solution mathematical model, that provides essential information for a better understanding of the geometry of a given femoral stem. This information also plays a crucial role in the process of estimating the femoral stem size.

5. A computer algorithm module, within a forward solution mathematical model, that is used to successfully predict the size of total hip arthroplasty of a particular subject.
6. A theoretical methodology for removing the femoral head, reaming the acetabulum, and broaching the femur in a virtual surgery procedure of total hip replacement that is part of a forward solution mathematical model.
7. Development and implementation of a virtual surgery platform that allows the User to better understand total hip arthroplasty surgery. This program can also work as a surgical training platform outside the Operation Room (OR) that allows surgeons to gain hands-on experience and enhance skills in the OR by giving them instant feedback on each surgical procedure.
8. A substantial improvement in the accuracy and an expansion of the capability of the existing mathematical model of the hip joint. This can provide surgeons and engineers alike an instant feedback of post-operative surgical outcomes of a total hip replacement surgery.

7.2 LIMITATIONS AND FUTURE WORK

Although the dissertation work has been validated, there still exists limitations that we aim to improve in the future work.

First and foremost, the automated prediction of anatomical landmarks needs a good initial alignment of the new bone model and the template bone model. In this dissertation, a good initial alignment of two bone models, while defined, still is a qualitative definition. In the future work, we target to automate this process to reduce human variation error. We would like to incorporate more pre-defined knowledge, pertaining to the geometry and orientation, to have a better understanding of the new bone model.

Secondly, the measurement of the proximal femoral morphology and femoral stem morphology is greatly influenced by the orientation of the femoral canal and femoral stem. Even though multiple planes that are used to intersect the femoral canal and femoral stem are defined to be parallel to the transverse plane, the initial orientations of the proximal femoral canal and femoral stem still affect the geometries of the contours obtained from the intersection. Therefore, the future work should focus on how to obtain and define a good initial orientation of the femur and femoral stem.

Thirdly, in the virtual surgery platform, the saw used in the femoral head removal is simplified and the reamer and broach handles are not incorporated. This simplified saw does not affect the accuracy of a virtual surgery but does affect its appearance. In the future work we would like to work closely with the total hip implant manufactures to obtain realistic CAD models of these instruments.

Fourthly, as mentioned in the mathematical modeling section, obtaining a good set of initial parameters for the mathematical model is a time-consuming and challenging task. However, this step is extremely important to increase the accuracy of the entire mathematical model. Therefore, an important task in the future work should focus on developing an automated process to obtain these parameters. As suggested in this dissertation, an optimization procedure can be used to realize this expectation.

Fifthly, this mathematical model has successfully predicted post-operative outcomes, but is still limited in its capability to simulate different activities of daily living.

Even though multiple activities have been introduced and developed in this dissertation, they are primarily used for visualization purposes. In the future, we would like to realize this goal so that the mathematical model will have the powerful capability to simulate all common activities of daily life including gait, deep knee bend, rising from a chair, stair accent, stair decent, and crossing the leg.

Lastly, personalized implant design has not been introduced in a detailed manner in this dissertation. This dissertation, however, provides a foundation for the personalized implant design community. Since the proximal femoral morphology and femoral canal morphology have been automatically measured using the proposed morphology measurement algorithm, the implant design community can benefit from results of this work. In the future, we would like to cooperate with implant manufactures who are interested in personalized implant development to promote this idea in order to provide better health care treatment for patients who need a total hip arthroplasty.

LIST OF REFERENCES

[1] G. E. Lewinnek, J. Lewis, R. Tarr, C. Compere, and J. Zimmerman, “Dislocations after total hip-replacement arthroplasties,” *The Journal of bone and joint surgery. American volume*, vol. 60, no. 2, pp. 217-220, 1978.

[2] B. R. Deshpande, J. N. Katz, D. H. Solomon, E. H. Yelin, D. J. Hunter, S. P. Messier, L. G. Suter, and E. Losina, “Number of persons with symptomatic knee osteoarthritis in the US: impact of race and ethnicity, age, sex, and obesity,” *Arthritis care & research*, vol. 68, no. 12, pp. 1743-1750, 2016.

[3] R. Otten, and H. Picavet, “Trends in the number of knee and hip arthroplasties: considerably more knee and hip prostheses due to osteoarthritis in 2030,” *Nederlands tijdschrift voor geneeskunde*, vol. 154, pp. A1534-A1534, 2010.

[4] D. Symmons, C. Mathers, and B. Pfleger, “Global burden of osteoarthritis in the year 2000,” *Geneva: World Health Organization*, 2003.

[5] R. D. Komistek, T. R. Kane, M. Mahfouz, J. A. Ochoa, and D. A. Dennis, “Knee mechanics: a review of past and present techniques to determine in vivo loads,” *Journal of biomechanics*, vol. 38, no. 2, pp. 215-228, 2005.

[6] J. J. Callaghan, J. E. Templeton, S. S. Liu, D. R. Pedersen, D. D. Goetz, P. M. Sullivan, and R. C. Johnston, “Results of Charnley total hip arthroplasty at a minimum of thirty years: a concise follow-up of a previous report,” *JBJS*, vol. 86, no. 4, pp. 690-695, 2004.

[7] R. B. Bourne, B. M. Chesworth, A. M. Davis, N. N. Mahomed, and K. D. Charron, “Patient satisfaction after total knee arthroplasty: who is satisfied and who is not?,” *Clinical Orthopaedics and Related Research®*, vol. 468, no. 1, pp. 57-63, 2010.

[8] H. M. Kremers, D. R. Larson, C. S. Crowson, W. K. Kremers, R. E. Washington, C. A. Steiner, W. A. Jiranek, and D. J. Berry, “Prevalence of total hip and knee replacement in the United States,” *The Journal of bone and joint surgery. American volume*, vol. 97, no. 17, pp. 1386, 2015.

[9] E. W. Paxton, G. Cafri, S. Nemes, M. Lorimer, J. Kärrholm, H. Malchau, S. E. Graves, R. S. Namba, and O. Rolfson, “An international comparison of THA patients, implants, techniques, and survivorship in Sweden, Australia, and the United States,” *Acta Orthopaedica*, pp. 1-8, 2019.

[10] D. J. Berry, “Long-term follow-up studies of total hip arthroplasty,” *Orthopedics*, vol. 28, no. 8, pp. S879-S880, 2005.

[11] S. Greenfield, G. Apolone, B. J. McNeil, and P. D. Cleary, “The importance of co-existent disease in the occurrence of postoperative complications and one-year recovery in

patients undergoing total hip replacement. Comorbidity and outcomes after hip replacement," *Medical care,* vol. 31, no. 2, pp. 141-154, 1993.

[12] H. Lindahl, "Epidemiology of periprosthetic femur fracture around a total hip arthroplasty," *Injury,* vol. 38, no. 6, pp. 651-654, 2007.

[13] P. Sadoghi, M. Liebensteiner, M. Agreiter, A. Leithner, N. Böhler, and G. Labek, "Revision Surgery After Total Joint Arthroplasty: A Complication-Based Analysis Using Worldwide Arthroplasty Registers," *The Journal of Arthroplasty,* vol. 28, no. 8, pp. 1329-1332, 2013/09/01/, 2013.

[14] K. L. Corbett, E. Losina, A. A. Nti, J. J. Z. Prokopetz, and J. N. Katz, "Population-Based Rates of Revision of Primary Total Hip Arthroplasty: A Systematic Review," *PLOS ONE,* vol. 5, no. 10, pp. e13520, 2010.

[15] N. Sugano, K. Ohzono, T. Nishii, K. Haraguchi, T. Sakai, and T. Ochi, "Computed-tomography-based computer preoperative planning for total hip arthroplasty," *Computer Aided Surgery: Official Journal of the International Society for Computer Aided Surgery (ISCAS),* vol. 3, no. 6, pp. 320-324, 1998.

[16] S. Eggli, M. Pisan, and M. Müller, "The value of preoperative planning for total hip arthroplasty," *The Journal of bone and joint surgery. British volume,* vol. 80, no. 3, pp. 382-390, 1998.

[17] E. H. Miashiro, E. N. Fujiki, E. N. Yamaguchi, T. Chikude, L. H. S. Rodrigues, G. M. Fontes, and F. B. Rosa, "Preoperative planning of primary total hip arthroplasty using conventional radiographs," *Revista Brasileira de Ortopedia (English Edition),* vol. 49, no. 2, pp. 140-148, 2014.

[18] J. B. Stiehl, A. M. DiGioia, R. G. Haaker, and W. H. Konermann, *Navigation and MIS in orthopedic surgery*: Springer, 2007.

[19] S. R. Shaarani, G. McHugh, and D. A. Collins, "Accuracy of digital preoperative templating in 100 consecutive uncemented total hip arthroplasties: a single surgeon series," *The Journal of arthroplasty,* vol. 28, no. 2, pp. 331-337, 2013.

[20] S. S. Shemesh, J. Robinson, A. Keswani, M. J. Bronson, C. S. Moucha, and D. Chen, "The accuracy of digital templating for primary total hip arthroplasty: is there a difference between direct anterior and posterior approaches?," *The Journal of arthroplasty,* vol. 32, no. 6, pp. 1884-1889, 2017.

[21] E. Sariali, R. Mauprivez, F. Khiami, H. Pascal-Mousselard, and Y. Catonné, "Accuracy of the preoperative planning for cementless total hip arthroplasty. A randomised comparison between three-dimensional computerised planning and conventional

templating," *Orthopaedics & Traumatology: Surgery & Research*, vol. 98, no. 2, pp. 151-158, 2012.

[22] M. D. Schofer, T. Pressel, T. J. Heyse, J. Schmitt, and U. Boudriot, "Radiological determination of the anatomic hip centre from pelvic landmarks," *Acta Orthopædica Belgica*, vol. 76, no. 4, pp. 479, 2010.

[23] F. A. Osmani, S. Thakkar, A. Ramme, A. Elbuluk, P. Wojack, and J. M. Vigdorchik, "Variance in predicted cup size by 2-dimensional vs 3-dimensional computerized tomography–based templating in primary total hip arthroplasty," *Arthroplasty today*, vol. 3, no. 4, pp. 289-293, 2017.

[24] A. Fatah, and E. ElHak, "Three Dimensional Nonlinear Statistical Modeling Framework for Morphological Analysis," 2012.

[25] M. R. Mahfouz, B. Merkl, E. Abdel Fatah, R. Booth Jr, and J. Argenson, "Automatic methods for characterization of sexual dimorphism of adult femora: distal femur," *Computer methods in biomechanics and biomedical engineering*, vol. 10, no. 6, pp. 447-456, 2007.

[26] M. Viceconti, R. Lattanzi, B. Antonietti, S. Paderni, R. Olmi, A. Sudanese, and A. Toni, "CT-based surgical planning software improves the accuracy of total hip replacement preoperative planning," *Medical Engineering & Physics*, vol. 25, no. 5, pp. 371-377, 2003/06/01/, 2003.

[27] Y. Kagiyama, I. Otomaru, M. Takao, N. Sugano, M. Nakamoto, F. Yokota, N. Tomiyama, Y. Tada, and Y. Sato, "CT-based automated planning of acetabular cup for total hip arthroplasty (THA) based on hybrid use of two statistical atlases," *International Journal of Computer Assisted Radiology and Surgery*, vol. 11, no. 12, pp. 2253-2271, December 01, 2016.

[28] E. Sariali, Y. Catonne, and H. Pascal-Moussellard, "Three-dimensional planning-guided total hip arthroplasty through a minimally invasive direct anterior approach. Clinical outcomes at five years' follow-up," *International Orthopaedics*, vol. 41, no. 4, pp. 699-705, April 01, 2017.

[29] E. L. Steinberg, N. Shasha, A. Menahem, and S. Dekel, "Preoperative planning of total hip replacement using the TraumaCad™ system," *Archives of orthopaedic and trauma surgery*, vol. 130, no. 12, pp. 1429-1432, 2010.

[30] I. Otomaru, M. Nakamoto, Y. Kagiyama, M. Takao, N. Sugano, N. Tomiyama, Y. Tada, and Y. Sato, "Automated preoperative planning of femoral stem in total hip arthroplasty from 3D CT data: Atlas-based approach and comparative study," *Medical image analysis*, vol. 16, no. 2, pp. 415-426, 2012.

[31] P. C. Noble, J. W. Alexander, L. J. Lindahl, D. T. Yew, W. M. Granberry, and H. S. Tullos, “The anatomic basis of femoral component design,” *Clinical orthopaedics and related research*, no. 235, pp. 148-165, 1988.

[32] P. Rubin, P. Leyvraz, J. Aubaniac, J. Argenson, P. Esteve, and B. De Roguin, “The morphology of the proximal femur. A three-dimensional radiographic analysis,” *The Journal of bone and joint surgery. British volume,* vol. 74, no. 1, pp. 28-32, 1992.

[33] T. A. Boymans, I. C. Heyligers, and B. Grimm, “The morphology of the proximal femoral canal continues to change in the very elderly: implications for total hip arthroplasty,” *The Journal of arthroplasty,* vol. 30, no. 12, pp. 2328-2332, 2015.

[34] O. Husmann, P. J. Rubin, P.-F. Leyvraz, B. de Roguin, and J.-N. Argenson, “Three-dimensional morphology of the proximal femur,” *The Journal of arthroplasty,* vol. 12, no. 4, pp. 444-450, 1997.

[35] A. Kaneuji, T. Matsumoto, M. Nishino, T. Miura, T. Sugimori, and K. Tomita, “Three-dimensional morphological analysis of the proximal femoral canal, using computer-aided design system, in Japanese patients with osteoarthrosis of the hip,” *Journal of orthopaedic science,* vol. 5, no. 4, pp. 361-368, 2000.

[36] M. Mahfouz, E. E. A. Fatah, L. S. Bowers, and G. Scuderi, “Three-dimensional morphology of the knee reveals ethnic differences,” *Clinical Orthopaedics and Related Research «,* vol. 470, no. 1, pp. 172-185, 2012.

[37] B. Mahaisavariya, K. Sitthiseripratip, T. Tongdee, E. L. Bohez, J. Vander Sloten, and P. Oris, “Morphological study of the proximal femur: a new method of geometrical assessment using 3-dimensional reverse engineering,” *Medical engineering & physics,* vol. 24, no. 9, pp. 617-622, 2002.

[38] D. S. Casper, G. K. Kim, J. Parvizi, and T. A. Freeman, “Morphology of the proximal femur differs widely with age and sex: relevance to design and selection of femoral prostheses,” *Journal of Orthopaedic Research,* vol. 30, no. 7, pp. 1162-1166, 2012.

[39] S.-Y. Baek, J.-H. Wang, I. Song, K. Lee, J. Lee, and S. Koo, “Automated bone landmarks prediction on the femur using anatomical deformation technique,” *Computer-Aided Design,* vol. 45, no. 2, pp. 505-510, 2013/02/01/, 2013.

[40] J. Ehrhardt, H. Handels, B. Strathmann, T. Malina, W. Plötz, and S. J. Pöppl, "Atlas-based recognition of anatomical structures and landmarks to support the virtual three-dimensional planning of hip operations." pp. 17-24.

[41] H. Jacinto, S. Valette, and R. Prost, “Multi-atlas automatic positioning of anatomical landmarks,” *Journal of Visual Communication and Image Representation,* vol. 50, pp. 167-177, 2018.

[42] C.-B. Phan, and S. Koo, “Predicting anatomical landmarks and bone morphology of the femur using local region matching,” *International journal of computer assisted radiology and surgery,* vol. 10, no. 11, pp. 1711-1719, 2015.

[43] K. Subburaj, B. Ravi, and M. Agarwal, “Automated identification of anatomical landmarks on 3D bone models reconstructed from CT scan images,” *Computerized Medical Imaging and Graphics,* vol. 33, no. 5, pp. 359-368, 2009/07/01/, 2009.

[44] P. Markelj, D. Tomaževič, B. Likar, and F. Pernuš, “A review of 3D/2D registration methods for image-guided interventions,” *Medical image analysis,* vol. 16, no. 3, pp. 642-661, 2012.

[45] B. Zitová, and J. Flusser, “Image registration methods: a survey,” *Image and Vision Computing,* vol. 21, no. 11, pp. 977-1000, 10//, 2003.

[46] M. Kass, A. Witkin, and D. Terzopoulos, “Snakes: Active contour models,” *International Journal of Computer Vision,* vol. 1, no. 4, pp. 321-331, 1988/01/01, 1988.

[47] P. J. Besl, and N. D. McKay, "Method for registration of 3-D shapes." pp. 586-606.

[48] A. Myronenko, and X. Song, “Point set registration: Coherent point drift,” *Pattern Analysis and Machine Intelligence, IEEE Transactions on,* vol. 32, no. 12, pp. 2262-2275, 2010.

[49] H. Chui, and A. Rangarajan, “A new point matching algorithm for non-rigid registration,” *Computer Vision and Image Understanding,* vol. 89, no. 2-3, pp. 114-141, 2003.

[50] J. A. Schnabel, D. Rueckert, M. Quist, J. M. Blackall, A. D. Castellano-Smith, T. Hartkens, G. P. Penney, W. A. Hall, H. Liu, and C. L. Truwit, "A generic framework for non-rigid registration based on non-uniform multi-level free-form deformations." pp. 573-581.

[51] P. J. Besl, and N. D. McKay, "Method for registration of 3-D shapes." pp. 586-607.

[52] D. J. Berry, W. S. Harmsen, M. E. Cabanela, and B. F. Morrey, “Twenty-five-year survivorship of two thousand consecutive primary Charnley total hip replacements: factors affecting survivorship of acetabular and femoral components,” *JBJS,* vol. 84, no. 2, pp. 171-177, 2002.

[53] J. H. Currier, M. A. Bill, and M. B. Mayor, “Analysis of wear asymmetry in a series of 94 retrieved polyethylene tibial bearings,” *Journal of biomechanics,* vol. 38, no. 2, pp. 367-375, 2005.

[54] J. D. DesJardins, P. S. Walker, H. Haider, and J. Perry, “The use of a force-controlled dynamic knee simulator to quantify the mechanical performance of total knee

replacement designs during functional activity," *Journal of Biomechanics,* vol. 33, no. 10, pp. 1231-1242, 2000.

[55] C. J. Lavernia, R. J. Sierra, D. S. Hungerford, and K. Krackow, "Activity level and wear in total knee arthroplasty: a study of autopsy retrieved specimens," *The Journal of arthroplasty,* vol. 16, no. 4, pp. 446-453, 2001.

[56] R. D. Komistek, D. A. Dennis, and M. Mahfouz, "In vivo fluoroscopic analysis of the normal human knee," *Clinical orthopaedics and related research,* vol. 410, pp. 69-81, 2003.

[57] D. A. Dennis, R. D. Komistek, C. E. Colwell Jr, C. S. Ranawat, R. D. Scott, T. S. Thornhill, and M. A. Lapp, "In vivo anteroposterior femorotibial translation of total knee arthroplasty: a multicenter analysis," *Clinical Orthopaedics and Related Research®,* vol. 356, pp. 47-57, 1998.

[58] J. B. Stiehl, R. D. Komistek, D. A. Dennis, R. D. Paxson, and W. A. Hoff, "Fluoroscopic analysis of kinematics after posterior-cruciate-retaining knee arthroplasty," *The Journal of bone and joint surgery. British volume,* vol. 77, no. 6, pp. 884-889, 1995.

[59] D. A. Dennis, R. D. Komistek, W. A. Hoff, and S. M. Gabriel, "In vivo knee kinematics derived using an inverse perspective technique," *Clinical Orthopaedics and Related Research®,* vol. 331, pp. 107-117, 1996.

[60] R. D. Komistek, J. B. Stiehl, D. A. Dennis, R. D. Paxson, and R. W. Soutas-Little, "Mathematical model of the lower extremity joint reaction forces using Kane's method of dynamics," *Journal of Biomechanics,* vol. 31, no. 2, pp. 185-189, 1997.

[61] M. T. LaCour, "Development and Implementation of a Forward Solution Hip Mathematical Model to Determine In Vivo Mechanics and Predict Hip Separation," *PhD diss., University of Tennessee*, 2017.

[62] L. Modenese, and A. T. M. Phillips, "Prediction of hip contact forces and muscle activations during walking at different speeds," *Multibody System Dynamics,* vol. 28, no. 1, pp. 157-168, August 01, 2012.

[63] L. Modenese, A. T. M. Phillips, and A. M. J. Bull, "An open source lower limb model: Hip joint validation," *Journal of Biomechanics,* vol. 44, no. 12, pp. 2185-2193, 2011/08/11/, 2011.

[64] M. S. Shourijeh, K. B. Smale, B. M. Potvin, and D. L. Benoit, "A forward-muscular inverse-skeletal dynamics framework for human musculoskeletal simulations," *Journal of Biomechanics,* vol. 49, no. 9, pp. 1718-1723, 2016/06/14/, 2016.

[65] S. L. Delp, F. C. Anderson, A. S. Arnold, P. Loan, A. Habib, C. T. John, E. Guendelman, and D. G. Thelen, "OpenSim: open-source software to create and analyze

dynamic simulations of movement," *IEEE transactions on biomedical engineering,* vol. 54, no. 11, pp. 1940-1950, 2007.

[66] T. P. Andriacchi, T. S. Stanwyck, and J. O. Galante, "Knee biomechanics and total knee replacement," *The Journal of arthroplasty,* vol. 1, no. 3, pp. 211-219, 1986.

[67] F. C. Anderson, and M. G. Pandy, "Dynamic optimization of human walking," *Journal of biomechanical engineering,* vol. 123, no. 5, pp. 381-390, 2001.

[68] B. J. Fregly, J. A. Reinbolt, K. L. Rooney, K. H. Mitchell, and T. L. Chmielewski, "Design of patient-specific gait modifications for knee osteoarthritis rehabilitation," *IEEE Transactions on Biomedical Engineering,* vol. 54, no. 9, pp. 1687-1695, 2007.

[69] J. A. Reinbolt, J. F. Schutte, B. J. Fregly, B. I. Koh, R. T. Haftka, A. D. George, and K. H. Mitchell, "Determination of patient-specific multi-joint kinematic models through two-level optimization," *Journal of Biomechanics,* vol. 38, no. 3, pp. 621-626, 2005/03/01/, 2005.

[70] J. A. Reinbolt, A. Seth, and S. L. Delp, "Simulation of human movement: applications using OpenSim," *Procedia IUTAM,* vol. 2, pp. 186-198, 2011/01/01/, 2011.

[71] D. Glaser, D. A. Dennis, R. D. Komistek, and T. M. Miner, "In vivo comparison of hip mechanics for minimally invasive versus traditional total hip arthroplasty," *Clinical Biomechanics,* vol. 23, no. 2, pp. 127-134, 2008.

[72] A. Sharma, R. D. Komistek, C. S. Ranawat, D. A. Dennis, and M. R. Mahfouz, "In vivo contact pressures in total knee arthroplasty," *The Journal of arthroplasty,* vol. 22, no. 3, pp. 404-416, 2007.

[73] A. Sharma, F. Leszko, R. D. Komistek, G. R. Scuderi, H. E. Cates Jr, and F. Liu, "In vivo patellofemoral forces in high flexion total knee arthroplasty," *Journal of Biomechanics,* vol. 41, no. 3, pp. 642-648, //, 2008.

[74] S. Du, N. Zheng, S. Ying, Q. You, and Y. Wu, "An extension of the ICP algorithm considering scale factor." pp. V-193-V-196.

[75] W. J. Schroeder, B. Lorensen, and K. Martin, *The visualization toolkit: an object-oriented approach to 3D graphics*: Kitware, 2004.

[76] M. A. Fischler, and R. C. Bolles, "Random sample consensus: a paradigm for model fitting with applications to image analysis and automated cartography," *Commun. ACM,* vol. 24, no. 6, pp. 381-395, 1981.

[77] P. H. Torr, and A. Zisserman, "MLESAC: A new robust estimator with application to estimating image geometry," *Computer vision and image understanding,* vol. 78, no. 1, pp. 138-156, 2000.

[78] G. Lecerf, M. H. Fessy, R. Philippot, P. Massin, F. Giraud, X. Flecher, J. Girard, P. Mertl, E. Marchetti, and E. Stindel, "Femoral offset: Anatomical concept, definition, assessment, implications for preoperative templating and hip arthroplasty," *Orthopaedics & Traumatology: Surgery & Research,* vol. 95, no. 3, pp. 210-219, 2009/05/01/, 2009.

[79] R. B. Bourne, and C. H. Rorabeck, "Soft tissue balancing: The hip," *The Journal of Arthroplasty,* vol. 17, no. 4, Supplement 1, pp. 17-22, 2002/06/01/, 2002.

[80] D. Synthes, "Corail Hip System: Product Rationale and Surgical Technique," *DePuy France S.A.S,* 2017.

[81] D. Markowicz, "Planning for Total Hip Replacement: Templating," *ICJR, December 2010, Miami, FL*, 2010.

[82] T. Siguier, M. Siguier, and B. Brumpt, "Mini-incision anterior approach does not increase dislocation rate: a study of 1037 total hip replacements," *Clinical orthopaedics and related research,* vol. 426, pp. 164-173, 2004.

[83] K. C. Bertin, and H. Röttinger, "Anterolateral mini-incision hip replacement surgery: a modified Watson-Jones approach," *Clinical Orthopaedics and Related Research®,* vol. 429, pp. 248-255, 2004.

[84] R. E. Kennon, J. M. Keggi, R. S. Wetmore, L. E. Zatorski, M. H. Huo, and K. J. Keggi, "Total hip arthroplasty through a minimally invasive anterior surgical approach," *JBJS,* vol. 85, pp. 39-48, 2003.

[85] J. M. Matta, C. Shahrdar, and T. Ferguson, "Single-incision anterior approach for total hip arthroplasty on an orthopaedic table," *Clinical Orthopaedics and Related Research®,* vol. 441, pp. 115-124, 2005.

[86] M. Ali Khan, P. Brakenbury, and I. Reynolds, "Dislocation following total hip replacement," *The Journal of bone and joint surgery. British volume,* vol. 63, no. 2, pp. 214-218, 1981.

[87] J. L. Masonis, and R. B. Bourne, "Surgical approach, abductor function, and total hip arthroplasty dislocation," *Clinical Orthopaedics and Related Research (1976-2007),* vol. 405, pp. 46-53, 2002.

[88] P. M. Pellicci, M. Bostrom, and R. Poss, "Posterior approach to total hip replacement using enhanced posterior soft tissue repair," *Clinical Orthopaedics and Related Research®,* vol. 355, pp. 224-228, 1998.

[89] R. E. White Jr, T. J. Forness, J. K. Allman, and D. W. Junick, "Effect of posterior capsular repair on early dislocation in primary total hip replacement," *Clinical Orthopaedics and Related Research®,* vol. 393, pp. 163-167, 2001.

[90] M. Müller, S. Tohtz, I. Springer, M. Dewey, and C. Perka, "Randomized controlled trial of abductor muscle damage in relation to the surgical approach for primary total hip replacement: minimally invasive anterolateral versus modified direct lateral approach," *Archives of orthopaedic and trauma surgery,* vol. 131, no. 2, pp. 179-189, 2011.

[91] J. R. Howell, B. A. Masri, and C. P. Duncan, "Minimally invasive versus standard incision anterolateral hip replacement: a comparative study," *The Orthopedic clinics of North America,* vol. 35, no. 2, pp. 153-162, 2004.

[92] R. A. Berger, "Mini-incision total hip replacement using an anterolateral approach: technique and results," *The Orthopedic clinics of North America,* vol. 35, no. 2, pp. 143-151, 2004.

[93] C. Quammen, C. Weigle, and R. Taylor, "Boolean operations on surfaces in vtk without external libraries," *The VTK Journal,* vol. 5, 2011.

[94] C. S. Shin, A. M. Chaudhari, and T. P. Andriacchi, "The influence of deceleration forces on ACL strain during single-leg landing: a simulation study," *Journal of biomechanics,* vol. 40, no. 5, pp. 1145-1152, 2007.

[95] T. R. Kane, and D. A. Levinson, "The use of Kane's dynamical equations in robotics," *The International Journal of Robotics Research,* vol. 2, no. 3, pp. 3-21, 1983.

[96] T. R. Kane, and D. A. Levinson, *Dynamics, theory and applications*: McGraw Hill, 1985.

[97] D. A. Levinson, and T. R. Kane, "AUTOLEV — A New Approach to Multibody Dynamics," *Multibody Systems Handbook*, W. Schiehlen, ed., pp. 81-102, Berlin, Heidelberg: Springer Berlin Heidelberg, 1990.

[98] A. Fedorov, R. Beichel, J. Kalpathy-Cramer, J. Finet, J.-C. Fillion-Robin, S. Pujol, C. Bauer, D. Jennings, F. Fennessy, and M. Sonka, "3D Slicer as an image computing platform for the Quantitative Imaging Network," *Magnetic resonance imaging,* vol. 30, no. 9, pp. 1323-1341, 2012.

[99] M. R. Mahfouz, W. A. Hoff, R. D. Komistek, and D. A. Dennis, "A robust method for registration of three-dimensional knee implant models to two-dimensional fluoroscopy images," *IEEE Trans. Med. Imaging,* vol. 22, no. 12, pp. 1561-1574, 2003.

[100] L. D. Dorr, and J. J. Callaghan, "Death of the Lewinnek "Safe Zone"," *The Journal of arthroplasty,* vol. 34, no. 1, pp. 1-2, 2019.

[101] M. P. Abdel, P. von Roth, M. T. Jennings, A. D. Hanssen, and M. W. Pagnano, "What safe zone? The vast majority of dislocated THAs are within the Lewinnek safe zone for acetabular component position," *Clinical Orthopaedics and Related Research®,* vol. 474, no. 2, pp. 386-391, 2016.

[102] D. Bhaskar, A. Rajpura, and T. Board, “Current concepts in acetabular positioning in total hip arthroplasty,” *Indian journal of orthopaedics,* vol. 51, no. 4, pp. 386, 2017.

VITA

Manh Ta's passion is to bring knowledge of engineers to improve health care practice and medical treatment. Vietnam, his home country, has a very high traffic-related accident rate. According to a report by the World Health Organization in 2010, road traffic injury was the leading cause of 14,000 deaths and 2,500 thousand of disabilities per year. Therefore, he decided to pursue a Ph.D.'s degree in Biomedical Engineering at the University of Tennessee – Knoxville, USA and carried out his research related to human movement analysis, computer-assisted orthopedic surgery, and medical image processing. He earned his Ph.D degree in Spring 2019.

At the early stage of middle school, Manh quickly showed strong enthusiasm for the relationship between Physics and motion. At high school, he was selected among 500 students in his city to attend a specialized class in Physics where he advanced his background in rigid body movement and advanced physics. As a college student in the honor program at Hanoi University of Science and Technology, Vietnam, he continued his study in multi-body movement by seriously taking fundamental mechanic courses. During this time, Manh also participated in several national competitions, including National Mechanics Olympic Competition, National Physics Competition, and won the high placements. After finishing his bachelor's degree in Mechatronics in Spring 2013, he was honorably awarded the Young Scientist Scholarship from Chung-Ang University, South Korea, to pursue a master's degree in Mechanical Engineering and earned this degree in Spring 2016.

Working as a research assistant in the Biomechanics Laboratory throughout his Master program, Manh has explored a relationship between a joint injury and joint movement. He discovered that the motion pattern of a healthy joint during any activity differs from an injured joint. He, therefore, developed an algorithm which can calculate and visualize joint motion on the computer. This program helped surgeons comprehensively understand how a healthy and an injured joint move during daily activity. Incorporating innovative ideas for his research, he presented his research to many world-renowned conferences in his field and exchange ideas with worldwide scholars.